Lifted Turbulent Jet Flames

Thesis by
Jay A. Hammer

In Partial Fulfillment of the Requirements
for the Degree of
Doctor of Philosophy

California Institute of Technology
Pasadena, California

1993
(submitted April 14, 1993)

Acknowledgements

There are many people to whom I am deeply indebted for their support in this undertaking. First, I would like to thank my advisor, Prof. Anatol Roshko, whose enthusiasm for this project and fluid mechanics in general was a source of inspiration to me. I appreciated the freedom and responsibility he gave me. I would also like to thank Dr. Richard C. Miake-Lye for a tremendous amount of help in the early part of this study, and for encouraging me to continue my graduate studies toward a Ph.D. To Prof. Ed Zukoski I am grateful for the use of his equipment, greatly in excess of what I had any right to ask for. Helpful discussions with Dr. Gene Broadwell and Prof. Paul Dimotakis are also greatly appreciated. Dr. Robert Schefer and Dr. Mehdi Namazian were instrumental in conducting the imaging experiments at Sandia National Labs, and discussions with them concerning the results were also very helpful.

The financial support of the Office of Naval Research through Grant No. N00014–89–J–1991, from the Propulsion and Energetics Program, is gratefully acknowledged. The Gas Research Institute's support of Dr. Miake-Lye is gratefully acknowledged as well. The financial support of Caltech, including the building of my laboratory, is highly appreciated.

Many of my friends made my stay here both more enjoyable and enlightening, including Dr. Mike Youngquist and Dr. John Budzinski. I am thankful to Dr. Paul Miller for many interesting discussions, both technical and non-technical. It was a pleasure to have the company of Dr. Greg Cardell and Dr. Derek Lisoski through the final phases of work on the thesis. The close friendship and support of Kris Gates was also a great help. I would also like to thank my parents, Joel and Amara, for giving me so much, including their generous support throughout my studies.

Abstract

Experiments were conducted on lifted, turbulent jet diffusion flames. An automated technique using a linear photodiode array was implemented to measure the temporal history of the liftoff height h. The measurements enabled accurate determination of the mean liftoff height $\bar{h}$ under a wide range of flow conditions, including several fuels, nozzle diameters, and exit velocities U_s. The results showed an approximately linear relationship between $\bar{h}$ and U_s, with a slight dependence on Reynolds number. A strain-rate model for liftoff, based on far-field scaling of turbulent jets, provides an explanation for the linear dependence of $\bar{h}$ on U_s. Measurements were also made in which the nozzle fluid contained varying amounts of air, where it was found that the slope of the $\bar{h}$ *vs.* U_s line increases faster than predicted by far-field scaling of turbulent jets. The discrepancy is attributed to near-field effects.

The amplitudes of the fluctuations in h were found to be of the order of the local large scale of the jet. There is a slight increase in normalized fluctuation level $h'/\bar{h}$ with $\bar{h}$, and there is some variation of $h'/\bar{h}$ with fuel type. The time scales of the fluctuations of h were found to be considerably longer than the local large-scale time of the turbulence τ_δ. By using fuels of different chemical times to vary τ_δ, the measured correlation time $\tau_{1/2}$ normalized by τ_δ was found to collapse with Richardson number ξ_h. Experiments in which the nozzles were oriented horizontally showed no change in $\tau_{1/2}$, however. Additional experiments were conducted to investigate alternative explanations for the variation of $\tau_{1/2}/\tau_\delta$ with ξ_h. These experiments included measuring the flame length L simultaneously with h, and measuring the visible radiation I simultaneously with h. $L(t)$ was found to be nearly uncorrelated with $h(t)$, dismissing the possibility that a feedback mechanism from L to h controls the fluctuations of h. Although $I(t)$ is highly correlated with $h(t)$ for the most sooting fuel, acetylene, it is not deemed responsible for the longer

correlation times of that fuel. This was deduced from experiments using mixtures of hydrogen with other fuels, which produce very little radiation, but which have values of $\tau_{1/2}/\tau_\delta$ comparable to those of acetylene flames.

Another experiment was conducted in which two-dimensional images of fuel concentration (CH_4) and reaction zones (indicated by CH) were obtained. The images showed a wide variety of structure types, indicating that there is no universal description of the flow field at the flame base. The flame stabilization position showed large fluctuations in both the axial and radial directions. The shot to shot variation in methane number density at the flame base was also large.

Table of Contents

List of Figures

List of Tables

List of Symbols

English

a	speed of sound
C	various constants, depending on subscript
C_p	constant pressure specific heat
d	nozzle diameter
d_s	equivalent source diameter
$E_h(f)$	power spectrum of $h(t)$
f	frequency
h	liftoff height
$\tilde{h}$	non-dimensional liftoff height (see Sec. A.4)
ΔH_f	enthalpy of combustion (J/kg-fuel)
I	light intensity as measured by photodiode array
J	momentum flux
k	thermal conductivity
L	flame length
$\dot{m}$	mass flux
M_s	source Mach number, U_s/a_∞
p	pressure
q	heat release rate of flame
Q	volumetric flow rate
r	radial distance
R_{hh}	autocorrelation of h
Re	Reynolds number
Ri	Richardson number
Ri_h	Richardson number at flame base (see Sec. A.6)
S	laminar flame speed
t	time

Δt	sample interval of measurement of h, L or I
T	temperature
ΔT_f	adiabadic flame temperature rise
u	velocity
U_o	mass-averaged velocity exiting nozzle
$U_{\rm s}$	equivalent source velocity
y	radial coordinate of imaging experiments
Y	mass fraction fuel
$Y_{\rm st}$	stoichiometric mass fraction
x	axial distance from nozzle
x_I	measurement location of I

Greek

$\delta(x)$	local jet width at axial location x, $0.44\,x$
η	r/x
κ	thermal diffusivity
μ	viscosity
ν	μ/ρ
ξ_h	$Ri_h^{1/3}$
ξ_L	$Ri_L^{1/3}$
$\rho(\tau)$	correlation function
ρ	density
$\breve{\rho}$	mixing cup density
$\overline{\Delta\rho}$	average value of $\rho_\infty - \rho$ in flame
σ	strain rate
$\sigma_{\rm cr}$	critical strain rate of fuel
$\sigma_{\rm ext}$	strain rate for extinction of laminar diffusion flame
τ	time lag
$\tau_{1/2}$	time at which autocorrelation reaches 0.5
τ_χ	chemical time of fuel

τ_{lo}	effective chemical time of fuel from liftoff results, $\bar{h}/Y_{\mathrm{st}}U_{\mathrm{s}}$
τ_δ	local large-scale time, δ/U_{cl}
τ_{c}	convection time

Other Symbols

$\overline{(\ )}$	time average
$(\ )'$	rms value (except in Sec. 4.8)
$[\,]$	normalized number density or scattering signal (Ch. 5)
$(\ )_{\mathrm{cl}}$	centerline
$(\ )_f$	adiabadic flame, *e.g.*, ΔT_f, MW_f
$(\ )_{\mathrm{fm}}$	at the flow meter
$(\ )_{\mathrm{lo}}$	liftoff (τ_{lo})
$(\ )_{\mathrm{o}}$	nozzle origin
$(\ )_{\mathrm{s}}$	effective source
$(\ )_{\mathrm{srm}}$	strain-rate model (f_{srm})
$(\ )_\infty$	far field of (non-reacting) jet
$(\ )_h$	at the liftoff height, h
$(\ )_L$	at the flame length, L
$(\ )_{\mathrm{st}}$	stoichiometric conditions

CHAPTER 1

Introduction

Many combustion devices employ turbulent flow to achieve efficient mixing of fuel and oxidizer. In particular, turbulent jets are used extensively. To reach a high combustion efficiency, conditions are sometimes chosen such that the flame stability is a concern. There are many factors which determine the stability of the flame, including the rate of chemical reactions, strain rates in the flow, and the mixing of products (which serve as the ignition source) with the reactants.

The lifted, turbulent jet flame is a useful flow to investigate these complex issues. Consisting of a jet of fuel issuing from a round nozzle into an oxidizer (air), it has a relatively simple geometry. Under certain flow conditions, the flame is detached from the nozzle (lifted). With such a flame, there is a region from the nozzle to the flame base in which the fuel mixes with the oxidizer, but no burning occurs. Further downstream, where the velocities and strain rates are lower, the flame is stabilized. A shadowgraph image of a lifted, turbulent propane flame is shown in Fig. 1.1. The mixing of the turbulent jet below the flame base is visible, as is the abrupt transition to the flame base, where there is a substantial change in the structure of the turbulence, as evidenced by the initial change in spreading angle of the flow. Because the flow below the flame base is largely unaffected by the combustion occurring above, it is the much-studied turbulent jet.

The goal of this research is to gain an understanding of the stabilization mechanism of lifted flames. In particular, the temporal behavior is of interest. It is hoped that knowledge gained from studying lifted flames can be applied to other problems in flame stability.

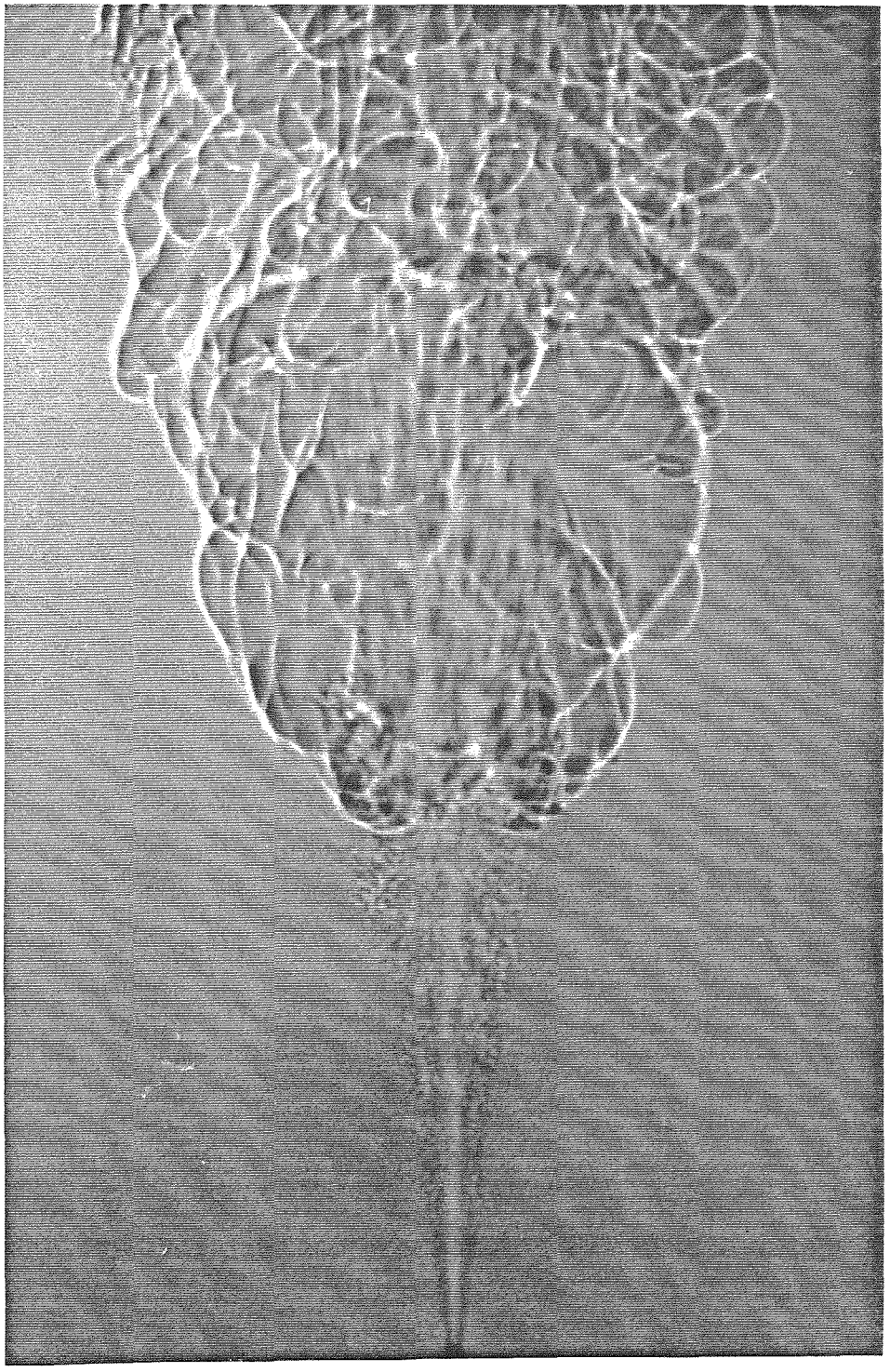

FIG. 1.1 Shadowgraph image of a lifted turbulent propane flame. The nozzle diameter is 3.8 mm, the exit velocity is 66 m/s, and the liftoff height is $\sim$ 150 mm.

1.1 Background

Lifted diffusion flames have been studied by many investigators in the past (*e.g.*, Vanquickenborne and Van Tiggelen 1966, Kalghatgi 1984, Peters and Williams 1983, Eickhoff *et al.* 1985, Lockwood and Moneib 1982). Some studies have focused on flames stabilized in the near-field region of the jet in which the shear layer begins to roll up (*e.g.*, Savas and Gollahalli 1986a, Gollahalli *et al.* 1987). In particular, the processes of detachment from the nozzle and reattachment to the nozzle have received considerable attention. Other studies have examined the behavior of flames stabilized further downstream (up to $\sim$ 50 nozzle diameters, depending on the fuel). In addition, Savas and Gollahalli (1986b) and Chung and Lee (1991) have investigated lifted *laminar* flames, in part to provide a starting point for understanding the turbulent flames.

Experimental results of Kalghatgi (1984) have shown that the mean (time-averaged) liftoff distance $\bar{h}$ of turbulent flames increases approximately linearly with nozzle exit velocity U_o, independent of the nozzle diameter d, once $\bar{h}$ is sufficiently far downstream (approximately $20\,d$). The slope of the $\bar{h}$ *vs.* U_o line depends on the fuel used. At a maximum velocity U_b, proportional to d, the flame blows out. Because $\bar{h} \sim U_o$, blowout occurs when $\bar{h}$ reaches a maximum distance proportional to d, for a given fuel.

Several models have been proposed to explain the liftoff behavior. These models can generally be divided into two categories, those which propose that the stabilization distance is governed by a balance between the propagation rate of the flame and the velocity of the approaching flow, and those which propose that the liftoff location is the most upstream position in which the turbulent mixing does not extinguish the combustion. The former type of model is described by Kalghatgi (1984), in which an expression for the turbulent flame speed in terms of the laminar flame speed and the turbulence properties is used. Models of the later type include the mixing-rate model of Broadwell *et al.* (1985), the scalar-dissipation-rate model of Peters and Williams (1983), and our own strain-rate model (Miake-Lye

and Hammer 1989). Additional classifications of the models in terms of the importance given to the large-scale structure of the turbulence can also be made. Another model which collapses the data well but has no theoretical basis has been proposed by Pitts (1989).

Although most of the experiments on flames stabilized in the far field have focused on the mean behavior, there have been some measurements of fluctuating properties. Lockwood and Moneib (1982) measured fluctuating temperatures with thermocouples, using a compensation technique to extend the frequency range of the measurements. Chen *et al.* (1989) measured temperatures along a line using thin film pyrometry, allowing them to track the radial position of the reaction zone. Using a video camera, Birch and Hargrave (1989) measured fluctuating liftoff heights of choked, underexpanded natural gas flames.

There are many unresolved issues concerning the mechanism by which lifted flames are stabilized, and the present experiments were undertaken to help elucidate the stabilization process.

1.2 Current Experiments

To improve upon previous measurements of the liftoff height, a new measurement system was designed in which the flame light was focused directly onto a linear photodiode array aligned with the axis of the flame. The liftoff height could then be found by detecting the visible radiation at the flame base. This enabled temporal information to be obtained, in addition to the time-averaged liftoff height.

Measurements of the time history of the liftoff height were made for moderate durations, for the purpose of determining the mean value. The fuels used in these experiments were natural gas (abbreviated as n.g.; 93.5% CH_4, 3.1% C_2H_6, 1.9% N_2, 0.6% C_3H_8, 0.6% CO_2, 0.2% C_4H_{10}, 0.1% C_5H_{12}), ethane (C_2H_6), ethylene (C_2H_4), and acetylene (C_2H_2). For each of the four fuels, two or three different nozzles of varying diameter were used. Liftoff heights ranging from the maximum

attainable for each nozzle down to approximately half of that height were measured. Limiting the conditions to this range ensured that the flames studied were stabilized far enough downstream of the nozzle exit that self similar behavior of the jet below the flame base was achieved, at least to a reasonable approximation. In addition to jets of pure fuel exiting the nozzle, measurements were made in which the fuel was premixed with air, but still fuel rich and thus requiring ambient air for complete combustion.

More extensive measurements were also made with all four fuels in which, for each fuel, two different nozzle diameters were used and four different liftoff heights studied for each nozzle. Using two nozzles for each fuel allowed the effects of Reynolds number to be investigated, while using different fuels provided a mechanism for varying the local fluid-mechanical time scale as well as a buoyancy parameter relevant to the dynamics of the flame base. From the longer data sets statistical analyses of the temporal fluctuations were obtained. In addition to the above listed fuels, experiments were done with fuel mixtures. A mixture of 50% C_2H_2 / 50% C_2H_6 was used, primarily to compare with C_2H_4 flames. Mixtures of hydrogen (H_2) with each of the fuels C_2H_6, C_2H_4, and C_2H_2 were also used to achieve greater control over the chemical rate of the fuel.

As an additional test of the importance of buoyancy to the liftoff height dynamics, experiments were conducted with the nozzles oriented horizontally. The fuels used in these experiments were natural gas, C_2H_4, and C_2H_2.

To investigate whether the behavior at the flame tip affects the liftoff height, additional experiments were conducted in which the liftoff height and the flame length were measured simultaneously. The fuels investigated in these tests were natural gas and C_2H_6.

Similarly, simultaneous measurements were made of the liftoff height and the flame radiation at a location downstream of the liftoff height. This was done to see whether the flame radiation fluctuations are correlated with, and might affect, the liftoff height of the more radiative fuels (C_2H_2 in particular).

To better understand the flame structure and the stabilization process, experiments were conducted in which planar, two-dimensional images of both the fuel and reaction zones of a methane (CH_4) flame were obtained by simultaneous measurements of Raman scattering from CH_4 and fluorescence from CH, which marks the reaction zones. These experiments were done in collaboration with Sandia National Labs in Livermore, CA. In the flow condition reported here, the fuel was premixed with air, and the flame was lifted to an intermediate liftoff height, ~ 0.6 times the maximum height before blowout.

CHAPTER 2

Experimental Facilities

2.1 Liftoff Height Measurements

2.1.1 Nozzles and Flow Control

The nozzles used in the liftoff height experiments performed at Caltech were designed to produce fully developed turbulent pipe flow at the exit. All nozzles were made from brass tubes, except the smallest nozzle which was made from stainless steel. The nozzles had length to diameter ratios of $\sim$ 60. The outside of each nozzle was tapered at a 15 degree half angle to reduce disturbances to the entrained flow near the exit. If the jet is modeled as a semi-infinite line sink, the streamline approaching the nozzle exit is a parabola. Although a parabola is then the ideal choice for the external shape of the nozzle, a straight taper was chosen because it is simple to construct, and it does not directly obstruct the natural streamline. To facilitate connection to a plastic tube supplying the fuel, the nozzles were soldered to successively larger brass tubes until reaching an outer diameter of 9.5 mm (3/8 in.). The entrance to the final (smallest) diameter tube of each nozzle was sharp edged to produce turbulent flow right from the beginning of the tube. Figure 2.1 shows the design of the 2.16 mm nozzle. Several different nozzle diameters were used, to have flexibility in adjusting the Reynolds number and liftoff height for the various fuels. The nozzle diameters used in these experiments were 1.02, 1.55, 2.16, 3.12, 3.88, 4.61, 4.92, 6.25, and 7.73 mm. For all of the nozzles, the exit was located 53 cm above the floor.

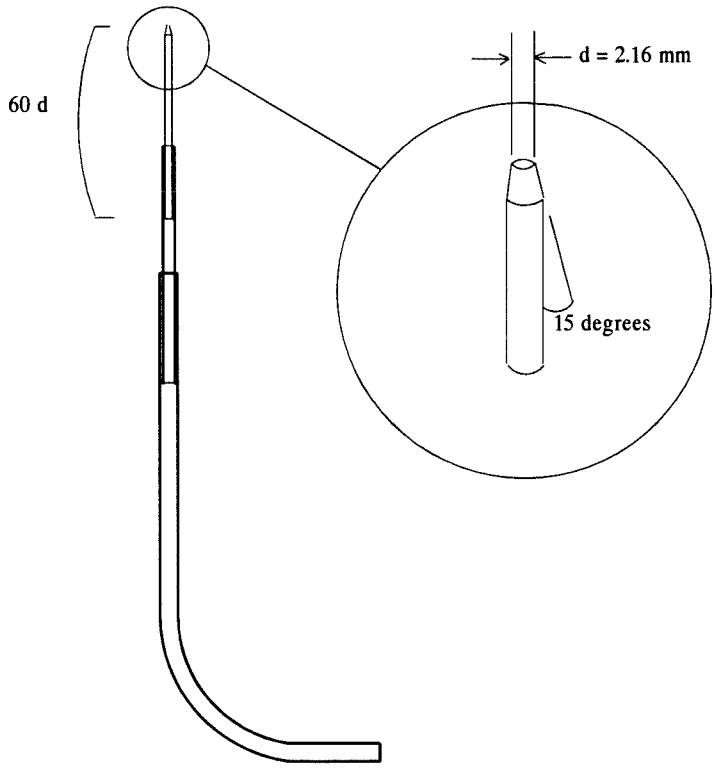

FIG. 2.1 Design of the 2.16 mm nozzle. Brass tubes with outer diameters of 9.5 mm, 6.4 mm, and 3.2 mm are soldered together as shown, reaching a final inner diameter of 2.16 mm.

Combustion gases were carried out of the lab through a fume hood using a blower. The hood was 1.5 m square and located 2.4 m above the laboratory floor. The blower had a flow rate of 1.2 m^3/s. Screens were placed around the flame to minimize the disturbances from room drafts. A double layer of screens was used around the perimeter of the hood and an additional cylindrical screen of diameter 68 cm and height 120 cm was placed around the flame. In the studies of horizontal flames, the nozzles protruded through the double layer of screens around the hood, and the cylindrical screen was suspended horizontally. All screens had an open area of 70%, and were painted black to reduce reflections of light.

Flow rates of the fuels were controlled with valves and measured with laminar flow elements (LFE's), Meriam models `50MW20-1` and `50MJ10-9`. The pressure drop

Δp across the LFE was measured with a Barocel pressure transducer type 590-D, with a full range of 10 torr. The upstream pressure $p_{\rm fm}$ (the subscript fm stands for conditions at the LFE) was measured with an Ashcroft test gauge, with a range of 0 to 15 psi. The gas temperature upstream of the flow element was measured with a type K thermocouple to determine the viscosity $\mu_{\rm fm}$ and density $\rho_{\rm fm}$. Values of viscosity, required for converting pressure drop into flow rate, were taken from Reid *et al.* (1977).

The volumetric flow rate at the LFE was obtained from the solution of the equation

$$\Delta p \;=\; C_1\,\mu_{\rm fm}\,Q_{\rm fm} + C_2\,\rho_{\rm fm}\,Q_{\rm fm}^2 \;, \tag{2.1}$$

where Q is volumetric flow rate, and C_1 and C_2 are constants from a calibration of the LFE. The quadratic term in Eq. 2.1 was always small.

The mean velocity U_o at the nozzle exit was then found by assuming that the gas reached atmospheric pressure and temperature, *i.e.*,

$$U_o \;=\; \frac{Q_{\rm fm}\,(p_{\rm fm}/p_\infty)\,(T_\infty/T_{\rm fm})}{(\pi/4)\,d^2} \;,$$

where the subscript ∞ stands for ambient conditions present at the nozzle exit.

The natural gas used in the experiments was gas was taken from a commercial supply line, with its composition determined from the gas company sample analysis. The purities of the bottled fuels were: C_2H_6 99%, C_2H_4 99.5%, C_2H_2 99.6%, and H_2 99.95%. Warm water was used to keep the regulators from icing, and a water bath was used upstream of the LFE to bring the gases close to room temperature.

2.1.2 Instrumentation and Measurement Technique

For measuring the liftoff height, a Reticon linear photodiode array was used. The array was a type T with 512 pixels spaced at 50 μm; each pixel was 2.5 mm wide. The visible radiative light emission was imaged directly onto the array using various camera lenses. The lenses used were a 50 mm f/1.4 Nikon lens, a 90 mm f/2.5 Pentax lens, and a 75—300 mm f/5.6 Pentax zoom lens. The particular lens used in a given experiment was chosen based on the size of the flame and its light intensity.

Data from the linear array were collected using an Everex 1800 personal computer (having an Intel 286 microprocessor) with an R.C. Electronics data acquisition board installed. The array was driven by a clock from an evaluation board supplied by Reticon, which was also used to synchronize data acquisition.

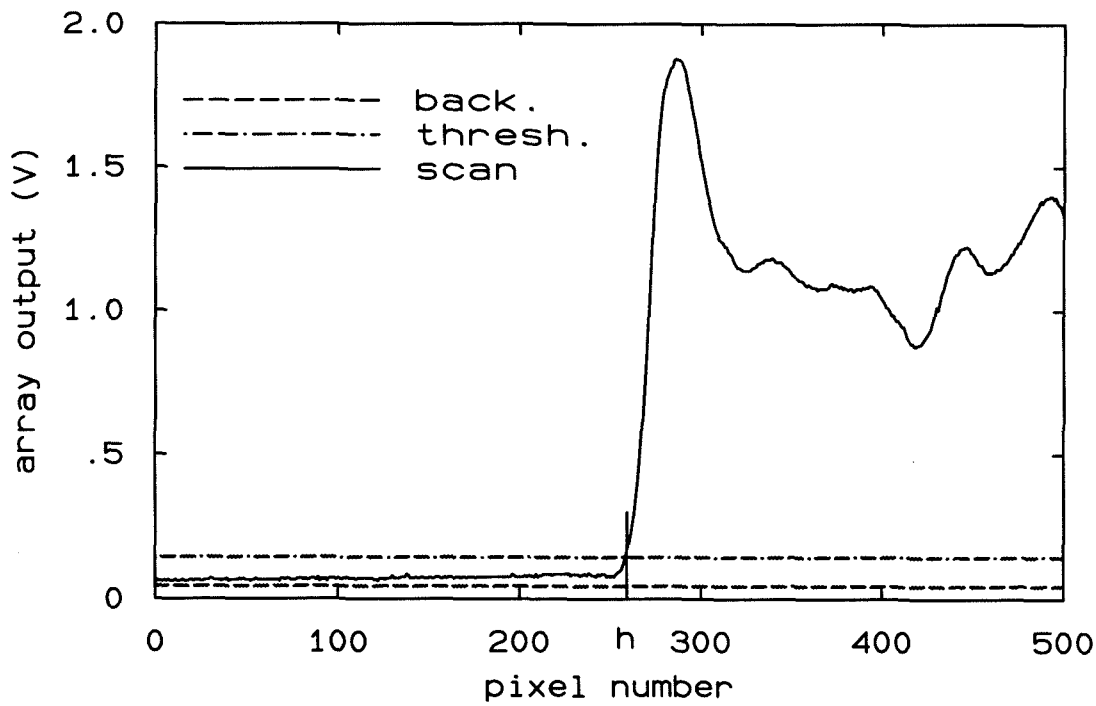

FIG. 2.2 Sample scan of the linear array imaging a C_2H_6 flame to illustrate the method for determining the liftoff height.

From each scan of the array, the liftoff height was found by looking for the first pixel with a voltage (light intensity) above a threshold value. This is illustrated

in Fig. 2.2, which shows one scan of the linear array imaging a C_2H_6 flame. The background level of the array, the threshold set some level above the background, and the actual array scan are all shown. There is a rather sudden increase in light intensity at the flame base.

For fuels producing large amounts of soot (C_2H_4 and C_2H_2), the radiation from which results in background light in the images, a slight modification was made to the algorithm for finding the liftoff height. Because this background noise was found to be relatively uniform along the array extent, it could be subtracted. In practice, before comparing a pixel's intensity with the threshold for determining liftoff height, the intensity 32 pixels below the current pixel was subtracted.

Because the computer memory was insufficient to store enough array scans to obtain meaningful statistics on the liftoff height, processing had to be done in real time with only the liftoff height being stored. As a sample of the raw data, the last 64 scans of the array were saved, however. This technique allowed up to 128K scans to be acquired for each flow condition. At one scan every 4.4 ms, this amounted to $\sim 9\,1/2$ minutes of data. For the faster flames, switches were selected on the circuit board controlling the array to cause only half of the pixels to be output, thereby increasing the data acquisition rate to one scan every 2.2 ms.

2.2 Imaging of Fuel and Flame Structures

Experiments to obtain planar images of CH_4 and CH were conducted at the Combustion Research Facility, Sandia National Laboratories in Livermore, CA. Both Raman scattering from CH_4 (fuel) and fluorescence from CH, which is present only in the reacting zones, were measured simultaneously using the DIANA pulsed dye laser. The simultaneous images allowed some insight to be gained into the relation between the fuel structures and the reaction zones.

As with the liftoff height measurements, the nozzle used in the imaging experiments was designed to produce fully developed, turbulent pipe flow at the exit. In

the imaging experiments, however, the jet emerged from a 50 mm bluff body, rather than being tapered on the outside. To form the laser light into a sheet, a multipass cell was used (Namazian *et al.* 1988), which reflects the laser beam back and forth through the flame, while keeping it in focus. More details on the burner and measurement technique are provided in Ch. 5, where these experiments are discussed in detail.

CHAPTER 3

Mean Liftoff Heights

Before the temporal behavior of h is discussed in Ch. 4, the time-averaged liftoff heights are discussed in this chapter. Previous results of other researchers are first reviewed in Sec. 3.1. These findings led to the development of a model by Dr. R. C. Miake-Lye and myself which implicates the large-scale strain rate as the criterion which determines the liftoff height; this model is discussed in Sec. 3.2. Results on mean liftoff heights from the current work are presented in Sec. 3.3.

3.1 Previous Measurements

Vanquickenborne and Van Tiggelen (1966) measured mean liftoff heights of methane using nozzle diameters of 1.3, 1.8, and 2.4 mm. Using such small nozzles limited the maximum Reynolds number attainable before blowout to $\sim$ 1,200. The most extensive set of measurements of mean liftoff heights was made by Kalghatgi (1984) who used as fuels CH_4, C_2H_4, H_2, and propane (C_3H_8). He used tubes for nozzles, similar to the current experiments. In Table 3.1 are listed the nozzle diameters used with each fuel along with a value of $\bar{h}/U_o$ obtained by fitting a line to the data in his figures.

An important experimental finding of Kalghatgi was that $\bar{h}$ is proportional to U_o. The slope of the line $\bar{h}/U_o$ depends on the fuel, but is essentially independent of nozzle diameter, once $\bar{h}$ is sufficiently far downstream.

Many of the data for H_2 were obtained with choked and underexpanded jets. For these data, Kalghatgi assumed an isentropic expansion to atmospheric pressure to determine an effective value of U_o.

Table 3.1: Liftoff Height Experiments of Kalghatgi (1984)		
fuel	nozzle diameters (mm)	$\bar{h}/U_o$ (ms)
H_2	1.08, 1.74, 2.95, 4.06, 5.03, 6.1	0.030
CH_4	4.06, 5.03, 6.1, 8.3, 10.1	2.4
C_3H_8	4.06, 5.03, 6.1, 8.3, 10.1	1.9
C_2H_4	4.06, 6.1, 8.3	0.67

Kalghatgi interpreted his experimental results by arguing that the speed of the gas just upstream of the stabilization position is equal to a turbulent flame speed, which depends on both the fuel's laminar flame speed and the turbulence properties. An alternative explanation of the results is presented in the following section.

3.2 Strain-Rate Model

The strain-rate model provides a plausible explanation for the experimental observations that, for a given fuel, the mean liftoff height is proportional to the fuel velocity exiting the nozzle, independent of the nozzle diameter. The model was initially developed by Dr. R. C. Miake-Lye. He and I worked out the details and conducted experiments to test one aspect of the model—the effect on the liftoff height of adding some air to the fuel (Miake-Lye and Hammer 1989).

The premise of the model is that the flame stabilizes where the strain rate is just low enough to allow burning without extinction, *i.e.*, at the critical strain rate of the fuel, σ_{cr}. Considering the large structure observed in non-reacting turbulent jets (*e.g.*, Dimotakis *et al.* 1983), the relevant strain rate is taken to be that between large turbulent structures. This strain rate must scale with the local large-scale variables U_{cl} and δ, where U_{cl} is the local centerline velocity and δ is the local jet width, taken to be the full visual width $0.44\,x$.

Because hydrocarbon fuels have reaction rates that are very sensitive to composition, with the highest reaction rates near stoichiometric conditions, the highest

strain rates that the flame can sustain also occur near stoichiometric conditions. Hence, this model also requires that the local mass fraction of fuel Y be at the stoichiometric value $Y_{\rm st}$.

In the derivation that follows, as well as throughout this thesis, two often-used quantities are the equivalent source velocity $U_{\rm s}$ and source diameter $d_{\rm s}$. They are defined in terms of the momentum flux J_o and mass flux $\dot{m}_o$ exiting the nozzle by the solution of the equations

$$\begin{aligned} \dot{m}_o &= \rho_\infty \frac{\pi}{4} d_{\rm s}^2 U_{\rm s} \\ J_o &= \rho_\infty \frac{\pi}{4} d_{\rm s}^2 U_{\rm s}^2 \ . \end{aligned} \tag{3.1}$$

The quantitative predictions of this model are derived by considering the similarity laws of non-reacting, turbulent jets. As a result, the model is applicable only to flames stabilized a sufficient distance from the nozzle exit. In the jet far field, the mean velocity is described by

$$\bar{u} = C_u U_{\rm s} \frac{d_{\rm s}}{x} f_u(\eta) \ , \tag{3.2}$$

and the mean concentration by

$$\bar{Y} = C_Y Y_o \frac{d_{\rm s}}{x} f_Y(\eta) \ . \tag{3.3}$$

The large scale strain rate σ_L is given by

$$\sigma_L \sim \frac{U_{\rm cl}}{\delta} f_\sigma(\eta) \ . \tag{3.4}$$

Noting that $\delta \sim x$ and using Eq. 3.2 results in the similarity law

$$\sigma_L = C_\sigma \frac{U_{\rm s} d_{\rm s}}{x^2} f_\sigma(\eta) \ . \tag{3.5}$$

In these equations, C_u, C_Y, and C_σ are constants determined from experiments, Y_o is the initial mass fraction of fuel in the nozzle fluid with, the balance being air, η is the non-dimensional radial coordinate, r/x, and $f_u(\eta)$, $f_Y(\eta)$, and $f_\sigma(\eta)$ are similarity functions, also determined from experiments, where possible.

The radial flame location will fluctuate, approximately tracking the position where instantaneously $Y = Y_{st}$; this will be distributed around the point where $\bar{Y} = Y_{st}$. For simplicity in describing the strain-rate model, it is assumed that $\bar{Y} = Y_{st}$. Additionally it is assumed that σ_L is equal to the critical strain rate for the fuel, σ_{cr}. A more detailed consideration of the statistics of the strain-rate and concentration fields would not alter the qualitative predictions of the model.

Solving for d_s/x from Eq. 3.3 with $\bar{Y} = Y_{st}$,

$$\frac{d_s}{x} = \frac{1}{C_Y} \frac{Y_{st}}{Y_o} \frac{1}{f_Y(\eta)} ; \tag{3.6}$$

putting this into Eq. 3.5 and setting $x = \bar{h}$ results in the expression for the mean liftoff height

$$\bar{h} = \frac{C_\sigma}{C_Y} \frac{Y_{st}}{Y_o} \frac{U_s}{\sigma_{cr}} \frac{f_\sigma(\eta)}{f_Y(\eta)} , \tag{3.7}$$

where η is given by Eq. 3.3 as

$$\eta = f_Y^{-1} \left(\frac{1}{C_Y} \frac{Y_{st}}{Y_o} \frac{\bar{h}}{d_s} \right) . \tag{3.8}$$

If the the strain-rate profile and concentration profile are the same, *i.e.*, if $f_\sigma(\eta) = f_Y(\eta)$ for $\eta_{min.} \leq \eta \leq \eta_{max.}$, then the strain-rate model predicts a linear relation between $\bar{h}$ and U_s,

$$\bar{h} = C_s \frac{Y_{st}}{Y_o} \frac{U_s}{\sigma_{cr}} . \tag{3.9}$$

Without this assumption about the strain rate and concentration profiles, the model's predictions can be written as

$$\frac{Y_{st}}{Y_o} \frac{\bar{h}}{d_s} = \frac{C_\sigma}{C_Y} \left(\frac{Y_{st}}{Y_o} \right)^2 \frac{1}{\sigma_{cr}} \frac{U_s}{d_s} f_{srm} \left(f_Y^{-1} \left(\frac{1}{C_Y} \frac{Y_{st}}{Y_o} \frac{\bar{h}}{d_s} \right) \right) , \tag{3.10}$$

where

$$f_{srm}(\eta) \equiv f_\sigma(\eta)/f_Y(\eta) . \tag{3.11}$$

This equation implicitly expresses the non-dimensional liftoff height $(Y_{st}/Y_o)\bar{h}/d_s$ as a function of a non-dimensional velocity $(Y_{st}/Y_o)^2(1/\sigma_{cr})U_s/d_s$.

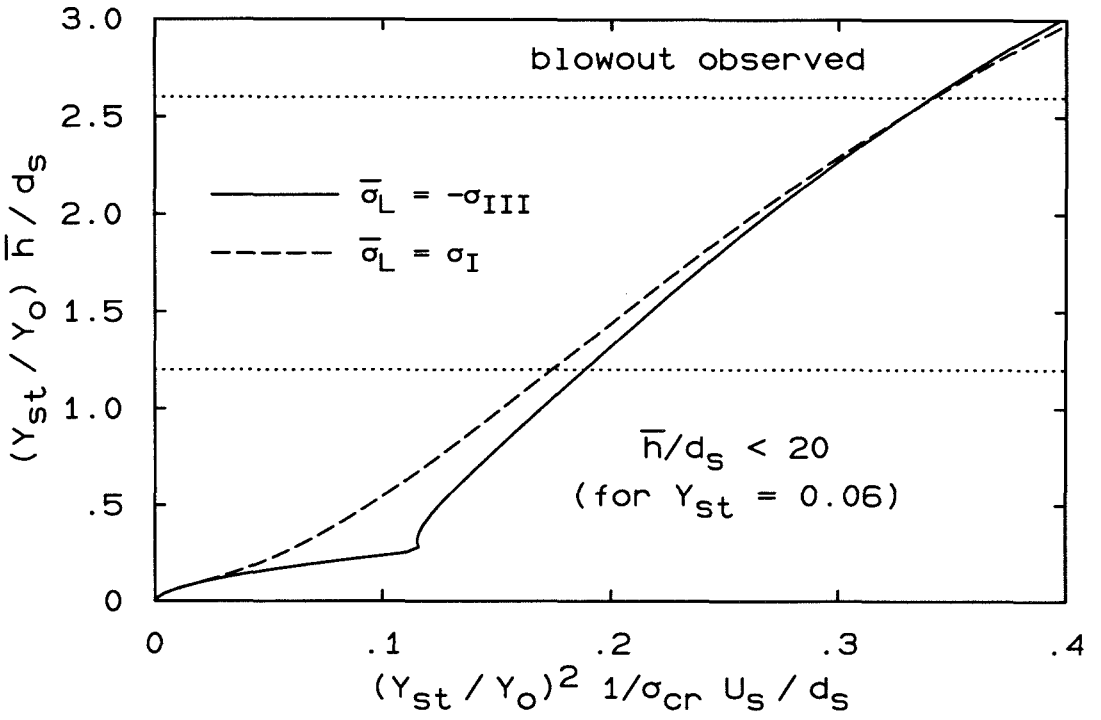

FIG. 3.1 Non-dimensional liftoff height *vs.* velocity as predicted by the strain-rate model, when σ_L is approximated by the largest principal compressive $(-\bar{\sigma}_{III})$ or extensive $(\bar{\sigma}_I)$ strain rate of the mean flow field.

To solve for $(Y_{st}/Y_o)\bar{h}/d_s$ requires knowledge of the two functions $f_Y(\eta)$ and $f_\sigma(\eta)$. Chen and Rodi (1980) recommend

$$f_Y(\eta) = e^{-C'_Y \eta^2} \tag{3.12}$$

with $C'_Y = 57$. The relevant strain rate for flame stabilization is that produced by the large structures of the turbulence. This is difficult to measure, and therefore only an approximate treatment is possible. One choice is to use the maximum principal strain rate obtained from the mean velocity field for σ_L, even though this may not be a very good approximation to the relevant strain rate produced by the turbulence. Using the expression from Chen and Rodi (1980) for the velocity function,

$$f_u(\eta) = e^{-C'_u \eta^2} \tag{3.13}$$

with $C'_u = 94$, the principal strain rates can be calculated, as discussed in Sec. A.2. Choosing either the maximum compressive strain rate $(-\bar{\sigma}_{III})$ or the maximum ex-

tensive strain rate ($\bar{\sigma}_{\rm I}$) allows Eq. 3.10 to be solved for $(Y_{\rm st}/Y_o)\bar{h}/d_{\rm s}$ as a function of $(Y_{\rm st}/Y_o)^2 U_{\rm s}/d_{\rm s}$. The solutions for both choices are shown in Fig. 3.1. Below the bottom dotted line, $(Y_{\rm st}/Y_o)\bar{h}/d_{\rm s} < 1.2$, which corresponds to $\bar{h}/d_{\rm s} < 20$ for $Y_{\rm st}/Y_o = 0.06$. This may be too close to the nozzle origin for the far-field equations to apply. (The kink in the $\sigma_L = -\bar{\sigma}_{\rm III}$ curve is a result of a change in the strain-rate component of maximum compression to the azimuthal component for low $(Y_{\rm st}/Y_o)\bar{h}/d_{\rm s}$, or large η.) Above the top dotted line, $(Y_{\rm st}/Y_o)\bar{h}/d_{\rm s} > 2.6$, where flames cannot be stabilized. Between the two dotted lines, both curves show an approximately linear relationship, with a negative virtual origin on the liftoff height axis. This is an indication that the strain-rate model does a reasonable job of predicting a linear relation between $\bar{h}$ and $U_{\rm s}$. Because the mean strain-rate field was used for approximating $f_\sigma(\eta)$ while the turbulence will cause the true variation of σ_L with η will be different, the model's actual predictions may differ from Fig. 3.1. As long as the effective strain rates increase as η is reduced (moving toward the jet centerline) in approximately the same way as the concentration profile, the strain rate model predicts a linear $\bar{h}$ *vs.* $U_{\rm s}$ relation.

Table 3.2: Strain-Rate Model Predictions

fuel	$\tau_{\rm lo} \equiv \bar{h}/Y_{\rm st}\,U_{\rm s}$ (ms)	$1/\sigma_{\rm ext}$ (ms)	$\tau_{\rm lo}\,\sigma_{\rm ext}$	κ/S^2 (ms)	$\tau_{\rm lo}\,S^2/\kappa$
CH_4	43.2	3.13	13.8	0.698	61.9
C_2H_4	10.4	–	–	0.174	59.8
C_3H_8	31.2	2.86	10.9	0.503	62.0
H_2	1.04	0.0769	13.5	0.012	86.0

In addition to predicting a linear relation between $\bar{h}$ and $U_{\rm s}$, a correct model for liftoff must predict the observed slope of the $\bar{h}/U_{\rm s}$ line for different fuels. A comparison of experimental results with model predictions is made in Table 3.2. An effective chemical time $\tau_{\rm lo}$ can be defined for each fuel with the equation

$$\bar{h} = Y_{\rm st}\,\tau_{\rm lo}\,U_{\rm s}\ , \tag{3.14}$$

where $\bar{h}/U_s$ is taken from experimental data. In the second column of Table 3.2 Kalghatgi's experimental liftoff results have been used to estimate η_o. These values can be compared to properties of the fuels which provide estimates of the critical strain rates. In the third column, the extinction limits of laminar, counterflow diffusion flames are listed. Values for CH_4 and C_3H_8 were taken from Tsuji and Yamaoka (1969), and the value for H_2 was taken from Dixon-Lewis *et al.* (1986). Although the combustion in a lifted turbulent jet flame does not take place at the interface between pure fuel and pure air because of premixing upstream of the flame base, σ_{ext} is used as an approximate measure of σ_{cr}. Flames with partial premixing have higher extinction limits than pure diffusion flames. For instance, Mastorakos *et al.* (1992) found that the extinction limit of counterflow diffusion flames of 20 % CH_4 / 80 % air is $\sigma_{ext} = 600\ s^{-1}$, compared with $350\ s^{-1}$ for pure CH_4. The fourth column of Table 3.2 is the ratio of the second and third columns, aiding comparison of the model's predictions for the different fuels. That the numbers in the fourth column are reasonably close to one another provides support for the strain-rate model. Using the definition of η_o from Eq. 3.14 along with Eqs. 3.2, 3.13, and 3.3, it can be shown that $\bar{\sigma}_I\,\eta_o \approx 7.5$ for $Y_{st}\bar{h}/d_s = 1.5$ to 2.5, where $\bar{\sigma}_I$ is calculated on the contour $\bar{Y} = Y_{st}$. That the values in the fourth column of Table 3.2 are in the neighborhood of 7.5 indicates that the strain rates at the flame base, as estimated by $\bar{\sigma}_I$, are close to (but slightly less than) σ_{ext}. It is likely that the turbulence increases the strain rates above that obtained from the mean velocity field. However, premixing of fuel and air will increase the maximum sustainable strain rates.

As an alternative estimate for the critical strain rate, S^2/κ is tabulated in the fifth column of Table 3.2, where κ is the thermal diffusivity and S is the laminar flame speed. Because κ/S^2 is a relevant chemical time in premixed flame propagation (*e.g.*, Glassman 1977), its inverse, which has dimensions of a strain rate, can be thought of as a characteristic maximum strain rate of the fuel. In the table, κ is defined as $k_f/\rho_{st}\,C_{p,st}$ where k_f is the thermal conductivity of the reacted mixture, here estimated as that of nitrogen at the adiabatic flame temperature, ρ_{st} is the

density of the unburned, stoichiometric mixture, and $C_{p,st}$ is the specific heat of the unburned mixture. As with the estimates of σ_{cr} based on σ_{ext}, κ/S^2 provides a reasonable collapse of the liftoff data for the fuels, as seen by the reasonable agreement between the numbers in the sixth column of Table 3.2.

3.3 Current Measurements

Measurements of the time-varying liftoff height were made as described in Ch. 2 using a linear photodiode array. From these measurements mean values were easily obtained. Two sets of measurements are reported in this chapter. First, liftoff heights of pure fuels for various nozzle diameters and exit velocities are reported, then measurements of $\bar{h}$ with premixing of air with the fuel are presented.

3.3.1 Details of the Measurement Technique

In making the measurements reported in this chapter, for each nozzle used, the array and camera lens were positioned at a vertical height equal to the liftoff height in the middle of the range of $\bar{h}$ to be measured, specifically, $\bar{h}$ for which $Y_{st}\bar{h}/d_s = 2.2$. The horizontal distance from the nozzle to the array was chosen such that the flame width just filled the lateral extent of the array when the flame was at this middle height, as illustrated in Fig. 3.2. Because the optics were not moved as the liftoff height was changed, flames with $\bar{h}$ greater than the middle value had images somewhat wider than the array, and therefore the left and right sides of the image were chopped off. This was found to have a negligible effect on the mean value measured, however, as documented in Sec. D.6. For each condition, 8192 data points were acquired at a repetition time of 4.4 ms.

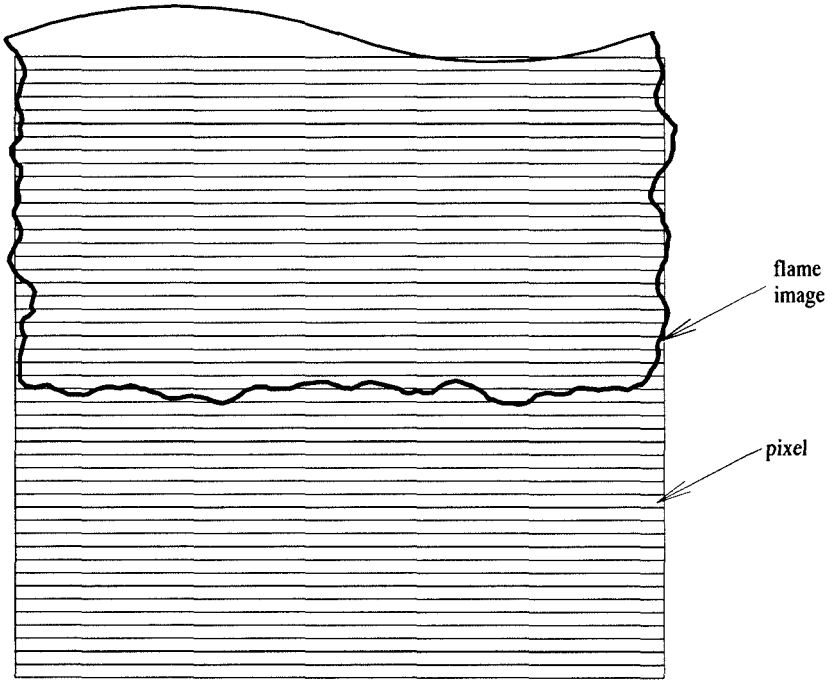

FIG. 3.2 Schematic showing the image of the flame on the linear array. Pixels are 50 times as wide as their vertical spacing.

3.3.2 Pure Fuels

The four fuels used in measurements of mean liftoff heights were natural gas, C_2H_6, C_2H_4, and C_2H_2. Properties of these fuels (molecular weight MW, Y_{st}, and adiabatic flame temperature rise ΔT_f) are listed in Table 3.3. The properties of H_2 are also listed because that fuel was used in experiments described in Ch. 4. The properties of natural gas were calculated from a sample analysis supplied by the gas company; the composition is given on p. 4. The flame temperatures and stoichiometric mass fractions for all the fuels were taken from Becker and Liang (1978). The three fuels C_2H_6, C_2H_4, and C_2H_2 were chosen in part because their molecular weights are close to that of air, thereby minimizing the effect of different jet and ambient densities; natural gas was used because of its convenience.

The flow conditions for the measurement of mean liftoff heights are listed in Table 3.4. For each fuel, three nozzle diameters were used, except for C_2H_2 for which only two nozzles were used. The corresponding minimum and maximum

Table 3.2: Properties of Fuels Used				
fuel	symbol	MW	Y_{st}	ΔT_f (K)
natural gas	see p. 4	17.1	0.0582	1925
ethane	C_2H_6	30.0	0.0584	1959
ethylene	C_2H_4	28.0	0.0633	2069
acetylene	C_2H_2	26.0	0.0700	2239
hydrogen	H_2	2.0	0.0284	2117

velocities for each fuel/nozzle combination are listed, along with the corresponding minimum and maximum liftoff heights. All of the measurements discussed in this chapter are tabulated in Appendix B.

Table 3.4: Conditions of $\bar{h}$ Measurements Without Air Premixing					
fuel	d (mm)	min. U_s (m/s)	max. U_s (m/s)	min. $\bar{h}$ (mm)	max. $\bar{h}$ (mm)
n.g.	4.61	33	56	89	164
	6.25	42	74	133	229
	7.73	39	90	137	272
C_2H_6	3.12	46	71	74	124
	3.88	48	93	89	180
	4.61	58	111	115	210
C_2H_4	2.16	73	127	44	91
	3.12	95	181	66	135
	3.88	111	200	82	143
C_2H_2	1.02	173	240	20	37
	1.55	226	266	32	40

Mean liftoff heights *vs.* source velocity U_s are shown in Fig. 3.3 for natural gas using three different nozzle diameters. Details of the method used to calculate U_s and d_s can be found in Sec. A.1. From the figure, it can be seen that $\bar{h}$ is approximately proportional to U_s, although there is some variation with nozzle diameter.

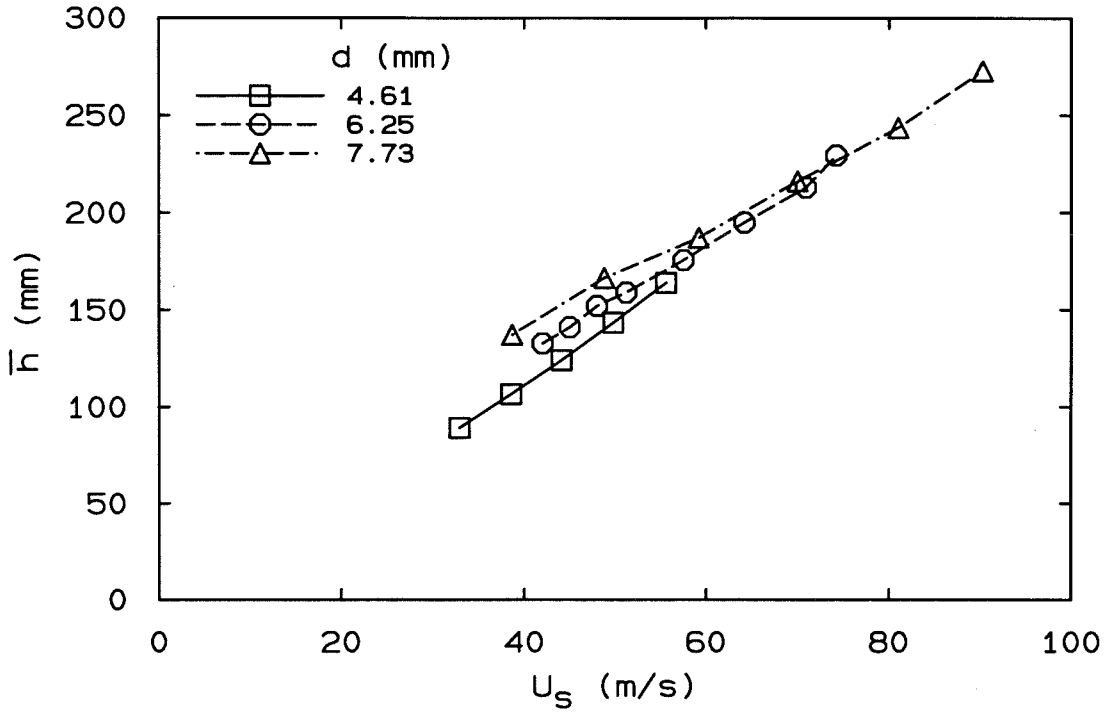

FIG. 3.3 Mean liftoff heights for natural gas, $d = 4.61$, 6.25, and 7.73 mm.

To see more clearly the effect of nozzle diameter it is useful to plot the data non-dimensionally. Recalling the discussion in Sec. 3.2, the proper non-dimensional variable for the liftoff height is $Y_{\rm st}\bar{h}/d_{\rm s}$ (for $Y_o = 1$). For a given fuel with known $Y_{\rm st}$ and MW, $\bar{h}/d_{\rm s}$ and $\bar{h}/d$, which are relevant to determining whether or not $\bar{h}$ is in the far field of the jet, are linearly related to $Y_{\rm st}\bar{h}/d_{\rm s}$. The proper variable to use for the velocity is less obvious. Following the strain rate model, a possibility is $Y_{\rm st}^2\tau_\chi U_{\rm s}/d_{\rm s}$, where τ_χ is a chemical time of the fuel. In the strain-rate model τ_χ is proportional to $1/\sigma_{\rm cr}$. Other models use $Y_{\rm st}^2\tau_\chi U_{\rm s}/d_{\rm s}$ as a non-dimensional velocity, with different choices of τ_χ, and possibly with $Y_{\rm st}$ replaced with another concentration, such as Y at the maximum laminar flame speed. To avoid choosing a chemical time τ_χ, $Y_{\rm st}\bar{h}/d_{\rm s}$ is plotted against $Y_{\rm st}^2 U_{\rm s}/d_{\rm s}$ in Fig. 3.4, making the slope of each line on the plot have dimensions of ms. The slope of a line is then the effective value of $\tau_{\rm lo}$, defined as $\bar{h}/U_{\rm s}\,d_{\rm s}$ in Eq. 3.14. Values of $\bar{h}/d_{\rm s}$ and $\bar{h}/d$ are labeled along the right side of the plot.

From Fig. 3.4 it can be seen that changing the nozzle diameter does have a

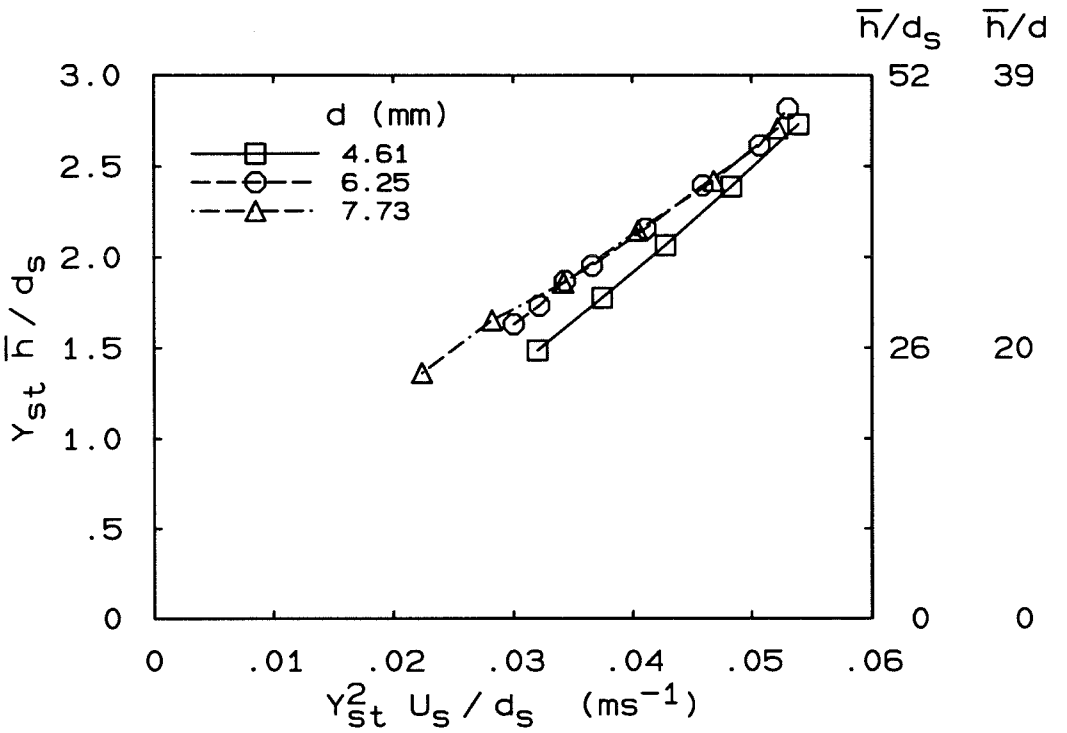

FIG. 3.4 Normalized mean liftoff heights *vs.* normalized velocity for natural gas. Values of $\bar{h}/d_s$ and $\bar{h}/d$ are shown along the right side of the graph.

slight effect on the normalized liftoff height. As d is increased from 4.61 mm to 6.25 mm, $Y_{st}\bar{h}/d_s$ at a constant $Y_{st}^2 U_s/d_s$ increases. However, there is no further increase in going to the 7.73 mm nozzle. It is possible that the changing Reynolds number is responsible for this behavior in which the normalized liftoff height first increases, and then remains constant with further increase in the Reynolds number. The Reynolds number in the far field of the jet is defined as

$$Re_\infty \equiv \frac{U_s\, d_s}{\nu_\infty} \,, \tag{3.15}$$

and is approximately equal to the Reynolds number just below the flame base Re_h, which is defined in Sec. A.5. The ranges of Re_∞ corresponding to the data points in Figs. 3.3 and 3.4 are: for the 4.61 mm nozzle, 7,300 to 12,000; for the 6.25 mm nozzle, 13,000 to 22,000; and for the 7.73 mm nozzle, 14,000 to 34,000. The density in the flame is lower than ρ_∞ and the viscosity is higher than μ_∞, making the effective Reynolds number in the flame considerably lower than Re_∞. Therefore, it is plausible that variation of Reynolds number could have an effect on these flames

even with $Re_\infty > 15{,}000$.

As larger nozzle diameters are used, the required velocity for a given non-dimensional liftoff height increases, and eventually, compressibility effects become important, at least in some region of the jet near the nozzle exit. Because the speed of sound in the fuel a_o is in general not equal to that in the air a_∞, there is some ambiguity in the exact definition of a Mach number. Here, the Mach number of the jet will be defined as $M_s \equiv U_s/a_\infty$. Because most of the fuels studied (C_2H_6, C_2H_4, and C_2H_2) have speeds of sound close to that of air, the precise definition of M_s will not qualitatively change the arguments presented here.

For the natural gas results shown in Fig. 3.4 it is unlikely that the change in M_s is responsible for the variation with nozzle diameter, since the maximum value of M_s achieved in natural gas experiments was 0.26. However, this may not be true for all of the fuels, as is discussed below.

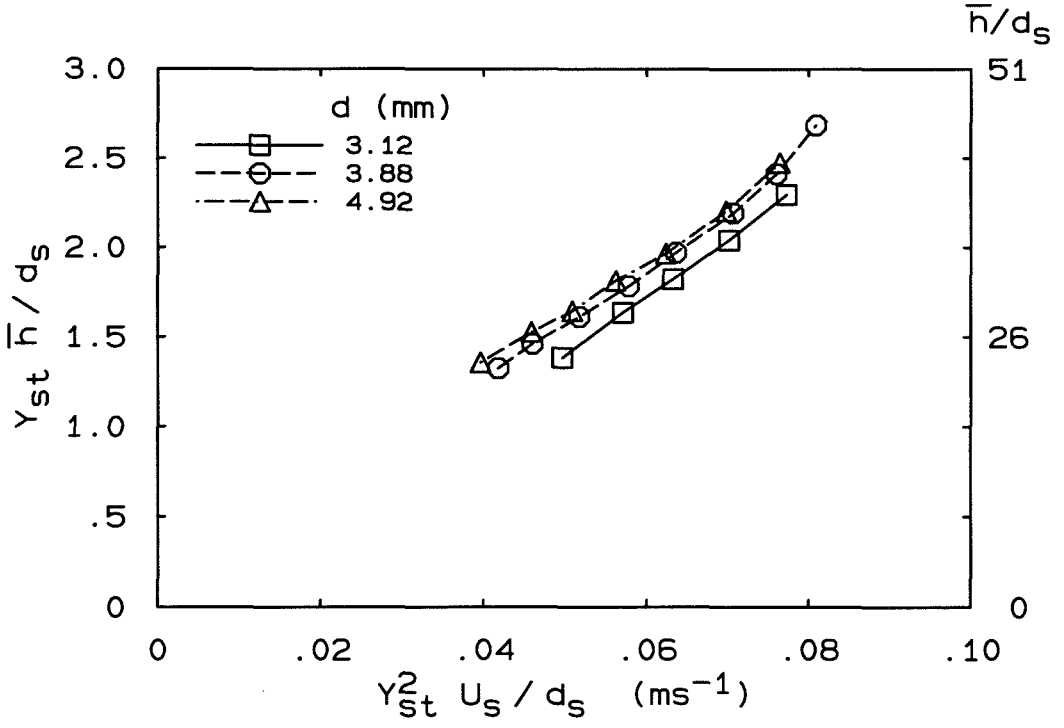

FIG. 3.5 Normalized liftoff height *vs.* normalized velocity for C_2H_6, $d = 3.12$, 3.88, and 4.92 mm.

The second fuel used in these experiments was C_2H_6. The mean liftoff heights are plotted in Fig. 3.5, where U_s and $\bar{h}$ have been normalized as was done with natural gas in Fig. 3.4. Because $d_s \approx d$ for C_2H_6, only values of $\bar{h}/d_s$ are labeled along the right side of the plot. The variation with nozzle diameter (or Reynolds number) is slight; the ranges of Re_∞ for the C_2H_6 data plotted are: for the 3.12 mm nozzle, 9,000 to 14,000; for the 3.88 mm nozzle, 12,000 to 23,000; and for the 4.92 mm nozzle, 18,000 to 35,000. Although the data from the last two nozzles do not collapse completely, there is less variation in liftoff height in changing from the 3.88 mm nozzle to the 4.92 mm nozzle, than in changing from the 3.12 mm nozzle to the 3.88 mm nozzle. As with the natural gas experiments, compressibility effects should be insignificant, as the highest Mach number realized for C_2H_6 was $M_s = 0.32$.

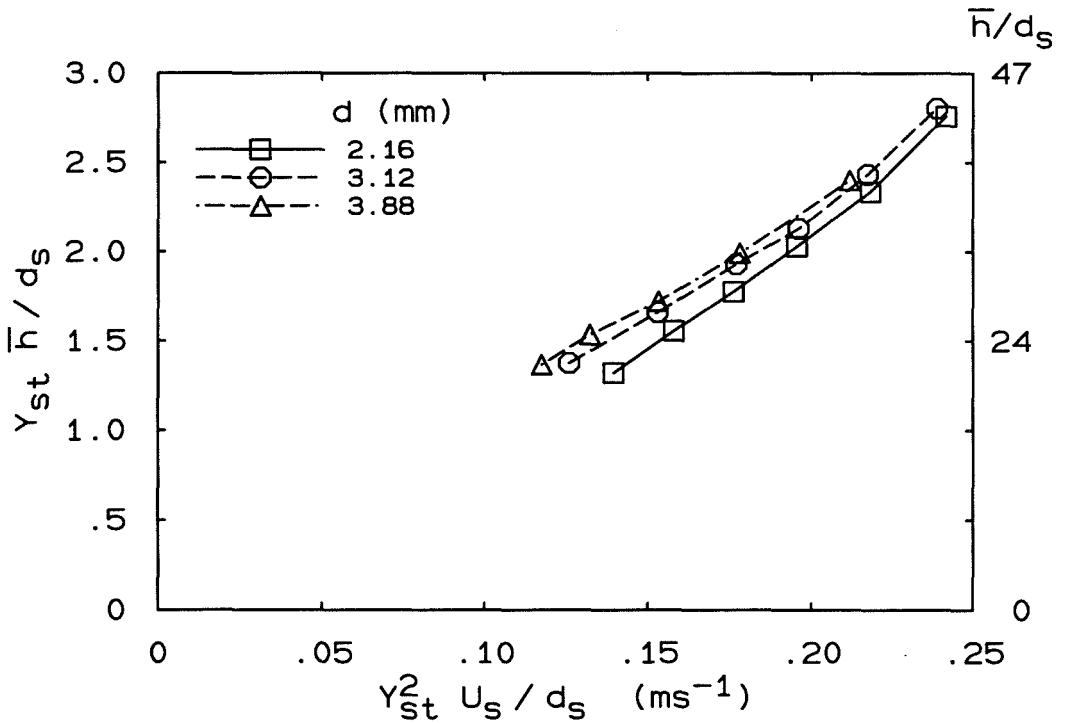

FIG. 3.6 Normalized liftoff height *vs.* normalized velocity for C_2H_4, $d = 2.16$, 3.12, and 3.88 mm.

C_2H_4 reacts faster than C_2H_6 and consequently higher velocities are needed to achieve the same liftoff height. Figure 3.6 is a plot of normalized liftoff height *vs.*

velocity for nozzle diameters of 2.16, 3.12, and 3.88 mm. Again, as d is increased, $Y_{st}\bar{h}/d_s$ increases slightly at a fixed value of $Y_{st}^2 U_s/d_s$, but the effect is smaller in going from the 3.12 mm to the 3.88 mm nozzle than going from the 2.16 mm to the 3.12 mm nozzle. The ranges of Re_∞ for the various nozzles are: for the 2.16 mm nozzle, 9,700 to 17,000; for the 3.12 mm nozzle, 18,000 to 35,000; and for the 3.88 mm nozzle, 27,000 to 48,000. This range of Re_∞ spans the range explored with the natural gas and C_2H_6 flames in which no Reynolds number effect was found above $\sim$ 13,000 for natural gas, and little Reynolds number effect found above 20,000 for C_2H_6. Therefore, the continued increase in $Y_{st}\bar{h}/d_s$ with Re_∞ for C_2H_4 requires another explanation.

Possibly compressibility effects are beginning to affect the data. The Mach number ranges for the nozzles are: for the 2.16 mm nozzle, M_s = 0.21 to 0.37; for the 3.12 mm nozzle, 0.28 to 0.52; and for the 3.88 mm nozzle, 0.32 to 0.58. It is possible that close to the nozzle where velocities are high, reduced entrainment in the mixing layer (Papamoschou 1988), caused by the high Mach numbers, effectively acts to create a virtual origin downstream of the nozzle exit. Assuming that this virtual origin is the same for all properties of the jet (concentration, velocity, strain rates, *etc.*), this would cause $Y_{st}\bar{h}/d_s$, for which no virtual origin effect has been considered, to increase.

Finally, mean liftoff height data for C_2H_2 are shown in Fig. 3.7. The achievable conditions for C_2H_2 were limited by the allowable delivery pressure for that gas of 15 psig. When the data for the 1.02 mm nozzle are extrapolated to $U_s = 0$, a line drawn through the data intersects the vertical axis at a large, negative non-dimensional distance. Although still having a negative intercept on the vertical axis, the intercept is smaller for the 1.55 mm nozzle. As with ethylene, an increase in diameter results in an increase in $Y_{st}\bar{h}/d_s$. The ranges of Re_∞ in Fig. 3.7 are: for the 1.02 mm nozzle, 11,000 to 15,000; and for the 1.55 mm nozzle, 20,000 to 24,000. The Mach numbers are the highest of all the fuels used in this study: 0.51 to 0.69 for the 1.02 mm nozzle and 0.64 to 0.76 for the 1.55 mm nozzle.

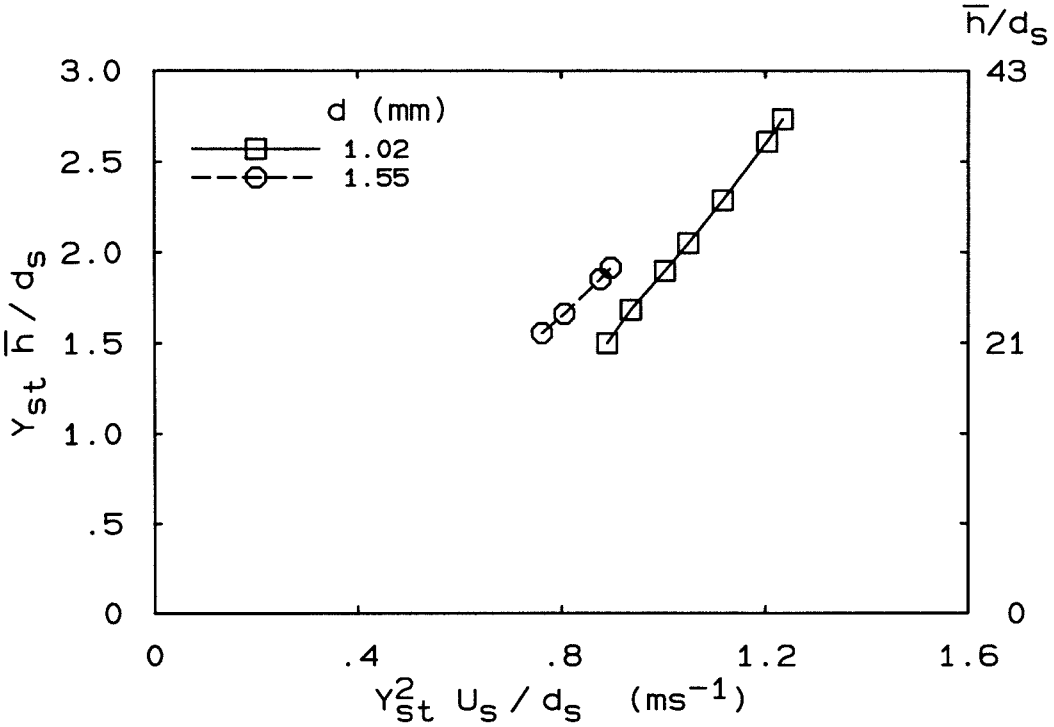

FIG. 3.7 Normalized liftoff height *vs.* normalized velocity for C_2H_2, d = 1.02 and 1.55 mm.

To better illustrate the effects of Re_∞ and M_s on mean liftoff heights, data from all four fuels have been plotted on a single graph, Fig. 3.8. This was done by selecting a single value of $Y_{st}\bar{h}/d_s = 2.0$ and plotting the corresponding value of $Y_{st}^2 U_s/d_s$ *vs.* Re_∞. Because the four fuels have vastly different effective chemical times τ_{lo}, each curve has been normalized by the value of $Y_{st}^2 U_s/d_s$ at Re_∞ = 15,000, to bring the curves onto the same scale and force them all to pass through the point (15,000, 1). With this normalization, the value of Y_{st} for each fuel does not affect the vertical axis, and has been left off the vertical axis label. One point for C_2H_2 had to be extrapolated from the data because the highest liftoff height reached for the 1.55 mm nozzle was $Y_{st}\bar{h}/d_s = 1.9$.

As the Reynolds number is increased, the velocity needed to reach $Y_{st}\bar{h}/d_s = 2.0$ decreases. All the fuels do not lie on a single curve, however, indicating that Re_∞ is not the only parameter causing this decrease. The curves for natural gas and C_2H_6 level out at Re_∞ = 15,000 and 18,000, respectively, while those of C_2H_4 and C_2H_2

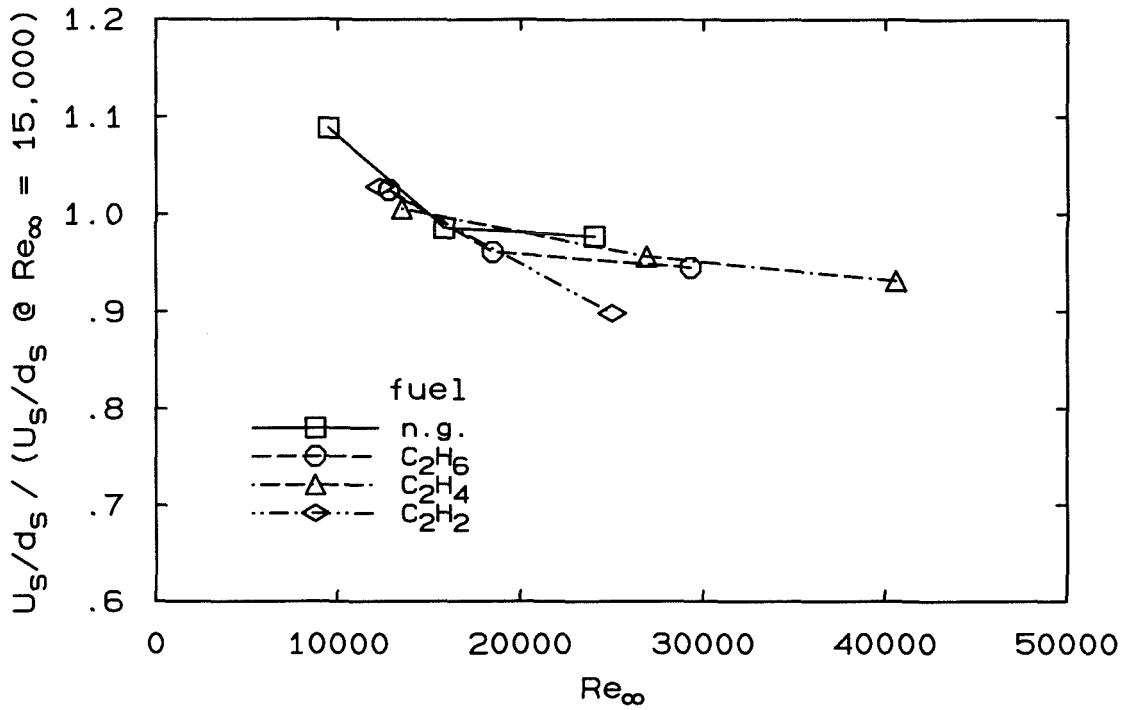

FIG. 3.8 Normalized velocity $Y_{st}^2 U_s/d_s$ at $Y_{st}\bar{h}/d_s = 2.0$ *vs.* Reynolds number Re_∞, for all four fuels. The curves have been normalized to pass through the point (15,000, 1) to allow all fuels to be displayed on one plot.

continue to fall. It is possible that this continued decrease for the latter two fuels is actually caused by an increase in Mach number, which presumably decreases the mixing in the region near the nozzle, creating a virtual origin downstream of the nozzle exit. It is also possible, however, that these two fuels simply have a different dependence on Re_∞, which results from details of the chemical reaction mechanism.

As discussed in Dimotakis (1993), there is evidence of a transition in the behavior of turbulent jets in the Reynolds number range of the current experiments. Gilbrech (1991) measured flame lengths of low-heat-release gas flames. He fit his results to an equation of the form

$$\frac{\bar{L}}{d_s} = A\,\phi + B\,, \tag{3.16}$$

where $\bar{L}$ is the mean flame length and ϕ is the stoichiometric air to fuel ratio, $1/Y_{st} - 1$. The stoichiometric coefficient A and the normalized virtual origin B were both found to depend on Reynolds number. In particular, A was found to

decrease as Re_∞ increases from 10,000 to 20,000, above which the Reynolds number dependence was found to be less, if any, at least up to 150,000.

For natural gas and C_2H_6, the change in liftoff height behavior shown in Fig. 3.8 occurs at approximately the same value of Re_∞ as the change in A shown in Gilbrech's Fig. 4.8 (Fig. 7 in Dimotakis 1993). The other two fuels plotted in Fig. 3.8 may have compressibility effects, as discussed above. (In the flame-length study, the Mach number did no change with Re_∞ because Re_∞ was controlled by adjusting the pressure in the reaction chamber.) Dimotakis notes that many other flows, in particular the shear layer, have a transition in this same range of Re_∞.

A property of the jet which changes with Re_∞ is the strain rate at the smallest scale of the flow. The strain rate at the Kolmogorov scale, σ_K, is proportional to $\sigma_L \, Re_\infty^{1/2}$. This increase in σ_K with Re_∞ may have the effect of destabilizing the flame, causing it to move to a slightly higher position, where both σ_L and σ_K are lower. Why the effect would diminish above $Re_\infty \approx 20{,}000$ is not clear, however.

To get an idea of the liftoff behavior for even larger Reynolds numbers, the results of Birch and Hargrave (1989) can be examined. They studied very large natural gas flames in which the jet was choked and underexpanded, using pressures up to 28 bar. By assuming an isentropic expansion to ambient pressure from sonic conditions at the nozzle exit, an equivalent source velocity can be calculated, and an equivalent source diameter can be similarly calculated. (For isentropic flow equations, see, *e.g.*, Liepmann and Roshko 1957, pp. 53, 126.) In Fig. 3.9a their measured mean liftoff heights are plotted *vs.* the calculated source velocity U_s for nozzle diameters of 50.6 mm and 111.2 mm, along with data from the current experiments using a 6.25 mm nozzle. $\bar{h}/U_s$ is $\sim$ 3.2 ms for the 50.6 mm nozzle, and ranges from $\sim$ 3.4 to 4.4 ms for the 111.2 mm nozzle, all reasonably close to the value of 3.1 ms measured in the current experiments (Fig. 3.3). Re_∞ ranges from 1.2×10^6 to 6.2×10^6 for the 50.6 mm nozzle, and from 1.6×10^6 to 7.5×10^6 for the 111.2 mm nozzle, more than 200 times as large as in the current experiments.

The data are plotted again in Fig. 3.9b, using the same normalization as in

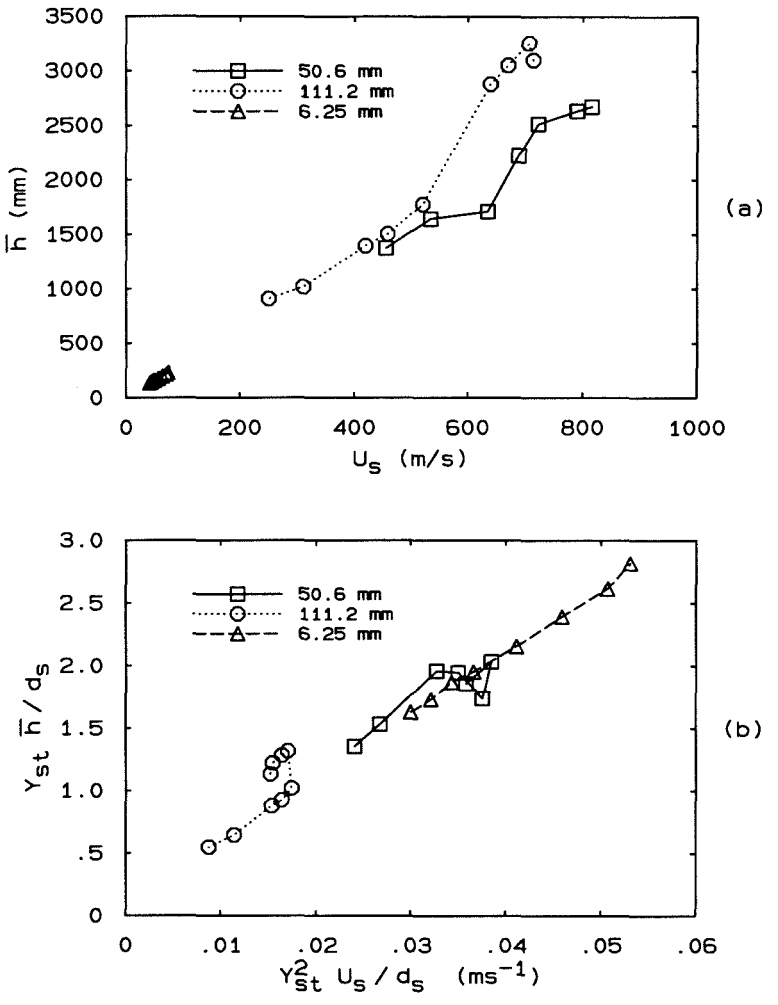

FIG. 3.9 Mean liftoff heights for natural gas, from Birch and Hargrave (1989), along with the current results for a 6.25 mm nozzle. (a) dimensional, (b) normalized.

Fig. 3.4. Because the calculated value of d_s changes as the stagnation pressure is changed, the shapes of the curves are different from Fig. 3.9a. There are multiple values of the abscissa, because U_s/d_s reaches a maximum at an intermediate pressure and then decreases. The left-most point on Fig. 3.9b for the 50.6 mm nozzle corresponds to the right-most point in Fig. 3.9a. For the 111.2 mm nozzle, however, the left-most points of each plot correspond. As long as the flames are out of the near field of the jet, the value of $\bar{h}/U_s$ is approximately the same as for the much smaller nozzles of the current experiments.

3.3.3 Fuels Premixed with Air

Experiments were conducted in which the fuel was premixed with air prior to exiting the nozzle. The strain-rate model described in Sec. 3.2 predicts that when air is added to the nozzle fluid reducing the initial mass fraction of fuel in the nozzle fluid Y_o, $\bar{h} \propto (1/Y_o)$ for a given fuel and source velocity. These experiments were conducted largely to test this prediction. Several other models of liftoff which use far-field scaling of jets make this same prediction, as summarized in Hammer (1990).

Miake-Lye and Hammer (1989) conducted experiments in which the nozzle diameter was kept constant and Y_o was varied. In that study, as Y_o was reduced, the slope of the liftoff curve exceeded predictions. Because those experiments were conducted with the nozzle diameter fixed while Y_o was varied, the Reynolds number dropped as Y_o was decreased.

In the current experiments, however, the nozzle diameter was changed systematically to keep the Reynolds number range of the experiments the same at each value of Y_o. For each fuel, this meant keeping $Y_o d_s$ constant so that at a given value of $(Y_{st}/Y_o)^2 U_s/d_s$ (at which $(Y_{st}/Y_o)\bar{h}/d_s$ is predicted to be fixed) Re_∞ will be fixed, for any value of Y_o. This is more clearly seen by examining the equation

$$Re_\infty \equiv (U_s\, d_s)/\nu_\infty = (1/Y_{st})^2\, [(Y_{st}/Y_o)^2 U_s/d_s]\, [Y_o\, d_s]^2/\nu_\infty \ . \qquad (3.17)$$

The specific conditions that were studied are listed in Table 3.5. Experiments were done with natural gas, C_2H_6, and C_2H_4, using four nozzles and four corresponding values of Y_o for each fuel.

Data from measurements using natural gas are plotted in Fig. 3.10 for several values of Y_o. For all the curves plotted, the range of Re_∞ is $\sim$ 6,000 to 12,000, which is too low to rule out effects of Re_∞ on the data. The Mach numbers M_s are all less than 0.2, which is sufficiently low to have negligible compressibility effects. The strain-rate model predicts that all of the curves would lie on top of one another. However, as more air is added to the nozzle fluid, the slope of the curve increases,

Table 3.5: Conditions of $\bar{h}$ Measurements with Air Premixing						
fuel	d (mm)	Y_o	min. U_s (m/s)	max. U_s (m/s)	min. $\bar{h}$ (mm)	max. $\bar{h}$ (mm)
n.g.	4.61	1	33	56	89	164
	4.92	0.92	25	51	75	169
	6.25	0.69	19	38	73	181
	7.73	0.53	15	30	68	189
C_2H_6	3.88	1	47	89	91	170
	4.92	0.79	37	68	89	168
	6.25	0.63	30	55	88	186
	7.73	0.50	24	41	77	168
C_2H_4	2.16	1	74	127	44	93
	3.12	0.69	48	83	39	91
	3.88	0.55	38	63	34	91
	4.92	0.43	30	49	27	92

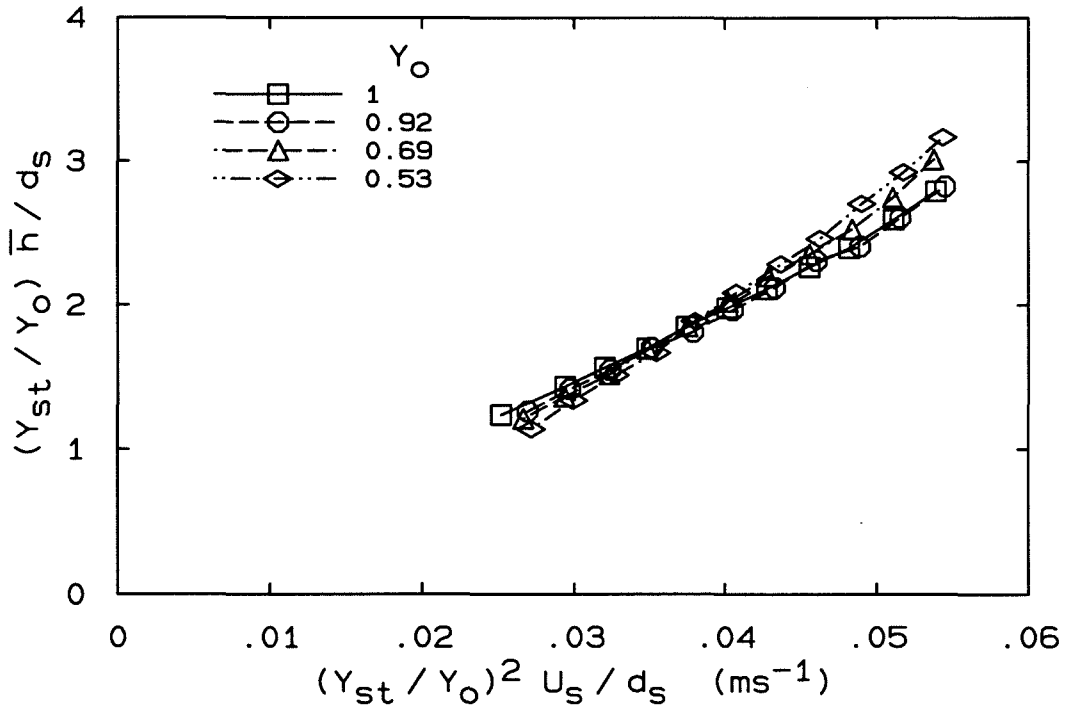

FIG. 3.10 Normalized liftoff height *vs.* normalized velocity for natural gas, for varying fuel mass fraction Y_o in the nozzle fluid.

creating a fan pattern. When Y_o is small, at low velocities the liftoff heights are lower than predicted, and at high velocities liftoff heights are higher than predicted.

One possible reason for the disagreement between experimental results and the model is that as Y_o is decreased, the flames are stabilized closer to the nozzle ($\bar{h}/d_s$ is reduced) thereby moving out of the far field of the jet where self-similar behavior is most completely achieved. Additionally, there may be some complicated Reynolds number effects in this range of Re_∞. These issues are discussed later in this section, following the presentation of all of the experimental data.

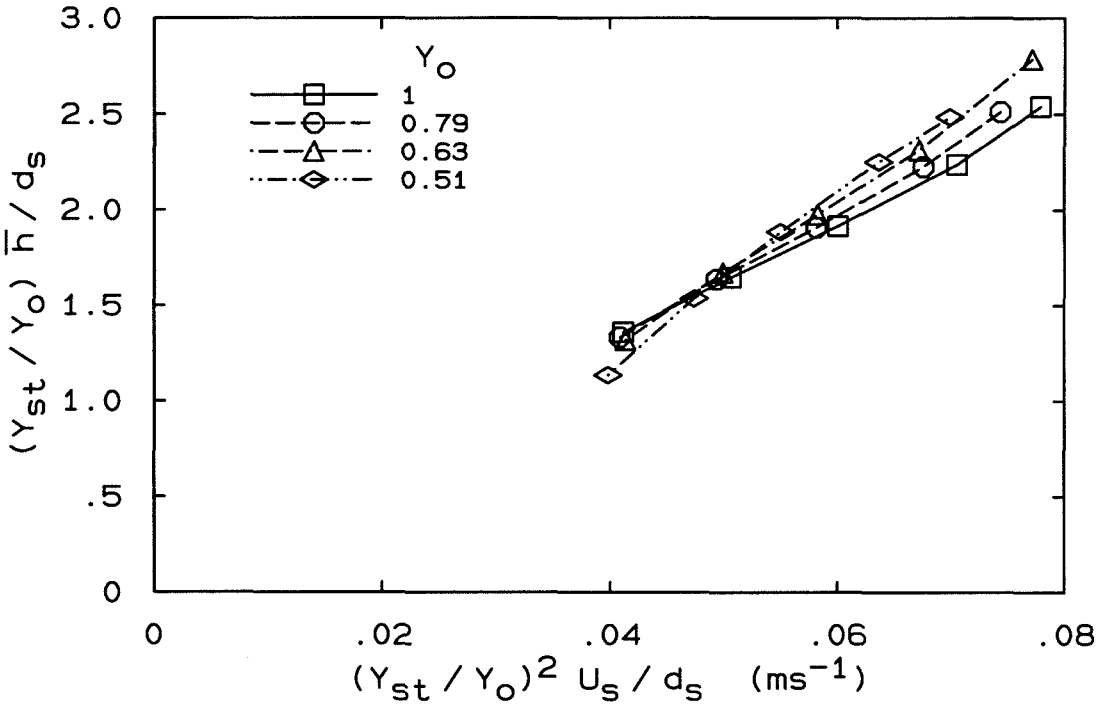

FIG. 3.11 Normalized liftoff height *vs.* normalized velocity for C_2H_6, for varying fuel mass fraction Y_o in the nozzle fluid.

Results similar to those using natural gas were obtained for C_2H_6 as shown in Fig. 3.11. Again, as Y_o is reduced, the slope of the line increases. The range of Re_∞ for each of the curves in Fig. 3.11 is $\sim$ 12,000 to 20,000, and the maximum Mach numbers M_s are 0.26, 0.20, 0.16, and 0.12 for Y_o = 1, 0.79, 0.63, and 0.51, respectively. This is still in the range where Re_∞ could have an effect, although these values of Re_∞ are roughly twice as high as in the natural gas flames (Fig. 3.10).

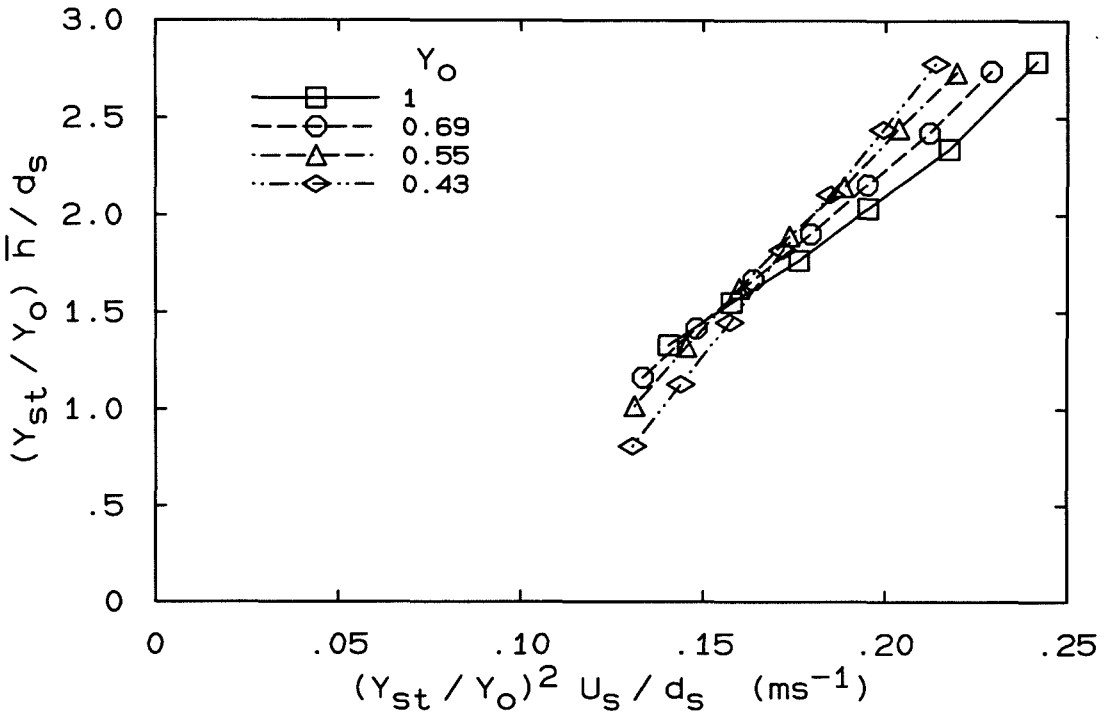

FIG. 3.12 Normalized liftoff height *vs.* normalized velocity for C_2H_4, for varying fuel mass fraction Y_o in the nozzle fluid.

Experiments with air premixing were also performed using C_2H_4. The results are plotted in Fig. 3.12 and show behavior similar to the previous fuels. The slope of the line increases as Y_o is reduced. For each of the curves in Fig. 3.12 the range of Re_∞ is $\sim$ 9,000 to 16,000, falling in between those of the natural gas and C_2H_6 flames. The maximum values of M_s are 0.37, 0.24, 0.18, and 0.14 for $Y_o = 1$, 0.69, 0.55, and 0.43, respectively.

Figure 3.13 shows more clearly how the slope of the liftoff curve changes with Y_o. Here, the slope of each of the lines of Figs. 3.10 through 3.12 are plotted against $1/Y_o$. Each slope was found by fitting a parabola through the data and taking the derivative at the point where $(Y_{st}/Y_o)\bar{h}/d_s = 2.0$, *i.e.*,

$$\frac{\mathrm{d}[(Y_{st}/Y_o)\bar{h}/d_s]}{\mathrm{d}[(Y_{st}/Y_o)^2 U_s/d_s]} \text{ at } (Y_{st}/Y_o)\bar{h}/d_s = 2.0\ . \tag{3.18}$$

Each slope was then normalized by the slope for $Y_o = 1$.

As increased amounts of air are added to the nozzle fluid, the slope of the curve increases, in disagreement with predictions based on far-field scaling of turbulent

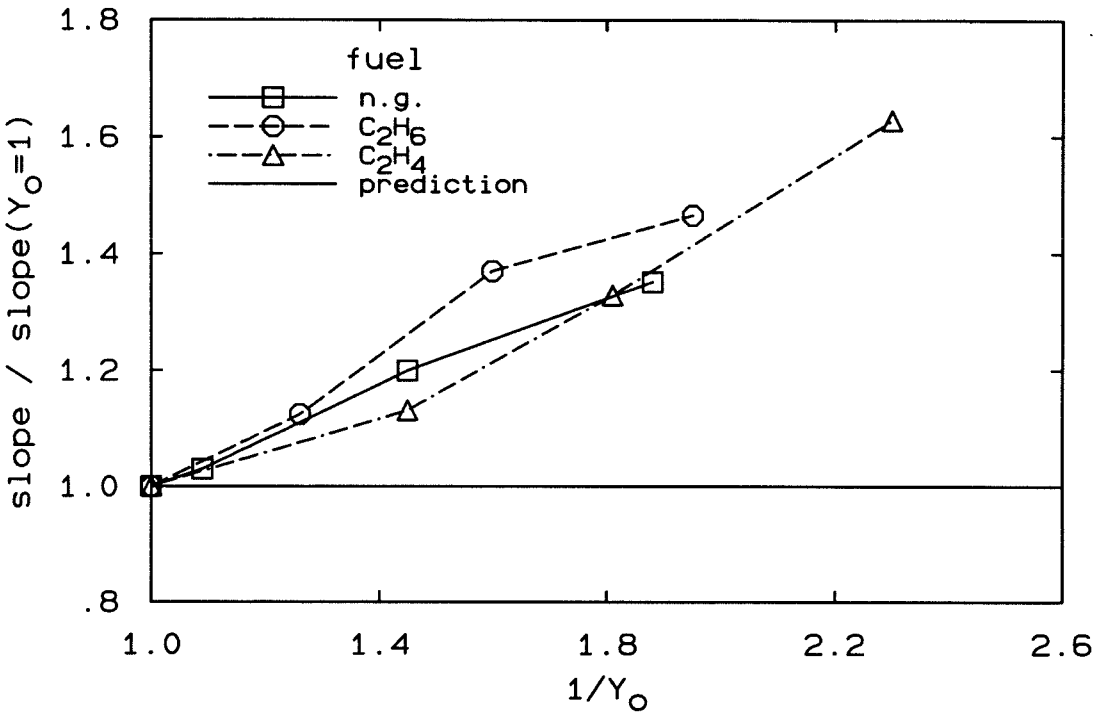

FIG. 3.13 Variation of the slope of the curve of $(Y_{st}/Y_o)\bar{h}/d_s$ *vs.* $(Y_{st}/Y_o)^2 U_s/d_s$ at $(Y_{st}/Y_o)\bar{h}/d_s = 2.0$ with Y_o. The slopes have been normalized by the slope for $Y_o = 1$.

jets, as was used in the strain-rate model described in Sec. 3.2. Although there is some scatter in this plot, there is a reasonable collapse for the different fuels. Such a collapse was not obtained in the results of Miake-Lye and Hammer (1989), presumably because of the changing Reynolds number as Y_o was changed.

As mentioned above, near-field effects and Reynolds number effects may be responsible for the discrepancy between experimental results and predictions based on far-field scaling. In particular, the mixing virtual origin found by Gilbrech (1991) in his study of flame lengths may be important. The normalized mixing virtual origin, B, (see Eq. 3.16 and the discussion in Sec. 3.3.2) was found to have a strong dependence on Reynolds number in the range $10{,}000 < Re_\infty < 150{,}000$.

The non-dimensional liftoff height can be defined to include a virtual origin x_o (in general, different from the flame length virtual origin), *i.e.*,

$$\frac{Y_{st}}{Y_o}\left(\frac{\bar{h} - x_o}{d_s}\right) .$$

Considering first the results for natural gas, if this quantity is plotted on the vertical axis of Fig. 3.10, the effect would be to shift the curves down for $Y_o < 1$, assuming x_o/d_s is positive and independent of Re_∞. This would not collapse the data for different Y_o. To collapse the data, x_o/d_s would need to be ~ -4 at $Re_\infty = 6{,}000$ and $+6$ at $Re_\infty = 12{,}000$. This can be compared with the flame-length results, in which B was found to increase from 17 to 28 as Re_∞ increases from 10,000 to 20,000. The required change in x_o/d_s with Re_∞ is therefore comparable to that observed in the flame-length studies (although the range of Re_∞ is different). However, a negative virtual origin would be required at the lower values of Re_∞, and this is in contrast to the flame-length results. The flame lengths measured were 60 to 130 diameters from the nozzle exit, and so it would not be expected that the extrapolated origin B would be the same as x_o/d_s of the current measurements which were made in the range of $\bar{h}/d_s = 10$ to 40.

The C_2H_6 results plotted in Fig. 3.11 show the same behavior as the natural gas results. However, the values of Re_∞ are roughly twice as high as in the natural gas flames (Fig. 3.10). As a result, Re_∞ at the lower liftoff heights of Fig. 3.11 is approximately equal to Re_∞ at the upper liftoff heights of Fig. 3.10. The required dependence of x_o/d_s on Re_∞ is then different for the C_2H_6 and natural gas results. This rules out the possibility that it is a change in virtual origin with Re_∞ that is responsible for the results for premixing with air. Although there are Reynolds number effects, they are not the dominant reason for the lack of a collapse at the different values of Y_o.

A possible explanation for the systematic variation with Y_o seen in Figs. 3.10 to 3.13 can be obtained by modifying the strain-rate model to allow two different virtual origins, one for the concentration field and one for the strain-rate field. Equation 3.3 for the concentration field is modified to have a virtual origin x_Y,

$$\bar{Y} = C_Y Y_o \frac{d_s}{(x - x_Y)} f_Y\big(y/(x - x_Y)\big) , \qquad (3.19)$$

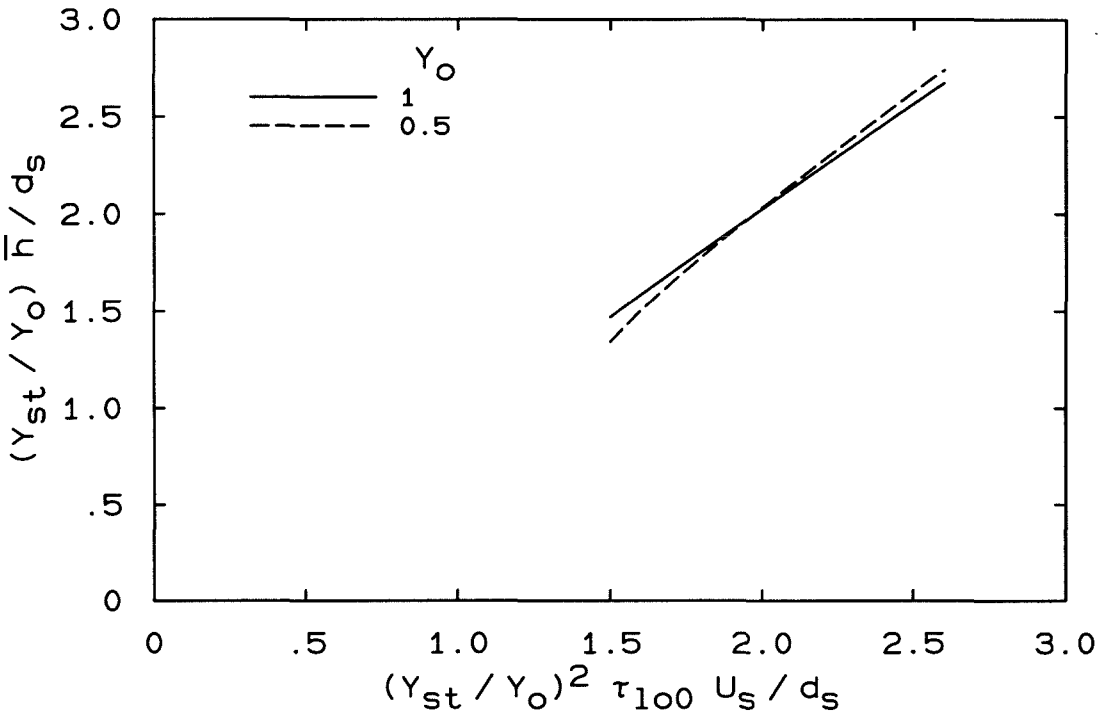

FIG. 3.14 Normalized liftoff height *vs.* normalized velocity using Eqs. 3.19, 3.20, and 3.21 in the strain-rate model. $Y_{\rm st} = 0.06$, $x_Y/d_{\rm s} = 0.5$, and $x_\sigma/d_{\rm s} = 1.75$.

and Eq. 3.5 is allowed to have a different virtual origin x_σ,

$$\sigma_L = C_\sigma \frac{U_{\rm s}\, d_{\rm s}}{(x - x_\sigma)^2} f_\sigma\big(y/(x - x_\sigma)\big) \ . \tag{3.20}$$

To ensure a linear relationship when $x_Y = x_\sigma = 0$, it is assumed that

$$f_\sigma(\eta) = f_Y(\eta) = e^{-C'_Y \eta^2} \ . \tag{3.21}$$

Making the substitution $\tau_{\rm loo} = C_\sigma/(C_y\, \sigma_{\rm cr})$, $(Y_{\rm st}/Y_o)\bar{h}/d_{\rm s}$ can be found as a function of $(Y_{\rm st}/Y_o)^2 \tau_{\rm loo} U_{\rm s}/d_{\rm s}$, for choices of the virtual origins, x_Y and x_σ. (With this definition of $\tau_{\rm loo}$, when $x_Y = x_\sigma = 0$, $(Y_{\rm st}/Y_o)\bar{h}/d_{\rm s} = (Y_{\rm st}/Y_o)^2 \tau_{\rm loo} U_{\rm s}/d_{\rm s}$.)

It is assumed that $x_Y/d_{\rm s}$ and $x_\sigma/d_{\rm s}$ are not changed by varying Y_o. For choices of $x_Y/d_{\rm s} = 0.5$ and $x_\sigma/d_{\rm s} = 1.75$, and with $Y_{\rm st} = 0.06$, the results of the calculation for $Y_o = 1$ and $Y_o = 0.5$ are shown in Fig. 3.14. Here, the same qualitative behavior is obtained as in the data. As Y_o is reduced, the slope of the curve increases. However, the magnitude of the change is less than observed. The ratio of the slope

of the $Y_o = 0.5$ curve to the $Y_o = 1.0$ curve at $(Y_{st}/Y_o)\bar{h}/d_s = 2.0$ is only 1.14, less than the experimental value of 1.5 obtained from Fig. 3.13.

There is not much room for adjusting the values of the virtual origins. x_σ must be greater than x_Y to have the slope increase as Y_o is decreased. Increasing x_Y/d_s and x_σ/d_s by the same amount has the effect of moving the $Y_o = 0.5$ curve up more than the $Y_o = 1$ curve, without changing the slope. If larger values of $(x_\sigma - x_Y)/d_s$ are tried, no solution can be found for the lower values of the non-dimensional velocity, because the $\sigma_L = \sigma_{cr}$ curve is moved entirely inside the $\bar{Y} = Y_{st}$ curve, *i.e.*, the flames should begin at the nozzle exit.

Although the details of the actual physical process of the flame stabilization certainly deviate from the above model, this does provide a possible qualitative explanation for the observed variation of liftoff height with Y_o and U_s.

CHAPTER 4

Fluctuations of the Liftoff Height

Measurements of liftoff height *vs.* time can reveal information concerning the dynamics of lifted flames. In this chapter aspects of the temporal fluctuations in liftoff height are examined. The motivation for making these measurements was to gain insight into the stabilization process. Particular issues of interest are whether the magnitude of the fluctuations scales with the local large scale of the jet, whether the time scale of the fluctuations scales with the local passage time of large structures, and whether the liftoff height fluctuates primarily at one frequency. It was hoped that answering these questions would help elucidate the importance of large turbulent structures to the flame stabilization mechanism.

To enable accurate analyses of the data, the measurements reported in this chapter were made for longer times than those of Ch. 3. For most of the conditions, 131072 (2^{17}) data points were acquired. Exceptions to this were the measurements of Sec. 4.4 where h and the flame length were measured simultaneously and those of Sec. 4.5, where h and the flame radiation were measured simultaneously, in both of which 65536 measurements of h were acquired.

One difference in the experimental procedure for the data of this chapter from that of Ch. 3 is that the array was repositioned for each flow condition. The vertical height of the array was adjusted to be at the mean liftoff height, and the horizontal distance from the flame to the array was chosen such that the flame image just filled the lateral extent of the linear array, as illustrated in Fig. 3.2. This was done to prevent any systematic error related to either, the fraction of the flame width imaged, or, the relative spatial resolution, from contaminating the results; both of these factors were kept constant for all the conditions reported in this chapter.

Setting a sufficiently low threshold for determining h would allow the lowest point anywhere along the flame base to be recorded as the liftoff height. To distinguish the flame light from noise in the data, a sufficiently large threshold had to be set; the technique therefore required that a large enough amount of light be present to call that position h. To a reasonable approximation, however, the liftoff heights measured in these experiments represent the lowest position along the lateral extent of the flame base where burning exists.

4.1 Fluctuation Amplitudes of the Liftoff Height

Before discussing the temporal behavior of $h(t)$, results on the spatial scales of the fluctuations are presented. This includes measures such as the probability density function (pdf) and root-mean-square (rms) of the liftoff height.

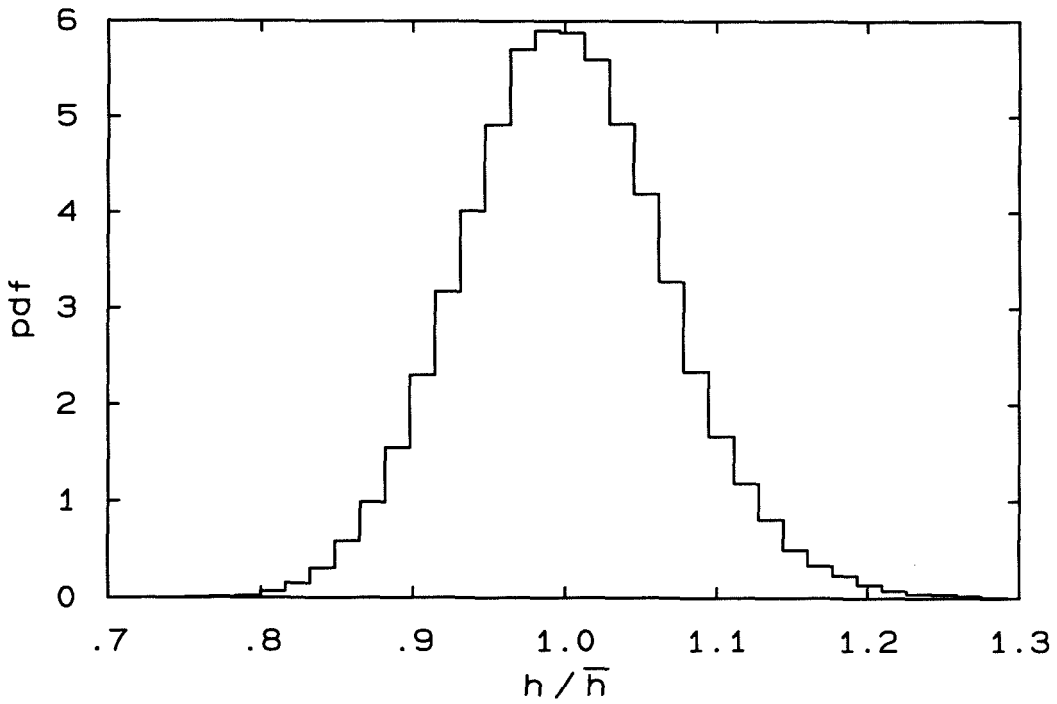

FIG. 4.1 Probability density function (pdf) of liftoff height. C_2H_6, $d_s = 3.88$ mm, $U_s = 88$ m/s, $\bar{h} = 151$ mm.

Table 4.1: Flow Conditions Studied, Group A Nozzles					
fuel	d (mm)	U_s (m/s)	$\bar{h}$ (mm)	Re_h	$\tau_{1/2}$ (ms)
n.g.	4.61	36	88	8,500	58.6
		47	116	10,900	63.7
		57	144	13,000	76.9
		65	172	14,600	110.1
C_2H_6	3.88	56	98	15,700	39.6
		74	124	20,000	41.8
		88	151	23,500	51.8
		96	166	25,300	66.9
C_2H_4	2.16	83	49	12,400	21.0
		98	59	14,300	20.5
		116	74	16,900	22.7
		127	83	18,200	25.5
C_2H_2	1.02	173	20	11,800	10.9
		193	24	12,900	10.1
		219	30	14,300	10.1
		235	34	15,200	10.6

The histogram of h from one of the flow conditions is shown in Fig. 4.1, where the rectangular bins each have a width corresponding to two pixels on the linear array. In the limit of infinitesimal bin size, the histogram would converge to the true pdf. The curve has been normalized such that its area is one, *i.e.*,

$$\int_0^\infty \mathrm{pdf}(h/\bar{h})\,\mathrm{d}(h/\bar{h}) \;=\; 1 \;. \tag{4.1}$$

The pdf is mono-modal, centered approximately at the mean and reasonably symmetric. The maximum excursions of h from the mean are $\sim \pm 0.25\,\bar{h}$, making the range of the fluctuations just larger than the local jet diameter, $\delta = 0.44\,\bar{h}$. For these data the rms level h' is $0.066\,\bar{h}$, which is slightly less than our earlier measurements (Miake-Lye and Hammer 1989) in which $h'/\bar{h}$ was found to be ~ 0.08 for a wide range of liftoff heights. That the spatial scale of the fluctuations is comparable to the jet large scale is consistent with the idea of large-scale structures of the

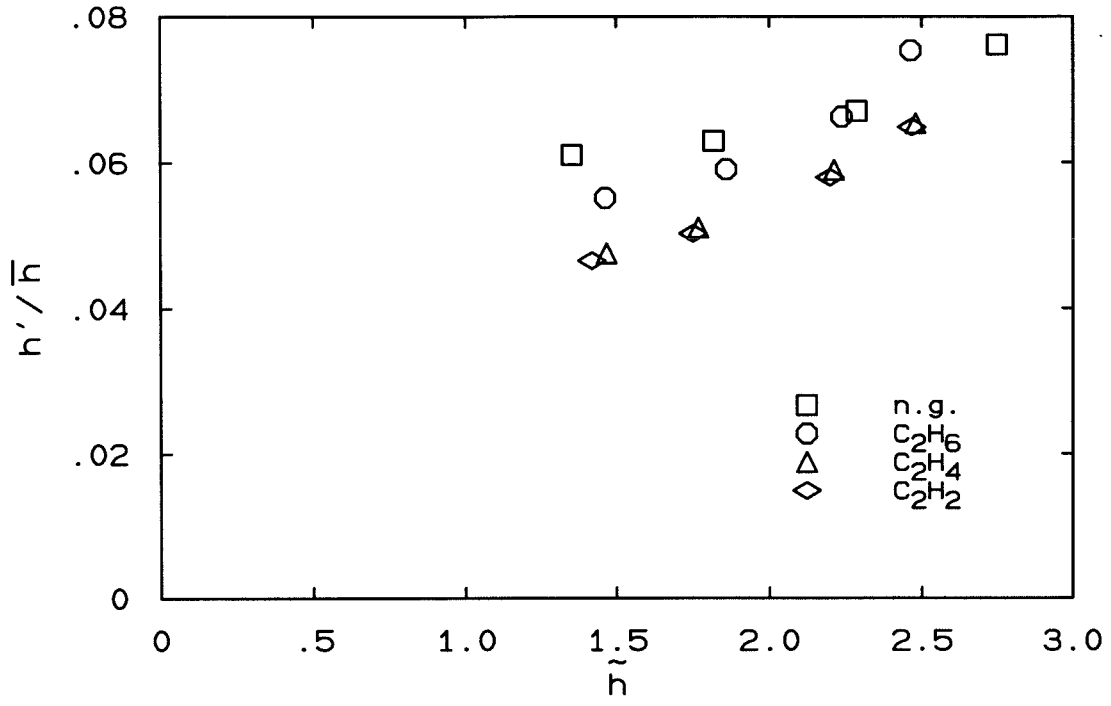

FIG. 4.2 Normalized rms level $h'/\bar{h}$ *vs.* normalized liftoff height for the conditions listed in Table 4.1 (group A nozzles).

turbulence governing the dynamics of the liftoff height.

For each of the first four fuels listed in Table 3.3, experiments were conducted with two nozzles. This allowed two different Reynolds numbers to be investigated at each non-dimensional liftoff height. The conditions achieved with the smaller set of nozzles, denoted group A, are listed in Table 4.1, and those of the larger group of nozzles, group B, are listed in Table 4.2. The Reynolds number listed Re_h is the local Reynolds number just below the flame base, which is approximately equal to the far-field Reynolds number $Re_\infty \equiv U_s d_s/\nu_\infty$. Its precise definition is given in Sec. A.5. For each fuel, four different liftoff heights were studied, spanning the range of $\tilde{h}$ from $\sim$ 1.5 to 2.5, where $\tilde{h}$ is the non-dimensional liftoff height, which is approximately equal to $Y_{st}\bar{h}/d_s$. Its precise definition, which accounts for the fact that the density just below the liftoff height is not equal to ρ_∞, is given in Secs. 4.3 and A.4. Having $\tilde{h} \geq 1.5$ ensured that all flames were lifted to at least $20\,d_s$. For the three pure fuels, $d_s \approx d$, and so all flames were lifted to at least 20 nozzle

diameters. For natural gas, all flames were lifted to at least 16 nozzle diameters.

A quantity derivable from the pdf is the rms of the fluctuations, h'. By making accurate measurements of h over a wide range of conditions, the current experiments are able to provide more information on the fluctuation levels of lifted flames than previous investigations. In Fig. 4.2 the normalized rms level $h'/\bar{h}$ is plotted against normalized liftoff height for all the conditions listed in Table 4.1. These rms values have been corrected for the finite sampling time of the linear array as described in Appendix C.

Table 4.2: Flow Conditions Studied, Group B Nozzles

fuel	d (mm)	U_s (m/s)	$\bar{h}$ (mm)	Re_h	$\tau_{1/2}$ (ms)
n.g.	7.73	46	148	17,900	60.9
		61	183	23,800	62.0
		79	221	30,300	69.7
		90	245	34,300	81.9
C_2H_6	4.92	68	125	24,000	38.7
		90	157	31,000	43.5
		109	187	36,700	53.9
		120	214	39,800	80.4
C_2H_4	3.12	105	71	22,300	21.0
		128	87	26,700	22.7
		154	106	31,600	25.7
		171	121	34,700	31.0
C_2H_2	1.55	215	30	22,100	8.2
		254	38	25,500	8.7

The most apparent observation from Fig. 4.2 is that as $\tilde{h}$ increases, the normalized fluctuation level increases. Because the Reynolds number also increases as $\tilde{h}$ is increased, however, it can not be discerned simply from these data whether this increase in $h'/\bar{h}$ is caused by the change in liftoff height or by the accompanying change in Reynolds number. This issue is addressed below.

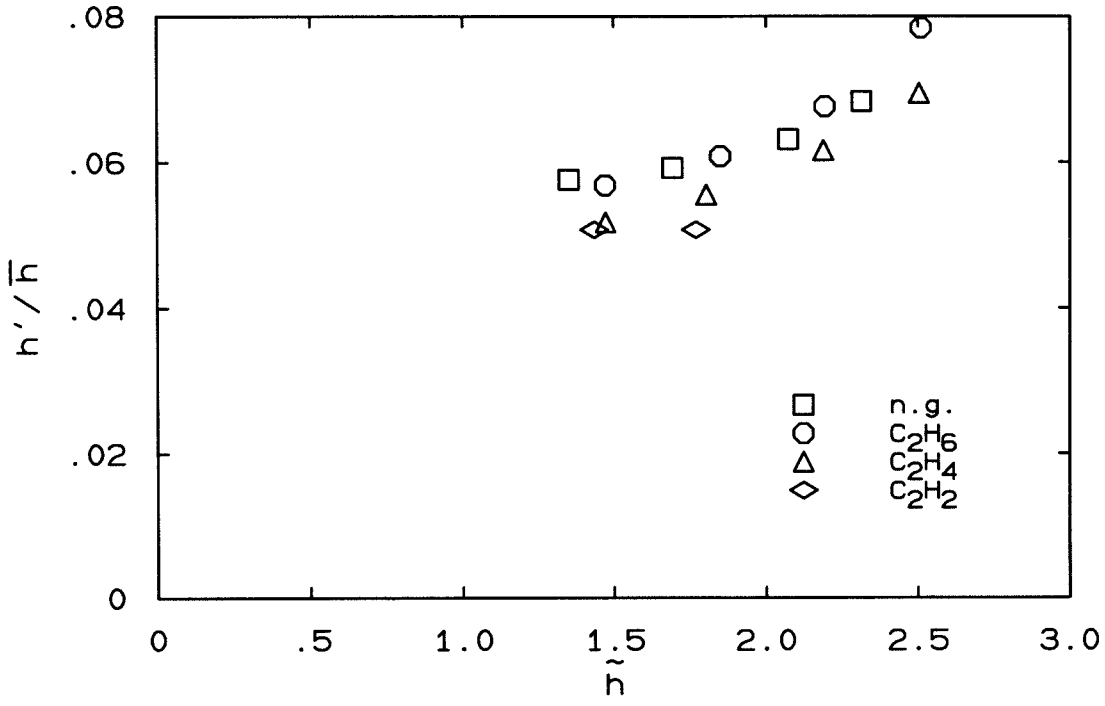

FIG. 4.3 Normalized rms level $h'/\bar{h}$ *vs.* normalized liftoff height for the conditions listed in Table 4.2 (group B nozzles).

The data from the different fuels do not collapse onto a single curve. In general, the rms levels for natural gas and C_2H_6 are higher than those of C_2H_4 and C_2H_2. It is not obvious why this should be the case. The time scale of the fluctuations decreases in the same order as the (first four) fuels listed in Table 3.3. The possibility that the finite sampling time of the measurements would cause lower *measured* rms levels for the faster fuels was considered, and ruled out, as discussed in Appendix C.

To investigate the effect of Reynolds number on the flames, larger nozzles of group B listed in Table 4.2 were used. The same range of $\tilde{h}$ was investigated, except that for acetylene, the maximum attainable value was 1.8 because of limitations on the delivery pressure of that gas. These Reynolds numbers are roughly twice as large as those of the group A nozzles.

The relative fluctuation levels $h'/\bar{h}$ are not significantly different from those of the smaller nozzles of group A, as shown in Fig. 4.3. The same general behavior is evident; as the liftoff height increases, the relative fluctuation level increases.

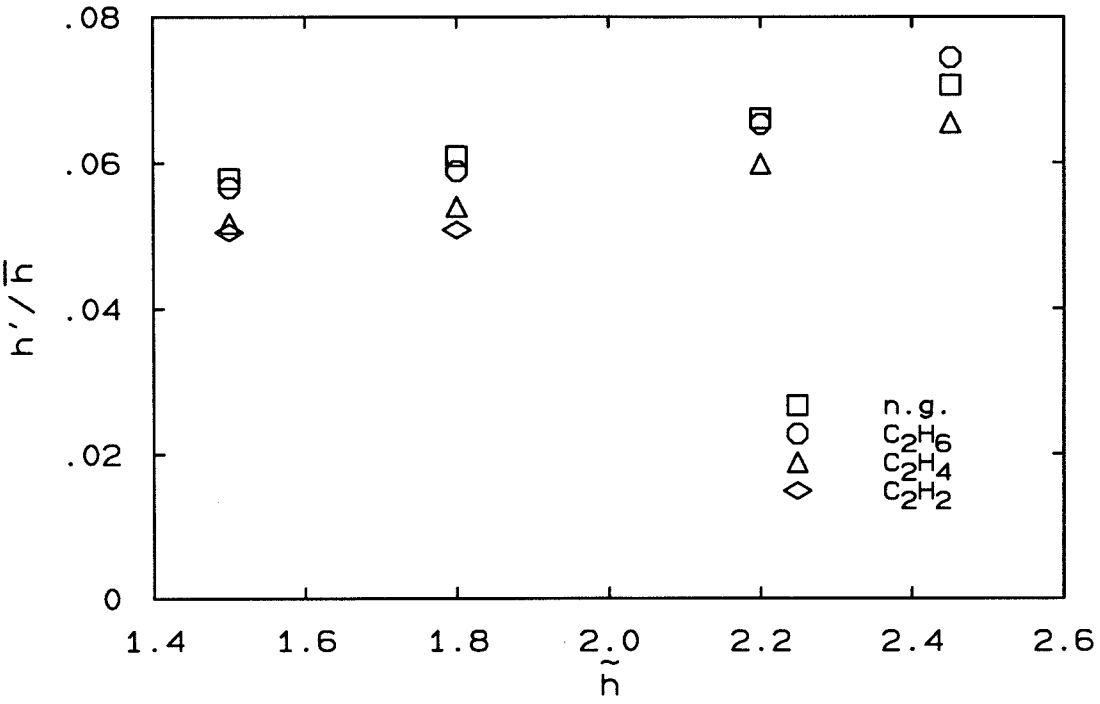

FIG. 4.4 Normalized rms level $h'/\bar{h}$ *vs.* normalized liftoff height. Data from group A and B nozzles interpolated to $Re_h = 22{,}000$.

To isolate the effects of $\tilde{h}$ from those of Re_h, interpolation was performed on the data from the group A and B nozzles to achieve a constant Reynolds number of 22,000. Before doing this interpolation, the data within each group of nozzles were interpolated to four values of $\tilde{h}$, namely 1.5, 1.8, 2.2 and 2.45. Then, at each value of $\tilde{h}$, the interpolation in Reynolds number was performed. The resulting plot is shown in Fig. 4.4, where the horizontal axis has been changed to include only the range of $\tilde{h}$ studied. Clearly, there is an increase in $h'/\bar{h}$ with $\tilde{h}$, even at a constant Re_h; as flames approach blowout, the relative fluctuation level increases.

4.2 Temporal Behavior Common to All Flames Studied

Several features of the liftoff height *vs.* time signals were found to be present in all the conditions studied, and these are illustrated by looking at results for a particular flow condition. The ways in which the behavior changes with flow conditions are examined in later sections.

The measurements of h *vs.* t revealed that fluctuations in h occur on much longer time scales than the large-scale time $\tau_\delta \equiv \delta(\bar{h})/U_{\rm cl}(\bar{h})$. This was not expected as it conflicted with ideas on the dynamics and structure of turbulent jets. A premise of the strain-rate model (Sec. 3.2) is that the passage of large, turbulent structures controls the liftoff height fluctuations, from which it would be expected that the fluctuations in liftoff height would occur on a time scale approximately equal to τ_δ. A sample time trace of h illustrating this long-time behavior is presented in Fig. 4.5. (Only 1/256 of the entire data record is plotted.) The experimental conditions are the same as those of Fig. 4.1. For reference, $10\,\tau_\delta = 46.7\,$ms is marked on the figure. The observed fluctuations clearly occur on times much greater than τ_δ. Although small fluctuations occur on the jet time scale, larger fluctuations occur on longer time scales. Another observation is that no periodic behavior is present in the h *vs.* t signal.

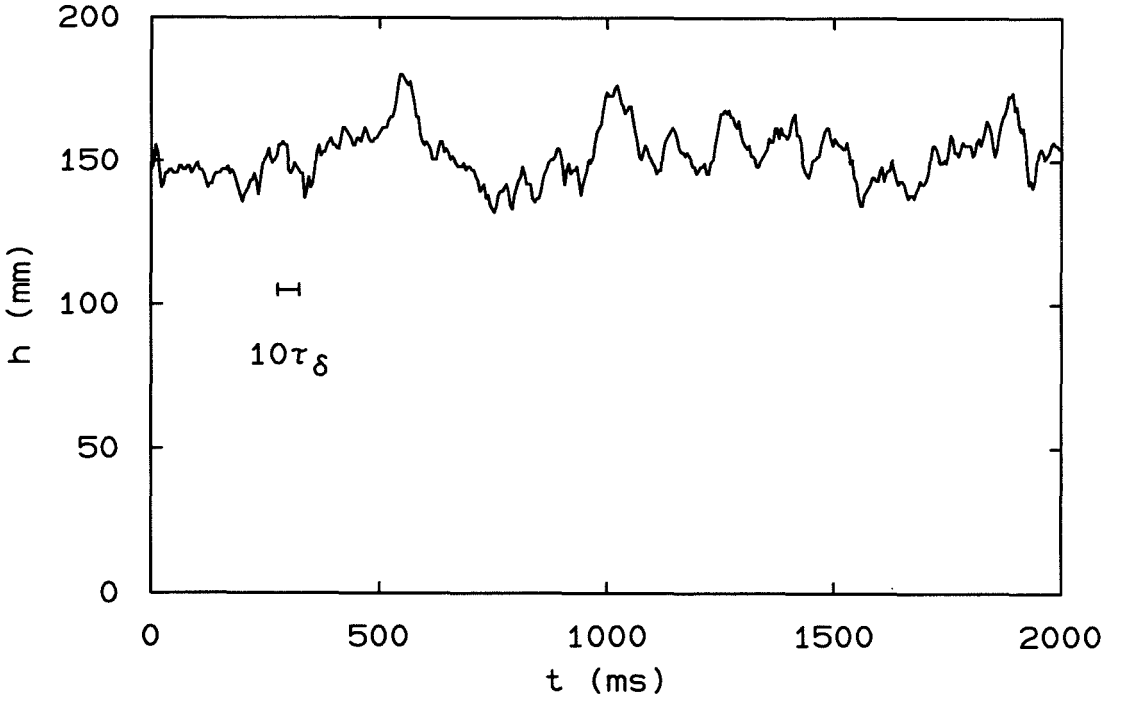

FIG. 4.5 Liftoff height h *vs.* time. C_2H_6, $d = 3.88$ mm, $U_s = 88$ m/s, $\bar{h} = 151$ mm.

To quantify the time scale and frequency content of the fluctuations, the power spectrum of the h *vs.* t signal was computed with program PSD, developed by Prof.

Paul Dimotakis. Then, all the computed points within each third of an octave were averaged to produce a smooth curve for plotting. The spectral power $E_h(f)$ is normalized such that

$$h'^2 = 2\int_0^\infty E_h(f)\,\mathrm{d}f\ . \tag{4.2}$$

The spectrum from the data used in Fig. 4.5 is plotted in Fig. 4.6, where the frequency f has been normalized using τ_δ. At low frequencies the spectrum is flat; at a break frequency f_b the spectrum begins its descent at approximately a constant slope, somewhat steeper than -2. There is no peak in the spectrum that would indicate periodic behavior. Corresponding to the long time behavior noted above, the break frequency, obtained from straight line fits to the two linear portions of the spectrum, is much less than $1/\tau_\delta$, approximately $0.01/\tau_\delta$.

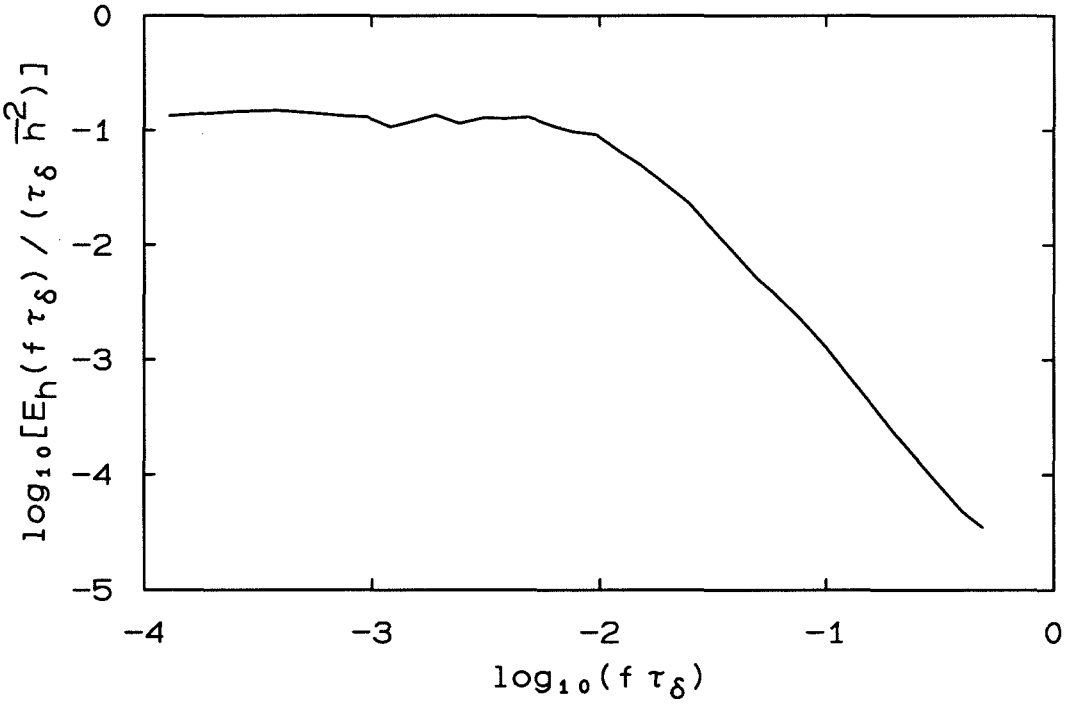

FIG. 4.6 Power spectrum of h. Same conditions as Fig. 4.5.

As a complementary measure of the behavior of $h(t)$, the autocorrelation function was computed using a FFT algorithm (Press *et al.* 1988). This is plotted in Fig. 4.7, where

$$R_{hh}(\tau) \equiv \overline{(h(t)-\bar{h})\,(h(t+\tau)-\bar{h})} \tag{4.3}$$

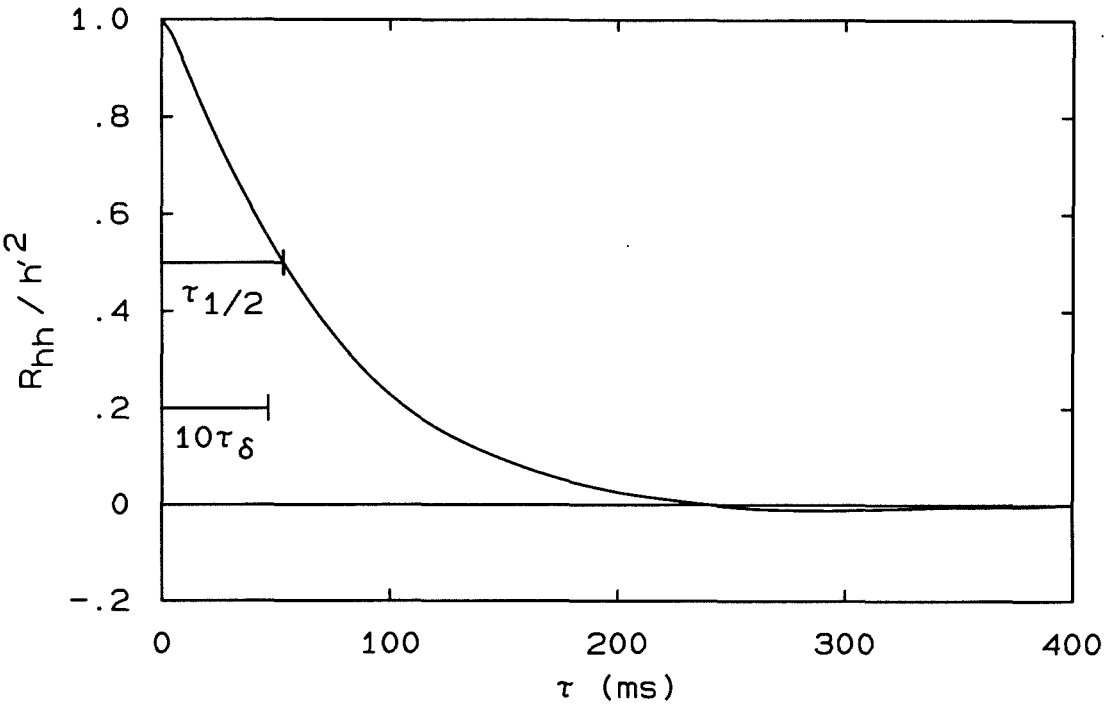

FIG. 4.7 Autocorrelation of h. Same conditions as Fig. 4.5

has been normalized by the mean square level to force the curve to go to one at zero lag time τ. Again, $10\,\tau_\delta$ has been marked on the figure, illustrating that fluctuation times are much larger than τ_δ. The autocorrelation shows no significant undershoot of zero or second peak, indicating that periodic behavior of $h(t)$ is not present. Also marked on the figure is $\tau_{1/2}$, which is defined as the time lag τ for which the autocorrelation function falls to a value of 0.5. (Values of $\tau_{1/2}$ have been corrected for the effect of non-instantaneous sampling time as described in Appendix C.) This time is used throughout this thesis as a representative time of the fluctuations for a given condition. Later in this chapter the measured values of $\tau_{1/2}$ for different experimental conditions are compared.

4.3 Variation of the Fluctuation Time with Conditions

This section examines the dependence of the fluctuation time on the flow conditions. The measurement of h *vs.* t reported in Sec. 4.2 indicates that the correlation time is much larger than the local jet time τ_δ, at least for one experimental condition. Whether this behavior is found in all flow conditions is the topic of this section. Of particular interest is whether $\tau_{1/2}$ is proportional to τ_δ for all flow conditions. By changing the fuel type, nozzle diameter, and liftoff height (by changing the exit velocity), τ_δ can be varied and the resulting correlation time measured. As the experimental conditions are changed, several non-dimensional parameters change which could potentially alter the fluctuation time.

First is the non-dimensional mean liftoff height $\tilde{h}$, defined as $C_Y\,(Y_{\rm st}/Y_{\rm cl})$, as described in Sec. A.4. For most of the conditions to be described,

$$\tilde{h} \;\approx\; Y_{\rm st}\bar{h}/d_{\rm s}\ , \tag{4.4}$$

which is the normalization of $\bar{h}$ used in Ch. 3. With the above definition, there is a one-to-one correspondence between $\tilde{h}$ and $\eta_{\rm st}$, the value of η at which $\bar{Y} = Y_{\rm st}$. At low liftoff heights, $\eta_{\rm st}$ is large and burning takes place close to the outside of the jet. The dynamics of such a flame can be quite different from one with a large liftoff height close to blowout, in which $\eta_{\rm st}$ is small. In the experiments to be discussed in this section, several fuels were used, having different values of $Y_{\rm st}$. To the extent that reaction rates of these fuels are highest at $Y = Y_{\rm st}$ and fall off rapidly for higher or lower values of Y, $\tilde{h}$ is the correct non-dimensionalization of the liftoff height. However, some of the fuels have wider flammability limits than others, and somewhat different dependencies of reaction rate on $Y/Y_{\rm st}$. Therefore, $\tilde{h}$ is not a perfect parameter to use as a non-dimensional liftoff height when different fuels are compared, but it is a reasonable choice.

Another parameter of interest is the Reynolds number. The Reynolds number in the non-reacting part of the jet, just below the liftoff height, Re_h, is estimated as described in Sec. A.5. For most of the conditions studied, Re_h is nearly equal

to the far-field Reynolds number $Re_\infty \equiv U_s d_s/\nu_\infty$. The exception to this is for the 86% H_2 / 14% C_2H_6 flames (to be discussed in Sec. 4.3.5), for which Re_h is $\sim$ 10% to 20% lower than Re_∞ for the range of $\tilde{h}$ studied.

In the burning region of the flame, the effective Reynolds number differs significantly from Re_h because of the temperature rise which lowers the density and increases the viscosity. An approximate measure of this effect can be obtained from a simple one-dimensional analysis of the flame. The momentum flux J will be unchanged in the initial burning region. $J \sim \rho U_{cl}^2 \delta^2$, and the Reynolds number $Re \sim (\rho U_{cl}\delta)/\mu$. Therefore $Re \sim J^{1/2}\rho^{1/2}/\mu$. Noting that $\rho \sim T^{-1}$, and taking as an approximation $\mu \sim T^{.8}$ results in $Re \sim T^{-1.3}$. An appropriate average value of T can be assumed to be $T_\infty + 0.6\Delta T_f$, (see Sec. A.6, which utilizes measurements of Becker and Yamazaki (1978)) where ΔT_f is the adiabatic flame temperature rise of the fuel, $\sim$ 1,900 K for most hydrocarbons. This implies that the effective Reynolds number in the flame will be $\sim$ $0.13\,Re_\infty$. As many approximations were made in this analysis, including the 1-D assumption, the factor of 0.13 is only approximate.

Additionally, buoyancy may affect the dynamics of lifted flames. The relative importance of buoyancy to momentum is characterized by a Richardson number relevant to the dynamics of the flame base (Ri_h), which is the ratio of a buoyancy force to momentum flux. The flow entering the flame base has a momentum flux approximately equal to the source momentum flux, $J_o = (\pi/4)d_s^2 U_s^2$. There is some subjectivity in determining the proper region over which to measure the buoyancy force B. The flow field dynamics are influenced by the region of the flame some distance downstream of the flame base. It was decided to use the region from the liftoff height to one local jet width $\delta(\bar{h})$ downstream.

The details of the definition and calculation method of Ri_h are given in Sec. A.6, and the resulting definition of $\xi_h \equiv Ri_h^{1/3}$ is

$$\xi_h \equiv C_\xi \left(\frac{\overline{\Delta\rho}\, g\, \bar{h}^3}{\rho_\infty U_s^2\, d_s^2} \right)^{1/3} , \tag{4.5}$$

where C_ξ is a constant equal to 0.87 that accounts for the fact that it is the frustrated cone above $\bar{h}$ that provides the buoyancy force, rather than the entire jet cone. $\overline{\Delta\rho}$ is the average value of $\rho_\infty - \rho$ in the region extending from h to $h + \delta$. ξ_h has a length scale $\bar{h}$ to the first power. It is similar to the definition of Becker and Yamazaki (1978) and Becker and Liang (1978), but with $\bar{h}$ as the relevant length scale, rather than the flame length L, and with consideration given to the actual density in the flame.

In addition to the parameters of non-dimensional liftoff height, Reynolds number, and Richardson number, other, more subtle parameters that could affect the dynamics of the liftoff height result from the different chemistry of the fuels. The flammability limits are wider for some of the fuels than the others. Also, the flame temperature rise is not exactly the same for the fuels. Although this variation of ΔT_f has little effect on buoyancy, and has been accounted for in the definition of ξ_h, the resulting dilatation of the gas could conceivably change the nature of the flow at the flame base. Also, the radiative properties of the fuels differ markedly, depending largely on the amount of soot which is produced in the flame.

4.3.1 Effects of Liftoff Height and Fuel Type

The fuels used in the current experiments are listed in Table 3.3, along with their properties relevant to these experiments. They are listed in order of increasing reaction rate or decreasing effective chemical time $\tau_{lo} = \bar{h}/Y_{st}\,U_s$. The first experiments to be discussed here involved the first four fuels listed. Hydrogen was used only as a mixture with the other fuels in the table, and hence discussion of the experiments involving hydrogen is postponed until Sec. 4.3.5.

This section addresses the effects that stabilization distance and fuel type have on the temporal behavior of the flames. The effects of Reynolds number are addressed in Sec. 4.3.2, followed by a discussion of the effects of buoyancy, as characterized by the Richardson number, in Secs. 4.3.3 and 4.3.4. As will be shown,

there is a close correspondence between the fuel type and the resulting Richardson number at the flame base.

From the measured values of $\tau_{1/2}$ at the conditions listed in Table 4.1 (group A nozzles) and Table 4.2 (group B nozzles), an interpolation procedure like that used to prepare Fig. 4.4 in Sec. 4.1 was used. For each fuel and each nozzle, values of $\tau_{1/2}/\tau_\delta$ were interpolated to four values of $\tilde{h}$, 1.5, 1.8, 2.2, and 2.45. To produce a graph in which the Reynolds number is fixed ($Re_h = 22{,}000$), interpolation from the group A and B nozzles was then done at each value of $\tilde{h}$.

The values of $\tau_{1/2}$ normalized by τ_δ are plotted in Fig. 4.8 for each of the four fuels. Because the maximum value of $\tilde{h}$ achieved for C_2H_2 with its group B nozzle was 1.8, only the two points corresponding to $\tilde{h}$ of 1.5 and 1.8 are plotted for that fuel.

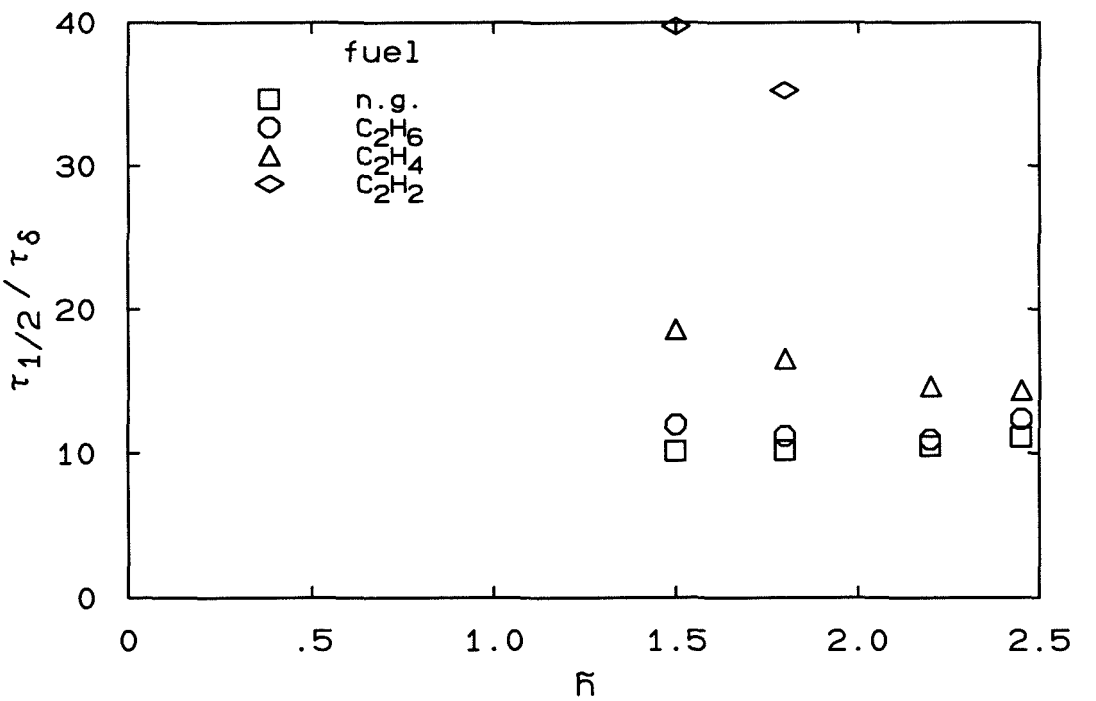

FIG. 4.8 Variation of normalized correlation time $\tau_{1/2}/\tau_\delta$ with normalized liftoff height $\tilde{h}$, at a fixed Reynolds number of $Re_h = 22{,}000$.

All of the fuels have correlation times much larger than the local large-scale time, with normalized correlation times $\tau_{1/2}/\tau_\delta$ ranging from $\sim$ 10 to 40. The

normalized correlation times increase with fuel type in the same order as Table 3.3, which corresponds to decreasing η_o. The effect is most dramatic for C_2H_2, which has values of $\tau_{1/2}/\tau_\delta$ more than twice those of the other fuels. Even C_2H_4, however, begins to show an increase in $\tau_{1/2}/\tau_\delta$ over the values of natural gas and C_2H_6. The possibility that the changing Richardson number at the flame base with fuel type is the cause of the variation of correlation times is examined in Secs. 4.3.3 and 4.3.4.

The other feature of the fluctuations evident from Fig. 4.8 is the variation of correlation time with $\tilde{h}$. For natural gas, there is very little change in $\tau_{1/2}/\tau_\delta$ with $\tilde{h}$. C_2H_6 shows a concave behavior, where $\tau_{1/2}/\tau_\delta$ first decreases then increases as blowout is approached. For C_2H_4 and C_2H_2, there is a decrease in $\tau_{1/2}/\tau_\delta$ with liftoff height, although only the lowest two values of $\tilde{h}$ are available for C_2H_2.

4.3.2 Effect of Reynolds Number

Figure Fig. 4.9 shows the effect of Reynolds number on the flames. Here, $\tau_{1/2}/\tau_\delta$ is plotted against Re_h in four separate plots, with one plot for each of the values of $\tilde{h}$, 1.5, 1.8, 2.2, and 2.45. In each of the four plots, results from each of the four fuels are presented.

In addition to the group A and B conditions, some additional measurements were made at still higher Reynolds numbers, corresponding to the conditions listed in Table 4.3; these points are included in Fig. 4.9. For natural gas and C_2H_6, data were taken only with the group A and B nozzles. For C_2H_4 an additional nozzle (group C) was used for $\tilde{h} = 1.5$, 1.8, and 2.2. For C_2H_2, all three nozzles were used for $\tilde{h} = 1.5$, the group A and B nozzles for $\tilde{h} = 1.8$, and only the group A nozzle for $\tilde{h} = 2.2$ and 2.45.

In general, there is very little variation of normalized correlation time with Reynolds number for all the fuels except C_2H_2. For C_2H_2, at least at $\tilde{h} \leq 1.8$, there is a decrease in $\tau_{1/2}/\tau_\delta$ with Re_h for the range of Re_h shown. It is not obvious why one fuel should exhibit a dependence on Reynolds number while the others

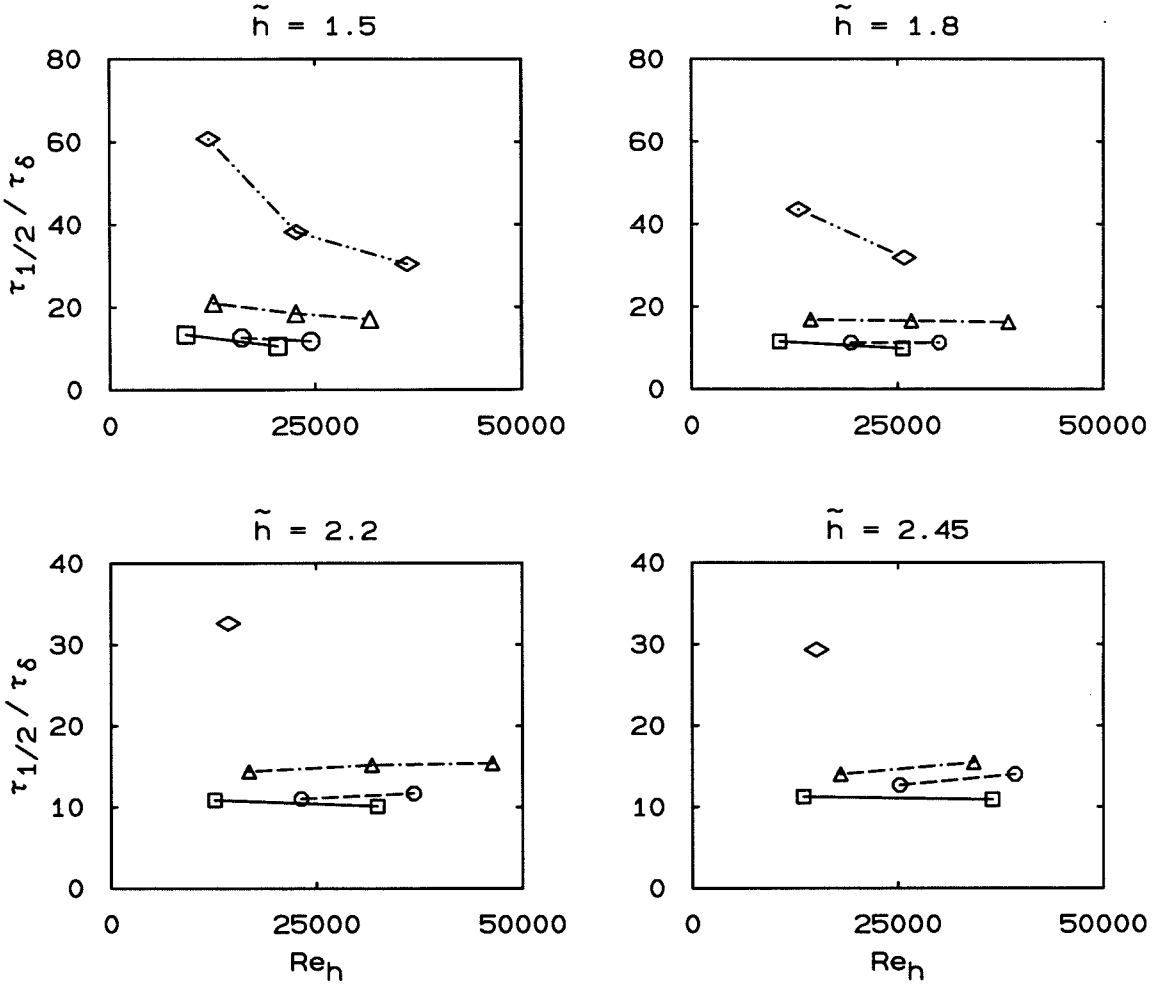

FIG. 4.9 Variation of $\tau_{1/2}/\tau_\delta$ with Re_h and fuel type at four values of $\tilde{h}$ = 1.5, 1.8, 2.2, and 2.45. See Fig. 4.8 for definitions of symbols. Note the different vertical axes of the top and bottom plots.

Table 4.3: Flow Conditions Studied, Group C Nozzles

fuel	d (mm)	U_s (m/s)	$\bar{h}$ (mm)	Re_h	$\tau_{1/2}$ (ms)
C_2H_4	3.88	115	87	30,400	21.2
		148	108	38,300	23.9
		179	130	45,800	27.7
C_2H_2	2.16	186	32	28,000	8.3
		245	43	35,400	8.4

do not. One possibility is that C_2H_2, which has a higher flame temperature than

the other fuels (Table 3.3), has a lower effective Reynolds number at a given value of the cold-jet Reynolds number Re_h. Then, while the range of flame Reynolds numbers is high enough for Reynolds number independence in the other fuels, it is low enough to still have a dependence for C_2H_2. It would be somewhat surprising, however, if the Reynolds number in the burning region were more important than that upstream of the flame base (Re_h) in determining the dynamics of the flame base.

4.3.3 Variation of Correlation Time with Richardson Number

The correlation times of different fuels can be compared by calculating the value of ξ_h, and plotting the corresponding value of $\tau_{1/2}/\tau_\delta$. Faster fuels, with smaller effective chemical times, $\tau_{lo} = \bar{h}/Y_{st}U_s$, will have lower Richardson numbers. This can be seen by combining the definition of τ_{lo} with the definition of the Richardson number (Eq. 4.5) to get

$$\xi_h = C_{\xi,s} \left(\frac{Y_{st}\,\bar{h}}{d_s}\right)^{1/2} \left(\frac{g'^2\,\tau_{lo}^3}{U_s\,d_s}\right)^{1/6} . \tag{4.6}$$

Here, $C_{\xi,s}$ is a constant, and $g' \equiv g\,\overline{\Delta\rho}/\rho_\infty$ is approximately constant for the various fuels. Then, if $\tilde{h} \approx Y_{st}\bar{h}/d_s$ is fixed, and the Reynolds number is fixed by keeping $U_s d_s$ constant, ξ_h will be proportional to $\tau_{lo}^{1/2}$.

Figure 4.10 shows the results of all three groups of nozzles, A, B, and C. For each fuel/nozzle pair, four points are plotted, corresponding to the four values of $\tilde{h}$. Beside each group of points, the corresponding fuel is printed. For the group A conditions (open symbols), there are data points at each of the four values of $\tilde{h}$ for each of the four fuels. For the group B conditions (filled symbols), there are four data points for each fuel except C_2H_2 for which only the lower two values of $\tilde{h}$ are plotted. The four points from the group C nozzles (one for C_2H_2 and three for C_2H_4) are plotted with a + inside the symbol. These points make the graph somewhat cluttered for C_2H_4 where the points lie close to those for the group B nozzles.

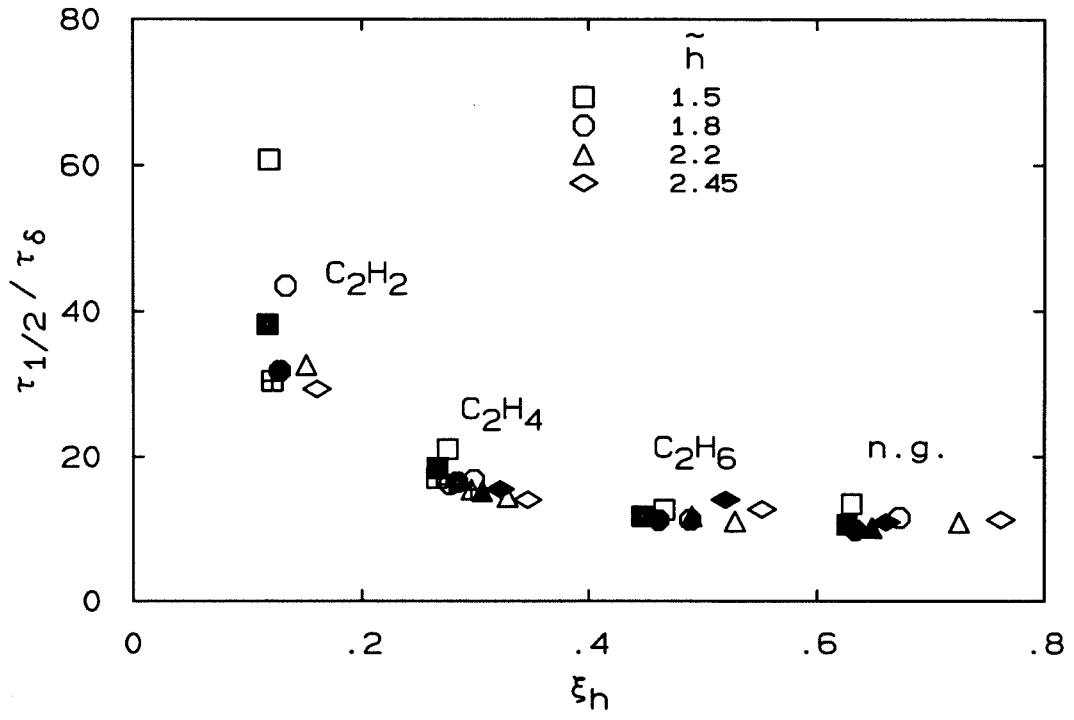

FIG. 4.10 Variation of normalized correlation time $\tau_{1/2}/\tau_\delta$ with Richardson number ξ_h, for the conditions listed in Tables 4.1, 4.2, and 4.3. Open symbols: group A, filled symbols: group B, symbols with a + inside: group C.

There is a reasonably good collapse of correlation time with Richardson number. Because the values of ξ_h do not overlap for the different fuels, however, the results are not as robust as they would otherwise be. Also, the acetylene results for the two different nozzle diameters do not collapse very well. It could be argued, however, that the imperfect collapse for C_2H_2 is due to slight errors on the estimation of ξ_h for the different nozzles. Alternatively, this may be a Reynolds number effect, as discussed previously.

The variation of the correlation time with ξ_h is quite extreme for the C_2H_2 flames while for the other fuels, $\tau_{1/2}$ approximately scales with τ_δ (although the upward trend is apparent for C_2H_4). It is surprising that at such low Richardson numbers as the C_2H_2 flames have, there would be such a large effect of further reduction in ξ_h. Although extrapolating the curve to $\xi_h \rightarrow 0$ appears to show $\tau_{1/2}/\tau_\delta \rightarrow \infty$, it is reasonable to expect that that $\tau_{1/2}/\tau_\delta$ would actually go to some constant value as $\xi_h \rightarrow 0$. The Richardson numbers of all the flames studied

are relatively low by conventional standards. Becker and Yamazaki (1978) found that for $\xi_x < 1$, the mass flux and momentum flux are relatively independent of ξ_x in hydrocarbon flames. Because they used the approximation $\overline{\Delta\rho} \approx \rho_\infty$ in their definition of ξ, a more appropriate value to use in comparing with the current definition of ξ_h, which assumes $\overline{\Delta\rho} \approx \rho_\infty - \rho(T_\infty + 0.6\,\Delta T_f)$ would be ~ 0.93. Similarly, Gilbrech (1991) found Richardson number independence of flame length of low-temperature flames for $\xi_x < 1$. In his definition of ξ, $\overline{\Delta\rho} \approx \rho_\infty - \rho(T_\infty + \Delta T_f)$, and so a more appropriate value to use in comparing with the current definition would be $0.6^{1/3} = 0.84$. Because the Richardson numbers in the current experiments are below that in which momentum dominance is believed to hold, the dependence of $\tau_{1/2}/\tau_\delta$ on ξ_h is surprising. However, because the dynamics of the flames are largely affected by the outer part of the jet, where velocities are lower, such a dependence on ξ_h is conceivable.

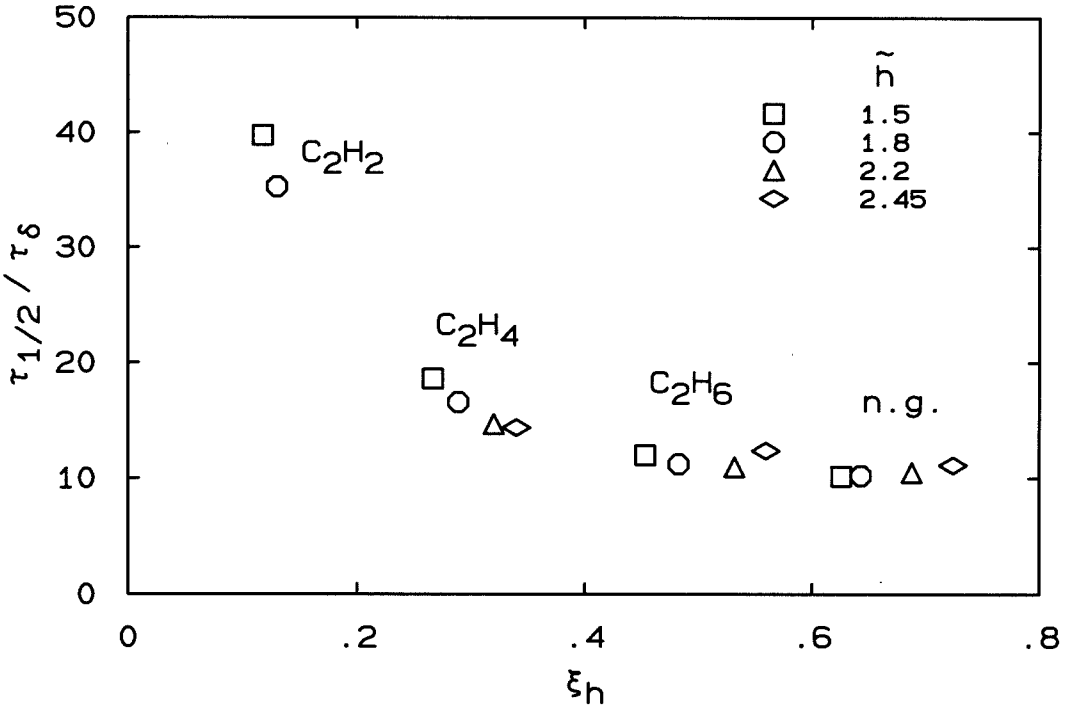

FIG. 4.11 Variation of normalized correlation time $\tau_{1/2}/\tau_\delta$ with Richardson number ξ_h, at a fixed Reynolds number of $Re_h = 22{,}000$.

One possible reason for acetylene's longer normalized correlation times is that

its radiation, which is considerably greater than that of the other fuels because of greater soot production, might somehow affect the dynamics of the liftoff height. This possibility is discussed in Sec. 4.5.

As indicated in Fig. 4.9, there is some variation of $\tau_{1/2}$ with Reynolds number, in particular for C_2H_2. In Fig. 4.10, however, the different points are not at the same Reynolds number, making it somewhat difficult to distinguish the effects of ξ_h from those of Re_h. Figure Fig. 4.11 shows the data after interpolating to $Re_h = 22{,}000$, as was done in Fig. 4.8.

The data fall nearly onto a single curve. There is a slight variation with $\tilde{h}$, however. As mentioned above, it is conceivable that the non-dimensional liftoff height would have an effect on the flame dynamics, resulting in separate curves of $\tau_{1/2}/\tau_\delta$ *vs.* ξ_h for the different values of $\tilde{h}$. The variation of $\tau_{1/2}/\tau_\delta$ with $\tilde{h}$ is not very large for the fuels other than acetylene, however.

4.3.4 Effect of Nozzle Orientation

To help discern whether buoyancy is responsible for the variation of correlation time with fuel type, measurements of h *vs.* t were repeated with the nozzles oriented horizontally. If buoyancy is an important parameter, then having the buoyancy force normal to the flame propagation direction would be expected to alter the liftoff height dynamics, although it would not have the same effect as eliminating buoyancy altogether.

The flow conditions for the horizontal-flame experiments are listed in Table 4.4. The same conditions were studied as for the (vertical) nozzles in group A, except that C_2H_6 was not used. Also, slightly higher velocities were needed for natural gas and C_2H_4 to achieve the same liftoff heights, as shown by the plot of $\bar{h}$ *vs.* U_s (Fig. 4.12). This is understandable in that, in the horizontal flames, there is no force pushing the hot products downstream and inhibiting the ignition of fresh reactants as there is with the vertical flames. This variation with nozzle orientation would be

Table 4.4: Flow Conditions Studied, Horizontal Nozzles					
fuel	d (mm)	U_s (m/s)	$\bar{h}$ (mm)	Re_h	$\tau_{1/2}$ (ms)
n.g.	4.61	39	92	9,200	52.7
		46	108	10,800	58.2
		57	133	13,200	74.7
		63	149	14,500	81.1
C_2H_4	2.16	86	49	12,600	21.5
		103	60	14,900	25.7
		124	76	17,600	28.6
		136	87	19,100	33.6
C_2H_2	1.02	176	20	11,900	10.9
		197	25	13,100	10.8
		220	30	14,400	10.7
		235	34	15,200	11.5

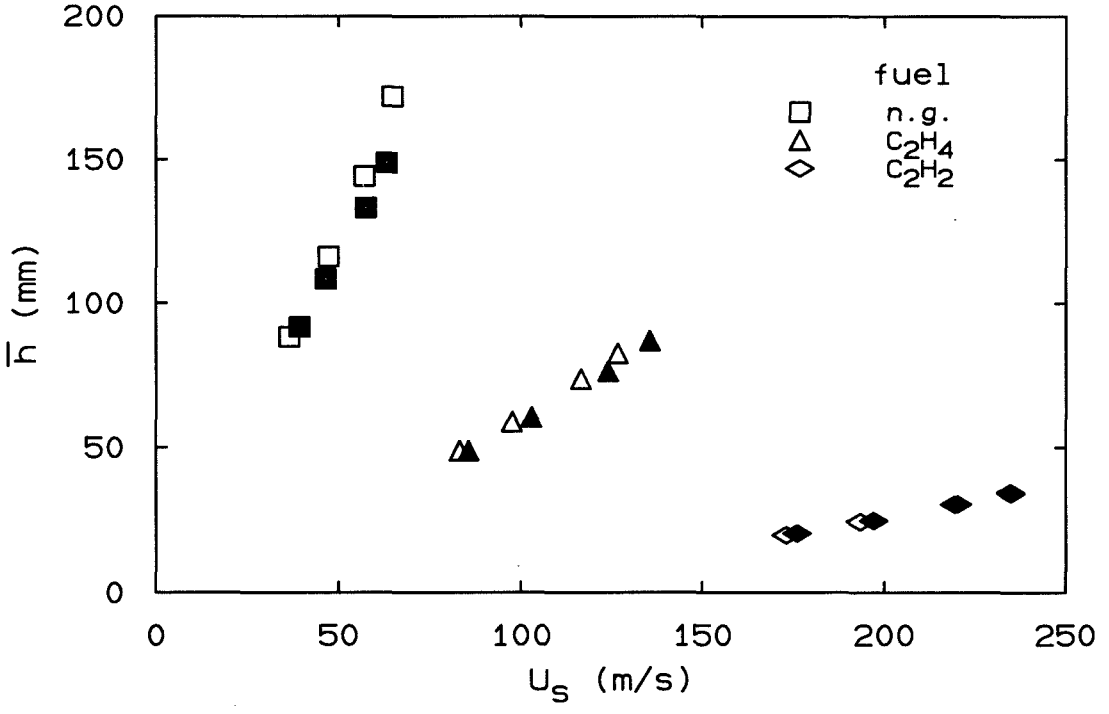

FIG. 4.12 Effect of nozzle orientation on mean liftoff heights. Open symbols: vertical nozzles, filled symbols: horizontal nozzles.

most extreme for the more buoyant flames. However, even for natural gas, which has the largest Richardson numbers, the velocities are only $\sim$ 15% larger for the horizontal nozzles.

The correlation times are plotted in Fig. 4.13 for the horizontal and vertical nozzles. Within the resolution of the measurements, there is no change in the dynamics of the liftoff height with nozzle orientation. This is true for all three of the fuels studied. The largest effect would be expected for natural gas flames, since the Richardson number is the highest for them, but neither they nor the other flames appear to be affected by the nozzle orientation.

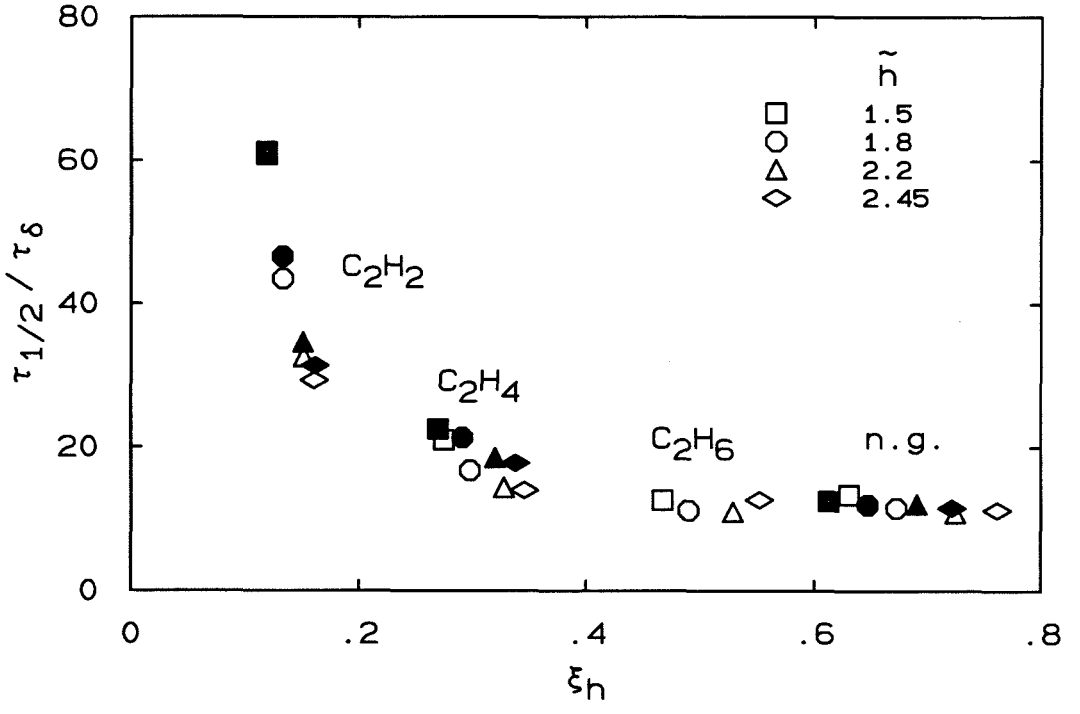

FIG. 4.13 Effect of nozzle orientation on scaled correlation time $\tau_{1/2}/\tau_\delta$ *vs.* Richardson number ξ_h. Open symbols: vertical nozzles, filled symbols: horizontal nozzles.

The result that the direction of the gravitational vector relative to the nozzle orientation has no measurable affect on the liftoff height dynamics makes the collapse of $\tau_{1/2}/\tau_\delta$ with ξ_h, a measure of the importance of buoyancy, more difficult to explain. It is still possible that both horizontal and vertical nozzles could have

comparable effects of buoyant behavior on the liftoff height dynamics. Other explanations for the variation of $\tau_{1/2}/\tau_\delta$ with ξ_h are examined in the following sections.

4.3.5 Results for Fuel Mixtures

To gain additional control of the flow conditions, experiments were conducted using mixtures of fuels. By appropriately choosing the proportions of the fuels, the effective chemical time of the fuel mixture could be controlled. The conditions studied are listed in Table 4.5. A mixture of 50% C_2H_2 / 50% C_2H_6 (by volume) was used primarily to compare with C_2H_4. Mixtures or H_2 with each of C_2H_6, C_2H_4, and C_2H_2 were used to obtain effective chemical times in the neighborhood of that of C_2H_2.

Only one nozzle diameter was used for the C_2H_2/C_2H_6 mixture, the same nozzle as was used for C_2H_4 in the group A conditions. For the H_2/C_2H_6 mixture, three different nozzle diameters were used to be able to interpolate to $Re_h = 22{,}000$ at each of the four non-dimensional liftoff heights. Two nozzles were used for the H_2/C_2H_4 experiments, again allowing interpolation to $Re_h = 22{,}000$. Only a single nozzle diameter was used for the H_2/C_2H_2 mixture.

To test whether the collapse of $\tau_{1/2}/\tau_\delta$ *vs.* ξ_h would hold for fuels other than the four fuels previously reported, the mixture of 50% C_2H_2 / 50% C_2H_6 was used. This resulted in the same average molecular weight and Y_{st} as C_2H_4. The measurements of $\bar{h}$ revealed that the mixture's effective chemical time is slightly lower than that of C_2H_4, yielding slightly lower liftoff heights at each exit velocity.

Measurements of the correlation times for the C_2H_2/C_2H_6 mixture are shown in Fig. 4.14 along with the group A results and the H_2/C_2H_2 results. The groups of points corresponding to each fuel (or mixture) are labeled, and the symbols alternate between filled and open in the order of ξ_h. The 50% C_2H_2 / 50% C_2H_6 and C_2H_4 results nearly lie on top of each other, although the former have slightly lower values of ξ_h at each value of $\tilde{h}$. The fact that the 50% C_2H_2 / 50% C_2H_6

Table 4.5: Flow Conditions Studied, Fuel Mixtures					
fuel	d (mm)	U_s (m/s)	$\bar{h}$ (mm)	Re_h	$\tau_{1/2}$ (ms)
50% C_2H_2/ 50% C_2H_6	2.16	89	50	13,300	19.3
		104	60	15,300	19.4
		122	72	17,600	21.1
		136	85	19,500	26.3
86% H_2/ 14% C_2H_6	1.55	357	42	14,600	10.9
		393	46	16,200	10.8
	2.16	264	36	15,200	12.9
		320	43	18,100	11.5
		375	51	21,300	11.0
		442	62	25,300	11.3
	3.12	438	59	36,000	10.3
		509	68	42,100	11.1
50% H_2/ 50% C_2H_4	2.16	153	44	15,600	16.9
		172	51	17,400	16.6
		201	63	20,300	16.9
		225	75	22,600	21.8
	3.12	189	59	28,000	15.5
		248	76	36,400	17.2
		295	92	42,900	19.7
		311	102	45,200	21.4
50% H_2/ 50% C_2H_2	1.02	290	21	13,300	8.5
		265	17	12,300	9.6
		346	29	15,600	8.1

points fall on the same curve as the pure fuels provides support that ξ_h can collapse results of different fuels. It should be noted, however, that this is not a particularly strong test of the collapse with ξ_h because the mixture of 50% C_2H_2 / 50% C_2H_6 has the same average chemical composition, molecular weight, and Y_{st} as C_2H_4. Discussion of the H_2/C_2H_2 mixture results (left-most points) is postponed until all other mixture results have been described.

Other fuel mixtures were used to achieve Richardson numbers near to those of

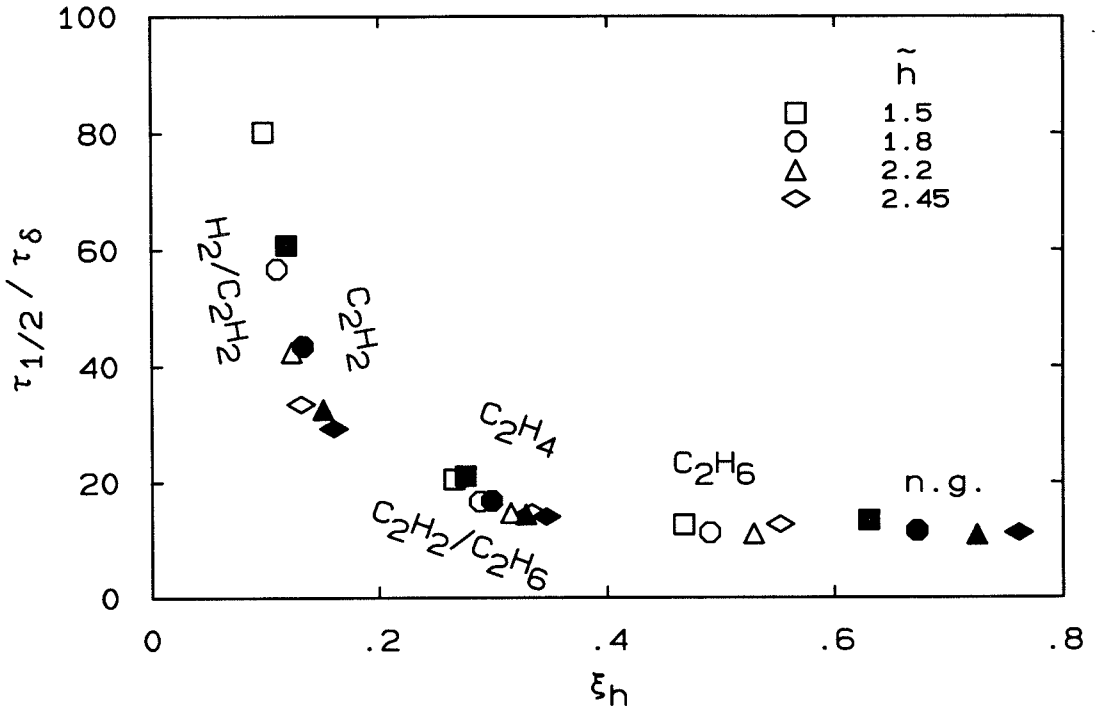

FIG. 4.14 Variation of normalized correlation time $\tau_{1/2}/\tau_\delta$ with Richardson number ξ_h, for the conditions listed in Table 4.1 and for the 50% C_2H_2 / 50% C_2H_6 and 50% H_2 / 50% C_2H_2 mixtures listed in Table 4.5. Filled symbols: n.g., C_2H_4, and C_2H_2.

acetylene flames. This was done largely to see whether the longer non-dimensional correlation times encountered with C_2H_2 were peculiar to that fuel. Experiments previously conducted, and described in Sec. 4.5, showed that the visible radiation from C_2H_2 flames is highly correlated with fluctuations in h. It was thought that some feedback mechanism from the flame radiation (and associated heat loss) to the flame base might be the cause of the longer correlation times. Mixing H_2 with C_2H_6 or C_2H_4 provided a good way to achieve flames with low τ_{lo} and low ξ_h, without intense radiation from soot. Pure hydrogen could not be used because its visible radiation is insufficient for detection with the photodiode array.

First, a mixture of 86% H_2 / 14% C_2H_6 was used. The effective chemical time of the mixture was found to be slightly larger than that of C_2H_2, but sufficiently close for the present purposes. No radiation from soot was observed for these flames. Following these experiments, studies of a mixture of 50% H_2 / 50% C_2H_4 were made.

Very little radiation from soot was observed for these flames. The effective chemical time of this mixture was found to be slightly larger than the 86% H_2 / 14% C_2H_6 mixture. By using more than one nozzle for each of the two mixtures, interpolation to a constant Reynolds number of 22,000 was made possible. Results are shown in Fig. 4.15. This figure is similar to Fig. 4.11, but with additional data points for the mixtures of H_2 with C_2H_6 and C_2H_4. Although neither of the fuel mixtures achieved quite as low a Richardson number as pure C_2H_2, it can still be seen that there is a substantial increase in $\tau_{1/2}/\tau_\delta$ as ξ_h becomes small. The mixture results fall approximately on the same curve as the pure-fuel results, although the 50% H_2 / 50% C_2H_4 points are slightly to the right of the 86% H_2 / 14% C_2H_6 points.

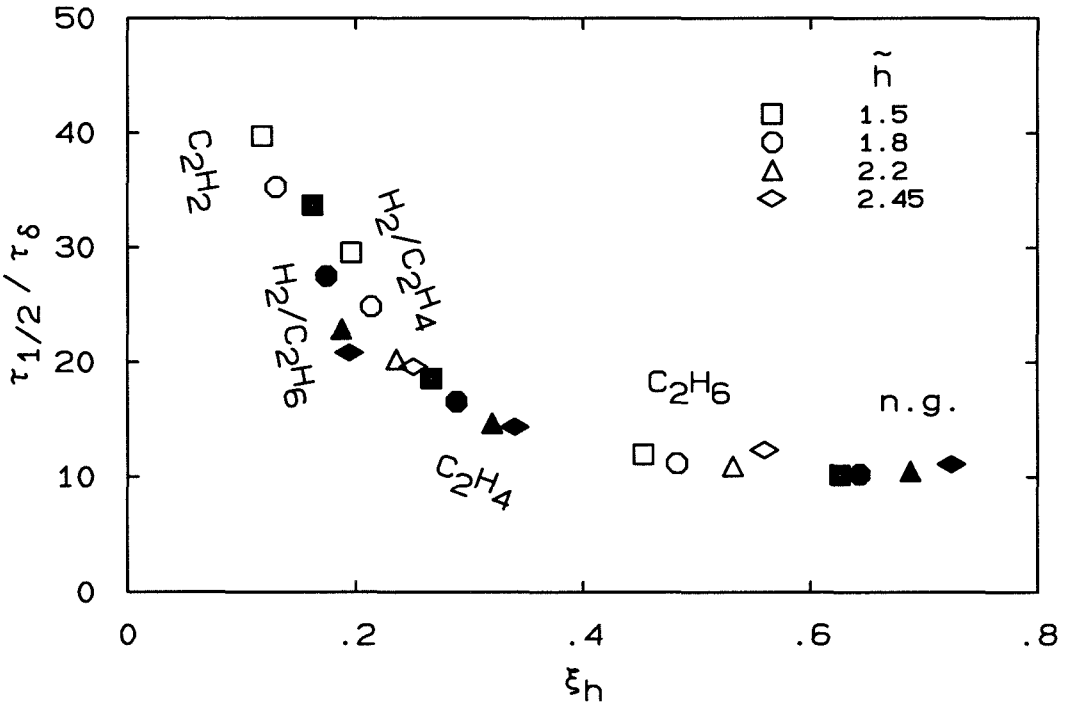

FIG. 4.15 Variation of normalized correlation time $\tau_{1/2}/\tau_\delta$ with Richardson number ξ_h, comparing C_2H_2 flames with mixtures of H_2 with C_2H_6 and C_2H_4. $Re_h = 22{,}000$. Filled symbols: n.g., C_2H_4, 86% H_2 / 14% C_2H_6.

The basic conclusion from Fig. 4.15 is that the large correlation times for C_2H_2 are *not* the result of the intense radiation from such flames. The H_2/C_2H_6 and H_2/C_2H_4 flames, for which little radiation from soot is present, also have large

(normalized) correlation times.

The last fuel mixture in Table 4.5 is 50% H_2 / 50% C_2H_2, which was used to achieve Richardson numbers even lower than for pure C_2H_2. It was not known whether the trend toward higher $\tau_{1/2}/\tau_\delta$ would continue as ξ_h was decreased. The results are plotted in Fig. 4.14, some aspects of which has already been discussed above. The left-most point at each of the four liftoff heights is from the H_2/C_2H_2 mixture. It is evident from Fig. 4.14 that $\tau_{1/2}/\tau_\delta$ continues to increase as ξ_h is decreased beyond the range achievable with C_2H_2. If the curve levels out at low ξ_h, it must occur at lower values than those yet reached in these experiments. It is also worth noting that the Reynolds numbers of the C_2H_2 flames and the 50% H_2 / 50% C_2H_2 flames are comparable, indicating that the difference in $\tau_{1/2}/\tau_\delta$ is not a result of different Reynolds numbers.

4.4 Simultaneous Measurements of Liftoff Height and Flame Length

Fluid mechanical time scales at the flame tip, where the length scales are larger and the velocities are lower, are considerably longer than the time scales at the flame base ($\tau_\delta(\bar{h})$). Because the measured fluctuation times of the liftoff height were found to be considerably larger than $\tau_\delta(\bar{h})$, there was some speculation that the behavior at the flame tip might be influencing the motion of the flame base. To investigate this possibility, measurements of both the liftoff height and flame length were made simultaneously.

The same photodiode array was used for both measurements by positioning the array such that both the flame base and the flame tip were in view. While there is a sharp transition in light intensity at the flame base, the intensity decays much more gradually at the flame tip. This results in some ambiguity in determining the flame length L, but simply setting a threshold in intensity proved to be adequate.

Two flow conditions were studied using natural gas with the 4.61 mm nozzle, and one condition using C_2H_6 with the 3.88 mm nozzle. The relevant parameters are listed in Table 4.6.

Table 4.6: Conditions of h and L Measurements							
fuel	d (mm)	U_s (m/s)	$\bar{h}$ (mm)	h' (mm)	$\tilde{h}$	$\bar{L}$ (mm)	L' (mm)
n.g.	4.61	39	111	6.1	1.80	850	66
		53	153	10.2	2.48	900	64
C_2H_6	3.88	80	153	9.2	2.29	1000	72

Portions of the two time traces for the higher velocity natural gas condition are plotted in Fig. 4.16. The liftoff height values have been multiplied by 4 to allow both h and L to be seen clearly on one plot. In the flame length signal, ramp structures are evident. This is caused by burning structures propagating downstream and burning out. Once the structure burns out, the flame length abruptly drops back to the next-most upstream burning region. This behavior has been observed previously in liquid flames by Dahm and Dimotakis (1987) and in hydrocarbon flames by Mungal *et al.* (1991).

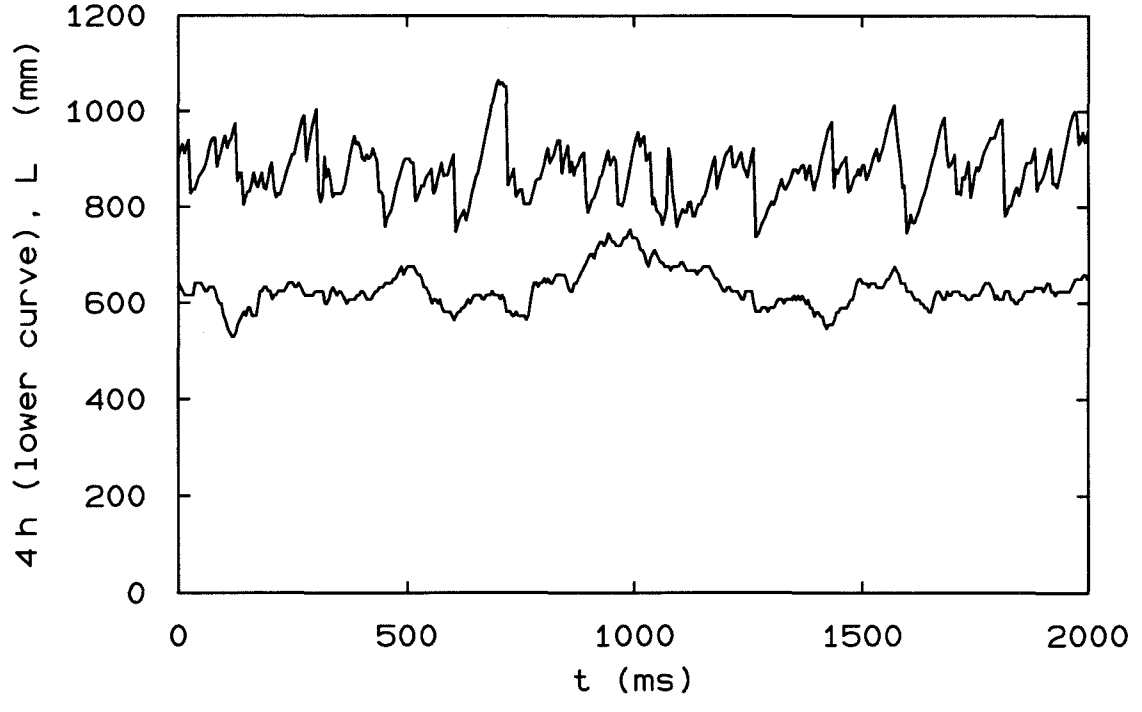

FIG. 4.16 Liftoff height h and flame length L *vs.* time. Natural gas, $d = 4.61$ mm, $U_s = 53$ m/s.

Looking at the time traces, there is evidently very little correlation between the h and L signals. This is supported by Figs. 4.17 and 4.18, which show correlations for the two natural gas cases listed in Table 4.6. In each of those two figures, three curves are plotted. The autocorrelation of h and that of L are shown, along with the cross correlation of h and L, where a positive time lag is defined for L lagging h. The autocorrelation curves have again been normalized by the mean square value, forcing the curves to go through one at zero time lag. The cross correlation has been normalized in a similar manner,

$$\rho_{h\,L}(\tau) = \frac{\overline{(h(t) - \bar{h})\,(L(t+\tau) - \bar{L})}}{(h'\,L')} \quad . \tag{4.7}$$

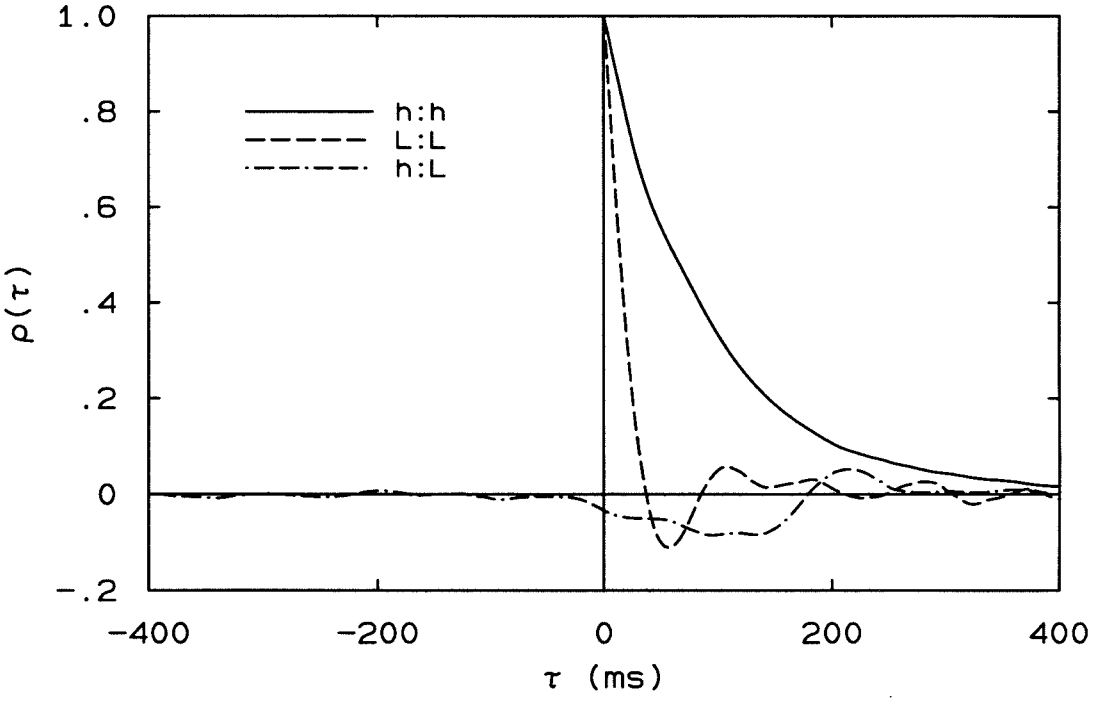

FIG. 4.17 Correlation of liftoff height h and flame length L *vs.* time. Natural gas, $d = 4.61$ mm, $U_s = 39$ m/s.

The flame length autocorrelation shows some periodic behavior, corresponding to the burnout of large structures. For reference, the calculated time scales of the flow for the first case in Table 4.6 are: $\tau_\delta(\bar{h}) = 6.4$ ms, $\tau_\delta(\bar{L}) = 80$ ms, and the

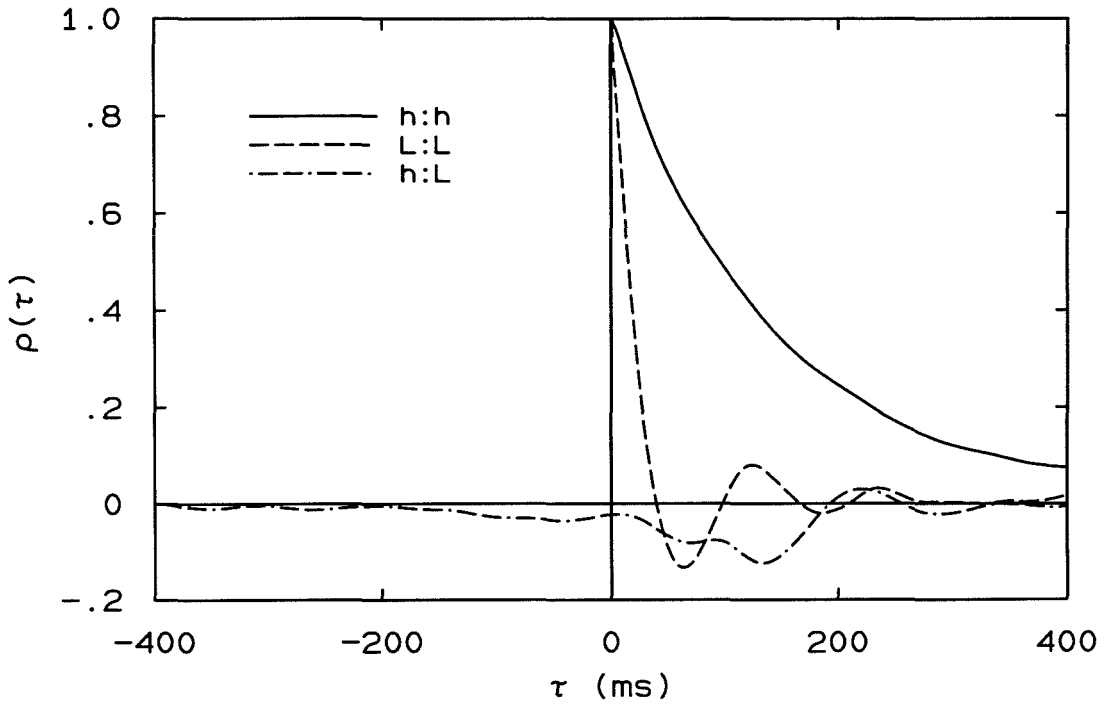

FIG. 4.18 Correlation of liftoff height h and flame length L *vs.* time. Natural gas, $d = 4.61$ mm, $U_s = 53$ m/s.

convection time τ_c from $\bar{h}$ to $\bar{L}$ is approximately 120 ms. For the second case the times are: $\tau_\delta(\bar{h}) = 9.0$ ms, $\tau_\delta(\bar{L}) = 76$ ms, and $\tau_c = 120$ ms. For estimating $\tau_\delta(\bar{L})$ and τ_c, experimental results of Becker and Yamazaki (1978) were used in the velocity estimates in the flame, as described in Sec. A.7. The convection time is defined here as the time for fluid to move from $\bar{h}$ to $\bar{L}$ traveling at the mean centerline velocity. Because there is considerable uncertainty in the estimates of $\tau_\delta(\bar{L})$ and τ_c, they are intended only as an approximate reference time to compare to the correlations. As seen in Figs. 4.17 and 4.18, the time scale of the flame length fluctuations is considerable smaller than that of the liftoff height, even though the large-scale time at the flame tip is considerable larger than at $\bar{h}$. The measurements of the two quantities are somewhat difficult to compare, however, because the flame length shows some periodic behavior and its autocorrelation has such a different shape from that of the liftoff height.

In both flames, there is only a modest correlation between h and L, which is

negative, and peaks at a time in the vicinity of the convection time from $\bar{h}$ to $\bar{L}$. The most important observation, however, is that the two signals are *not* strongly correlated, indicating that the flame tip behavior is not responsible for the observed long correlation times in the liftoff height. This is the result that was expected. Considering that a jet is nearly a parabolic flow, the dynamics far downstream should not significantly influence the upstream regions. Because $L > 4\,h$, feedback from the flame tip to the liftoff height would be expected to be weak.

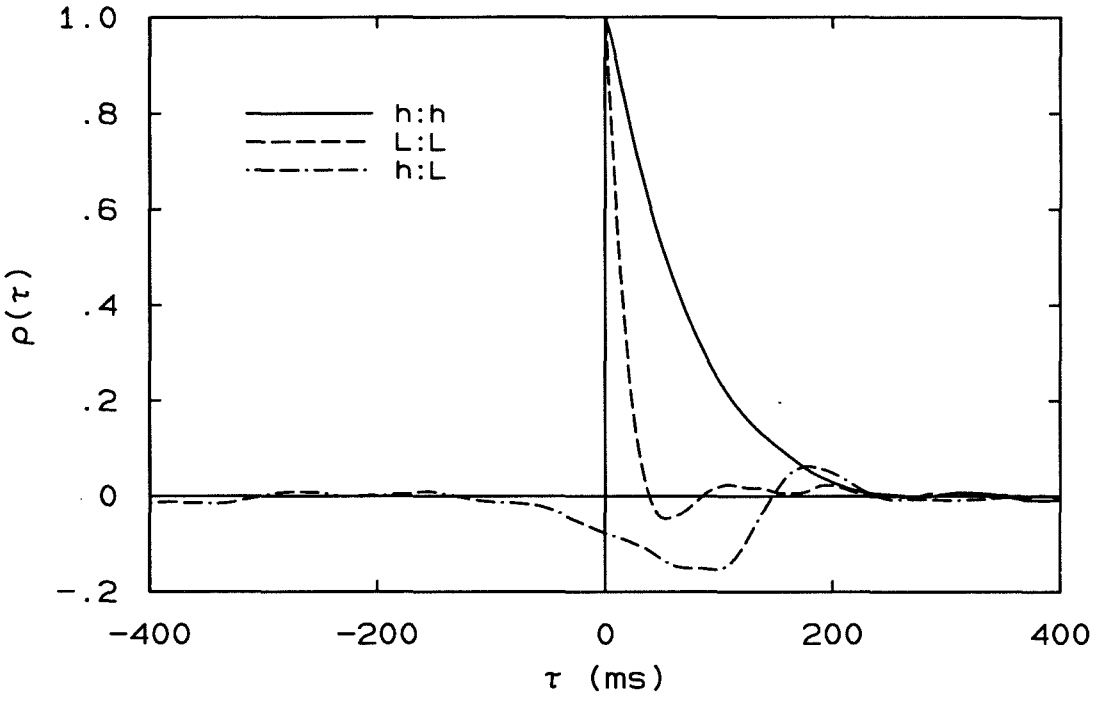

FIG. 4.19 Correlation of liftoff height h and flame length L *vs.* time. C_2H_6, d = 3.88 mm, U_s = 80 m/s.

Results similar to those presented for natural gas were obtained with C_2H_6 using a 3.88 mm nozzle as shown in Fig. 4.19. The results from the slightly higher Reynolds number C_2H_6 flame (Re_h = 20,000 for the C_2H_6 flame *vs.* 12,000 for the second natural gas flame) provide further evidence that the dynamics at the flame tip are not responsible for the behavior of $h(t)$.

4.5 Simultaneous Measurements of Liftoff Height and Radiation

As shown in Figs. 4.10, 4.11, and 4.15, the measured values of $\tau_{1/2}/\tau_\delta$ are well correlated with ξ_h. However, the fact that the correlation times are unchanged by nozzle orientation (Fig. 4.13) suggested that there might be an explanation for the collapse other than the influence of buoyancy.

For the first four fuels listed in Table 3.3, the radiation from soot increases in the same order as τ_{1o}. That is, C_2H_2 radiates more than C_2H_4 which radiates more than either C_2H_6 or natural gas, neither of which produce substantial amounts of soot under the conditions investigated. Furthermore, for a given fuel, *e.g.*, C_2H_2, flames at low non-dimensional liftoff heights have lower Richardson numbers (*cf.* Eq. 4.6 on p. 56), and were also found to have greater radiation from soot. Therefore, for the first four fuels listed in Table 3.3, there is a one-to-one correspondence between the Richardson number of a flame and the fraction of heat radiated away from the flame. It was conjectured that there might be some feedback mechanism whereby the radiation in the downstream portion of the flame, where fluid mechanical time scales are larger than at the liftoff height, could couple with the liftoff height fluctuations and cause the correlation times of $h(t)$ to increase. This would then explain the collapse of $\tau_{1/2}/\tau_\delta$ with ξ_h shown in Fig. 4.11.

The measurements reported in this section were performed prior to those of Sec. 4.3.5 in which mixtures of H_2 with other fuels were used to produce flames with low Richardson numbers comparable to the C_2H_2 flames, but without the radiation from soot. The values of $\tau_{1/2}/\tau_\delta$ found for the mixtures were comparable to those of C_2H_2, making it very unlikely that the large correlation times of C_2H_2 result from the radiation. Nevertheless, some interesting results were obtained on the simultaneous measurement of liftoff height and radiation, which are reported in this section.

It was noticed in visual observations of the C_2H_2 flames that when the flame base dropped to a low position, the radiation generally increased, presumably because of increased soot production. To verify this, simultaneous measurements were

made of the liftoff height and flame radiation at a position downstream of the flame base. The radiation was measured with the same photodiode array used to determine the liftoff height. The photodiode's spectral response to radiation is not flat. It peaks at $\sim$ 700 nm and falls off rapidly outside the visible range. Therefore, the radiation measurement was qualitative, but quite adequate for the purposes of determining the degree to which the flame radiation and liftoff height are correlated.

The acetylene flames which were studied are listed in Table 4.7, where the intensity I is in arbitrary units, but is consistent from one case to the next. The downstream distance at which I was measured is denoted as x_I. By examining traces of intensity all along the flame, it was found that the radiation at different downstream locations fluctuates together. Therefore, the results presented are not very sensitive to the choice of x_I, except possibly the magnitude of the light intensity. For all the flames, the 1.02 mm nozzle was used. For the first three cases listed, a neutral density filter 2.0 (each 0.3 is one stop, or a reduction in light intensity by a factor of 2) was used to reduce the signal below the saturation level of the photodiode array. The fourth case had low enough radiation that no filter was required.

The measurement of I was made at a position along the photodiode array some distance downstream from that of h, typically 200 pixels. Because the measurement of intensity at any given pixel of the array is the integration of light over a time period Δt ending at the measurement time, the measurements of h and I were not exactly simultaneous. The data were corrected for this by assuming that the measurement of I occurred at a time lag from that of h, equal to the time needed to scan from the pixel corresponding to $\bar{h}$ to the pixel at which I was measured. For the acetylene flames this was a significant correction to the data.

Two observations can be made from Table 4.7. First, as the liftoff height increases, the flame radiation decreases, especially near blowout. Second, as the liftoff height increases, the ratio $I'/\bar{I}$ increases. This is because at the high liftoff heights, the flame radiation is highly intermittent, occurring in short, infrequent

Table 4.7: Conditions of h and I Measurements: C_2H_2						
U_s (m/s)	$\bar{h}$ (mm)	h' (mm)	$\tilde{h}$	x_I (mm)	$\bar{I}$ (arb.)	I' (arb.)
166	21.4	0.90	1.56	60	62	11
178	24.9	1.14	1.81	70	56	14
199	31.0	1.65	2.25	80	17	6.7
213	35.7	2.24	2.60	90	0.62	0.52

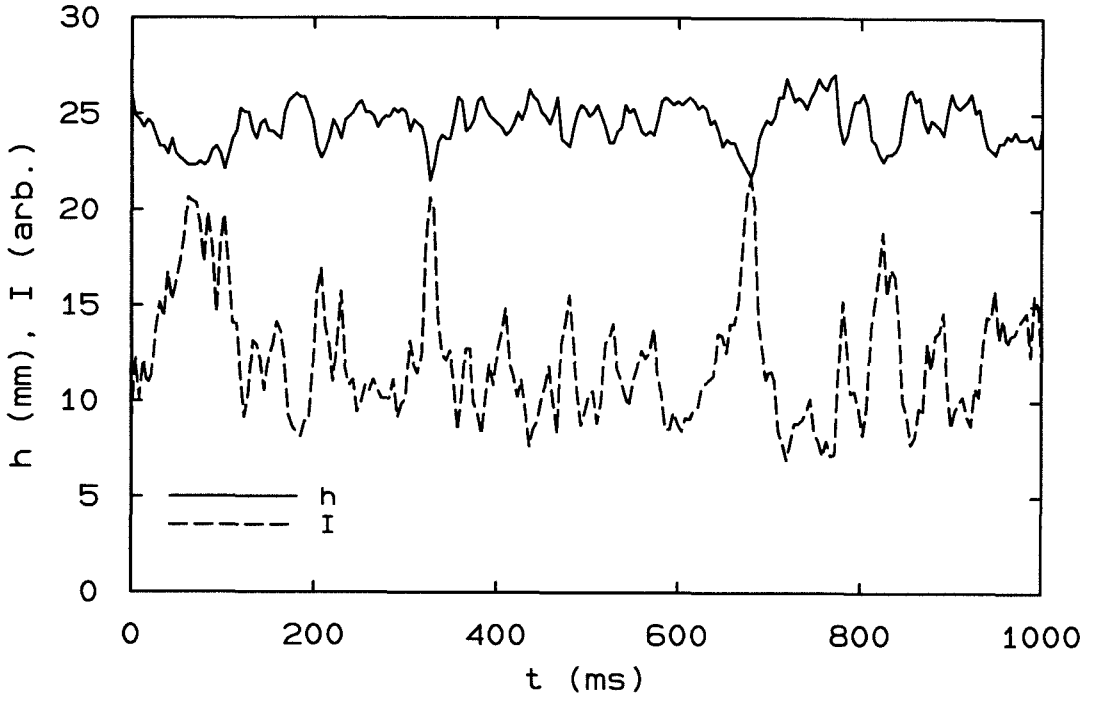

FIG. 4.20 Liftoff height h and light intensity I *vs.* time. C_2H_2, $d = 1.02$ mm, $U_s = 178$ m/s, $x_I = 70$ mm.

bursts.

Portions of the time signals of h and I from the second case in Table 4.7 ($U_s = 178$ m/s) are plotted in Fig. 4.20. It is apparent from the time traces that when the liftoff height drops, the radiation tends to increase, often producing a sharp peak in the I signal.

This is brought out more clearly in a plot of the cross correlations of h and I, which were computed for all four cases in Table 4.7. Results are shown in Fig. 4.21

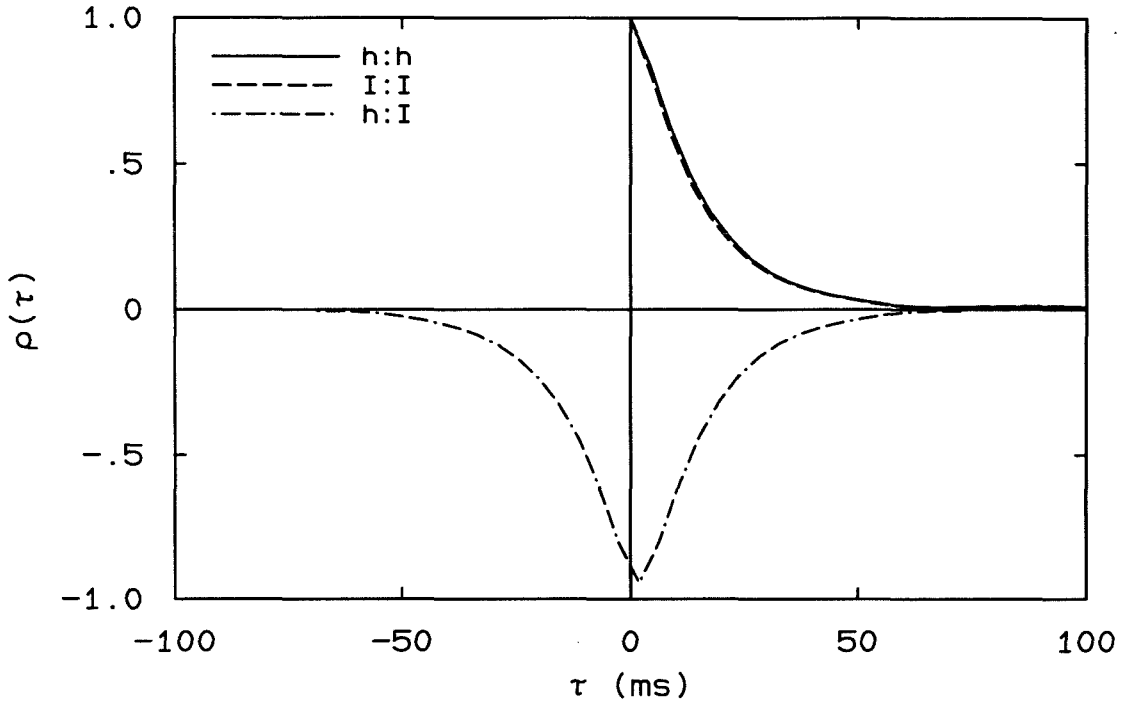

FIG. 4.21 Correlation of h and light intensity I *vs.* time. Same conditions as Fig. 4.20.

for the same case as Fig. 4.20. In the upper right corner are the autocorrelation functions of h and of I. Here, I is shown to have approximately the same correlation time as the liftoff height. In the lower half of the figure is the cross correlation, where a positive time lag is defined as I lagging h. Just as with the cross correlation of h and L reported in the previous section, ρ_{hI} is normalized such that the maximum possible magnitude is one. That the minimum value is so close to -1 is an indication that the two signals are highly, negatively correlated.

It is difficult to discern from the data by how long the change in liftoff height leads the change in radiation, because the temporal resolution is insufficient. The peak in the cross correlation for each case occurs at the shortest measured time lag, *i.e.*, in the same scan of the array, with the time lag arising from x_I corresponding to a pixel which is scanned some time after the pixel corresponding to h. The convection time of fluid traveling at the centerline velocity from the flame base to x_I was estimated as described in Sec. A.7 to be $\sim$ 1.6 ms for the data shown in

Figs. 4.20 and 4.21. This is slightly less than the time lag for the peak in the cross correlation which was measured to be 1.9 ms. However, because of experimental resolution difficulties, with the time between samples being 4 ms, there is a large uncertainty in the measured time lag.

A possible explanation for the large, negative correlation between h and I is that when the flame base drops to a low value, the fuel, which is not as well mixed upstream, has a longer residence time in the hot flame, thereby generating more soot, which greatly increases the radiation. This is a possible mechanism by which the change in liftoff height could cause the radiation to increase.

There are conceptually two possible ways in which the flame radiation could cause the liftoff height to change. In the first scenario, the increased radiation lowers the temperature in the flame, which therefore changes the entrainment, which must act to keep the momentum flux constant (assuming a low Richardson number). It is unlikely that this could affect the liftoff height dynamics, however, because the radiation occurs downstream of the flame base, and the largest affect on the entrainment should also be downstream of the flame base.

The second possibility is that a fraction of the radiation from the flame is absorbed by the gas approaching the flame, thereby raising its temperature and increasing the reaction rate. The faster reaction would cause the flame to be stabilized further upstream, providing a feedback mechanism. The major flaw in this argument is in the magnitude of the possible temperature rise in the reactants entering the flame. Modeling the radiation as a point source of strength equal to 0.4 times the total heat release, located an average distance of $1.5\,\bar{h}$ away from the approaching reactants, taking the velocity along the ray $\eta = 0.15$, and using an extremely conservative estimate for the absorptivity of the mixture to be 0.01 m^{-1}, the calculated temperature rise is less than 0.01 K. More details on the calculation are provided in Sec. A.8. This temperature rise would not be nearly sufficient for a noticeable change in the chemical kinetics which could alter the liftoff height.

The cross correlation functions of the other three cases listed in Table 4.7 are

similar to that of the first case (Fig. 4.21). The minimum correlation value always occurs at the shortest measurable time lag. The values of this minimum correlation for the four cases are: −0.92, −0.94, −0.93, and −0.82. The correlation does drop somewhat for the highest lifted flame. Its radiation is also substantially less than the other cases as indicated in Table 4.7.

To compare these results for acetylene, which radiates brightly from soot production, with less sooting flames, similar experiments were conducted using natural gas, C_2H_6, and C_2H_4. Additionally, measurements of I were made at more than one location. The conditions of the experiments involving fuels other than C_2H_2 are listed in Table 4.8.

Table 4.8: h and I Measurements: n.g., C_2H_6, and C_2H_4

fuel	d (mm)	U_s (m/s)	$\bar{h}$ (mm)	x_I (mm)
n.g.	6.25	60	181	300, 400, 500
C_2H_6	3.88	81	150	240, 340, 440
C_2H_4	2.16	110	73	125, 200

The first condition listed in Table 4.8 involved a non-sooting flame of natural gas at a non-dimensional liftoff height of $\tilde{h} = 2.2$. To determine how the correlation of h and I is affected by the choice of downstream location x_I, measurements of I were made at three positions simultaneously.

The cross correlations of h and I at the three locations are shown in Fig. 4.22. The peak values in the correlations are small, indicating that h does not substantially affect I in non-sooting flames. As x_I is increased, the correlation diminishes, with maximum values of $\rho(\tau)$ being 0.12, 0.070, and 0.036 for x_I = 300, 400, and 500 mm, respectively. Additionally, the sign of the correlation is opposite of that of the sooting C_2H_2 flames. This is a result of the completely different mechanisms of radiation of the two fuels. For natural gas, the radiation comes from chemiluminescence of C_2 and CH radicals. From Fig. 4.22 it appears that an increase

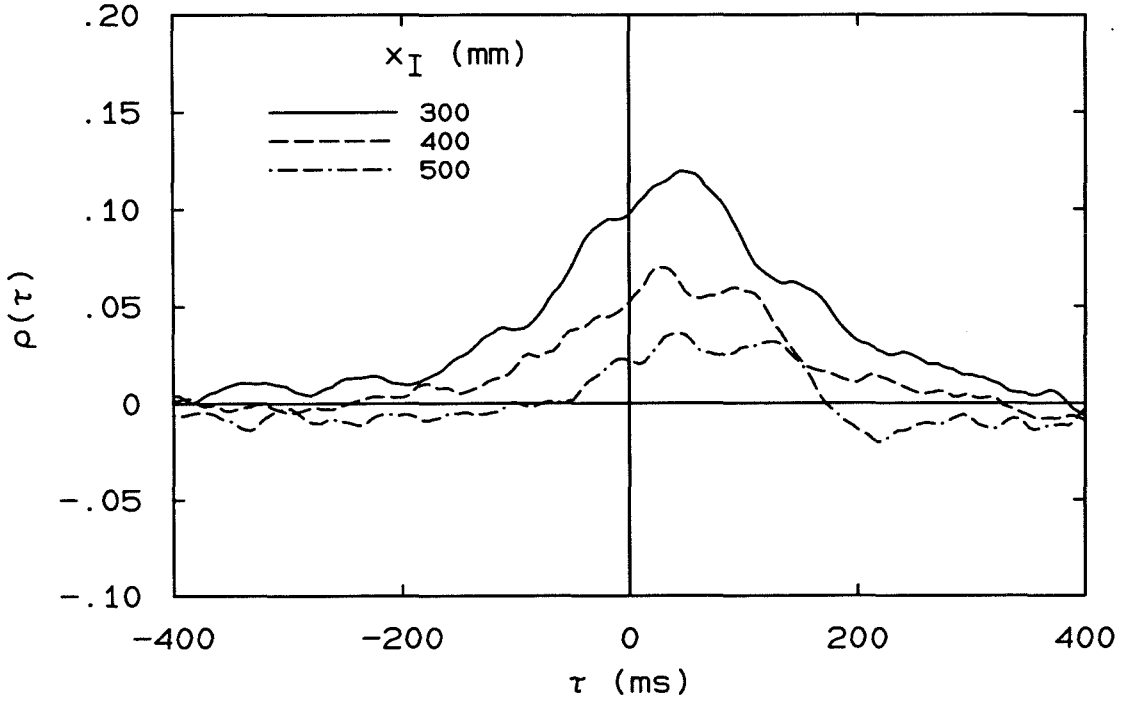

FIG. 4.22 Correlation of h and light intensity I *vs.* time. Natural gas, $d = 6.25$ mm, $U_s = 61$ m/s, $\bar{h} = 181$ mm, $x_I = 300$, 400, and 500 mm.

in liftoff height may increase the total amount of chemical reaction at a location downstream of h. Alternatively, the increase in liftoff height may change the entrainment, and consequently the stoichiometry at the downstream location. This would affect the chemiluminescence, which is very sensitive to composition (*e.g.*, Chomiak 1990). Because the response of the photodiode array is dependent on the wavelength of light, a change in the spectral content of the radiation would change the measurement.

Because the correlation functions are not sharply peaked, it is difficult to identify a time lag at which the correlation is maximum. There does appear to be a slight shift to longer times as the distance downstream x_I is increased. If convection times from $\bar{h}$ to x_I are calculated as described in Sec. A.7, these times are $\tau_c = 13$, 25, and 38 ms for the three values of x_I. The correlation curves peak at larger times than these in general. Also, the measured shift to longer times with increasing x_I is not as extreme as the calculated convection times.

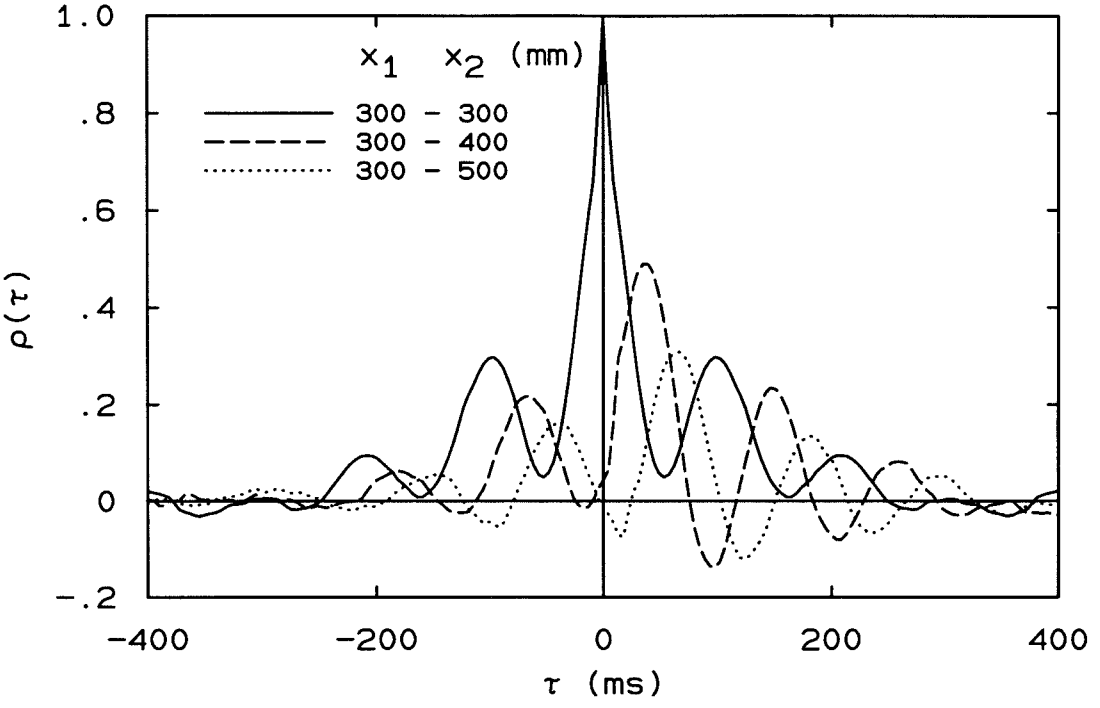

FIG. 4.23 Correlation of light intensity I at different locations x_I *vs.* time. Natural gas, $d = 6.25$ mm, $U_s = 61$ m/s, $\bar{h} = 181$ mm, $x_I = 300$, 400, and 500 mm.

It is also interesting to look at the correlations of I at the different locations. This gives some indication of the convection speed of the flame structures. Cross correlations of $I_1\, I_2$ and $I_1\, I_3$ are shown in Fig. 4.23 along with the autocorrelation of I_1, where the subscripts 1, 2, and 3 correspond to $x_I = 300$, 400, and 500 mm, respectively.

The autocorrelation of I_1 shows quasi-periodic behavior, with a period of 100 ms. For comparison, the estimated large-scale time at $x_{I,1}$ is 15 ms. A buoyancy time defined as $\tau_b \equiv (2\,\delta(x)\,\rho_\infty / g\,\overline{\Delta\rho})^{1/2}$ is $\sim$ 180 ms. It is quite possible that this oscillation is driven by buoyancy.

By having measurements of light intensity at several locations, it is possible to determine the convection times from one location to the next. The peaks in the correlations occur at time lags of 38 and 68 ms for correlations of $I_1\, I_2$ and $I_1\, I_3$, respectively. These are longer than the calculated times of 12 and 25 ms, indicating that the structures convect at speeds lower than the centerline value.

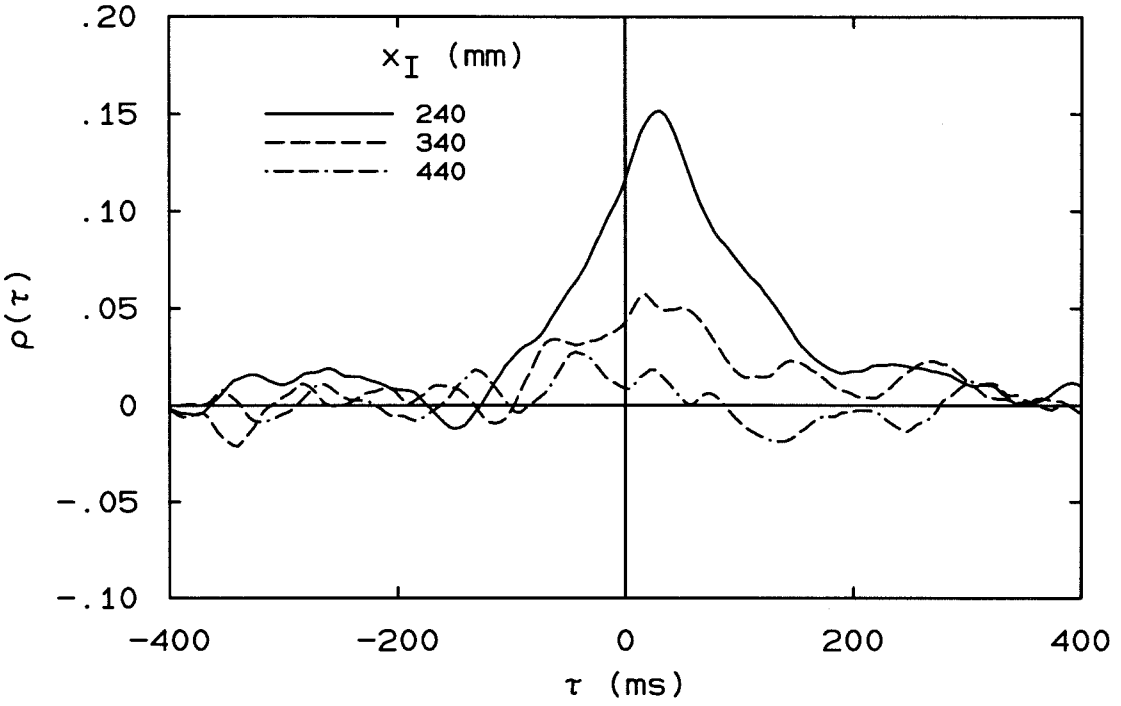

FIG. 4.24 Correlation of h and light intensity I *vs.* time. C_2H_6, $d = 3.88$ mm, $U_s = 81$ m/s, $\bar{h} = 150$ mm, $x_I = 240$, 340, and 440 mm.

Measurements of a C_2H_6 flame, which produces essentially no soot, were also made. The correlations of h and I measured at three different locations are shown in Fig. 4.24. The results are qualitatively similar to those of natural gas. The estimated convection times from $\bar{h}$ to x_I are 9, 16, and 24 ms. The peak in the correlation at $x_I = 300$ mm occurs at ~ 27 ms. No peaks are discernible in the correlations at the other two locations.

Finally, measurements were made with C_2H_4, which does have radiation from soot, although not as much as C_2H_2. The radiation intensity was measured at two locations, $x_I/\bar{h} \approx 1.7$ and 2.7. The lower location $x_{I,1}$ is below the region of intense soot radiation, while $x_{I,2}$ is in the beginning of the sooting region. The cross correlations are shown in Fig. 4.25. At the lower location, there is very little correlation between h and I. At $x_{I,2}$, however, there is a larger (negative) correlation. The correlation is not nearly as strong as that of C_2H_2, however. It peaks at a positive time lag of 9.4 ms, which is close to the calculated convection time from $\bar{h}$ to $x_{I,2}$

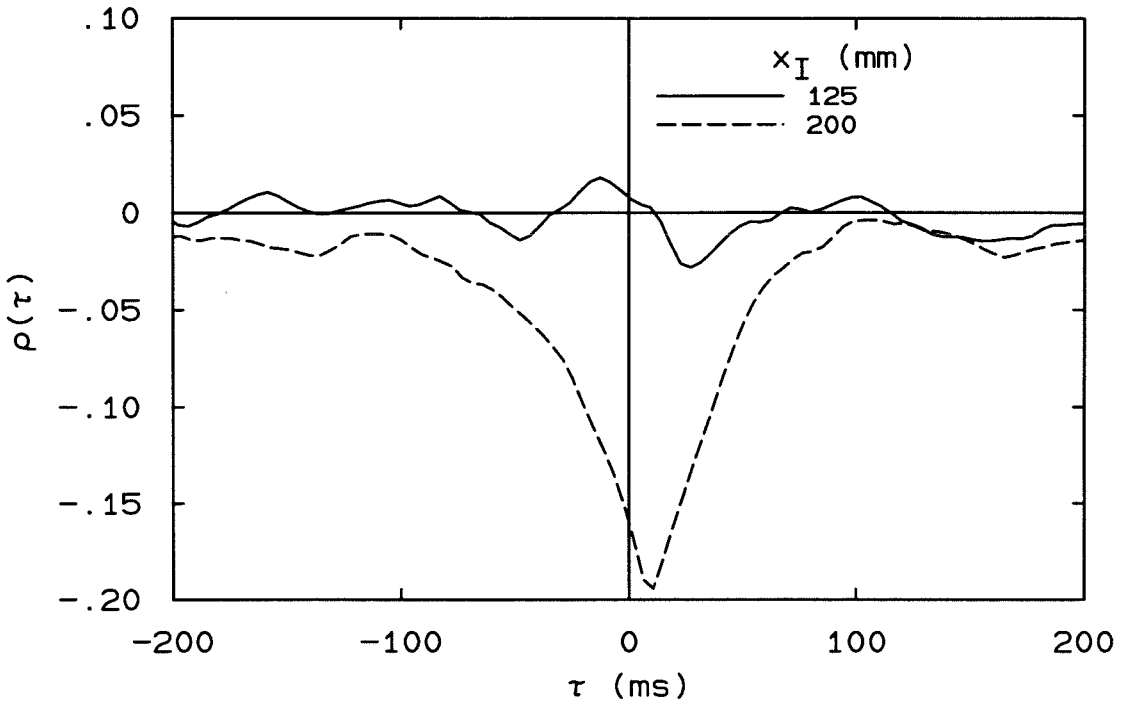

FIG. 4.25 Correlation of h and light intensity I *vs.* time. C_2H_4, $d = 2.16$ mm, $U_s = 110$ m/s, $\bar{h} = 74$ mm, $x_I = 125$ and 200 mm.

of 9 ± 3 ms.

While it was difficult to determine the time by which the soot production lags the liftoff height fluctuations for C_2H_2 because of limitations in the resolution of the measurements, it is clear that this time is approximately the time for fluid to convect from h to x_I for C_2H_4. In all likelihood, this is also the case for C_2H_2 flames as well.

4.6 Discussion

The preceeding results on the temporal behavior of the liftoff height, the simultaneous measurements of h and L, and the measurements of h and I still leave open the question of what determines the time scale of the fluctuations. Although the collapse with ξ_h is compelling, the lack of an effect of nozzle orientation leaves room for speculation. Additional information may be found by examining what happens to the magnitude of the fluctuations as the time scale changes.

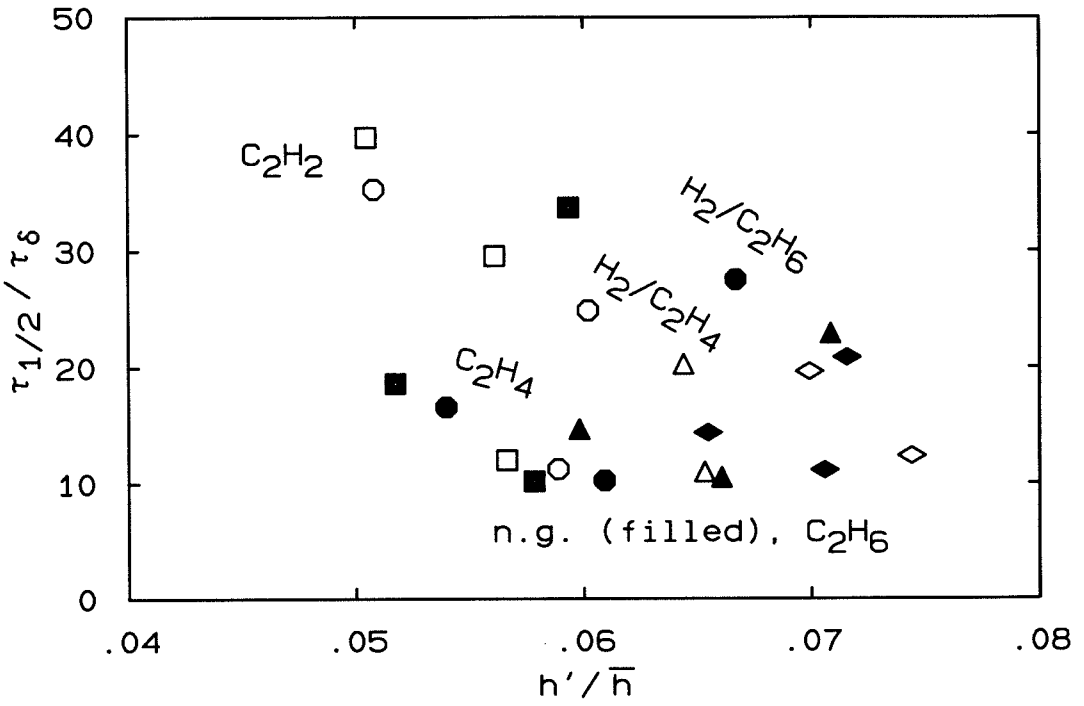

FIG. 4.26 Relation between normalized fluctuations and normalized correlation time at a fixed Reynolds number of Re_h = 22,000. Filled symbols: n.g., C_2H_4, 86% H_2 / 14% C_2H_6.

Figure 4.26 shows $\tau_{1/2}/\tau_\delta$ *vs.* $h'/\bar{h}$ for all the fuels and fuel mixtures for which two different nozzles were used (allowing interpolation to Re_∞ = 22,000). This figure shows that there is not a one-to-one correspondence between $\tau_{1/2}/\tau_\delta$ and $h'/\bar{h}$. Although there is a decrease in $h'/\bar{h}$ and an increase in $\tau_{1/2}/\tau_\delta$ for the fuels: natural gas, C_2H_6, and C_2H_4, the values of $h'/\bar{h}$ are approximately the same for C_2H_4 and C_2H_2, for which $\tau_{1/2}/\tau_\delta$ differs by a factor of 2. Further, for the mixtures of H_2 with C_2H_6 and C_2H_4, values of $h'/\bar{h}$ are comparable to those of natural gas, but $\tau_{1/2}/\tau_\delta$ is much larger. Any explanation of the variation of $\tau_{1/2}/\tau_\delta$ with fuel type must *not* require a corresponding change in the relative rms level of the fluctuations.

It is possible that some subtle property of the fuels is responsible for the variation in $\tau_{1/2}/\tau_\delta$. One candidate is the relative dependence of the chemical properties on Y/Y_{st}. For instance, the laminar flame speed versus Y/Y_{st} data of Egolfopoulos and Law (1991) and Egolfopoulos, Zhu and Law (1991) plotted in Fig. 4.27 show a

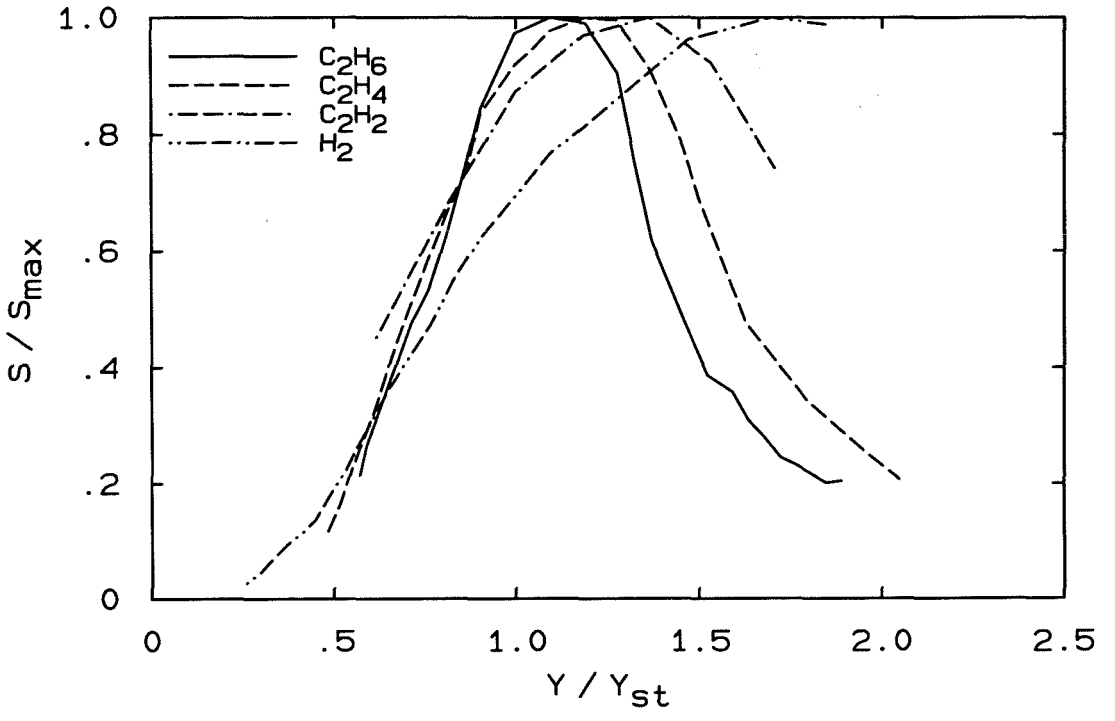

FIG. 4.27 Variation of laminar flame speed with mass fraction. Data for C_2H_6, C_2H_4, and C_2H_2 are from Egolfopoulos, Zhu, and Law (1991); H_2 data are from Egolfopoulos and Law (1991).

widening of the values of Y/Y_{st} for which S/S_{max} is large, in the order of the fuels: C_2H_6, C_2H_4, C_2H_2; this is the same order as the increase in $\tau_{1/2}/\tau_\delta$. The flame speed of hydrogen is also shown. Its curve is wider than any of the other fuels, and it is shifted toward the rich side of stoichiometric. The shapes of the S/S_{max} *vs.* Y/Y_{st} for mixtures of H_2 with C_2H_4 and C_2H_6 have not been measured, but they would likely fall between those of the individual components of the mixture.

4.7 Comparison with other Measurements

Birch and Hargrave (1989) measured liftoff heights of underexpanded natural gas flames. Their mean results have already been discussed in Sec. 3.3.2. They recorded the flame fluctuations using a video camera and automatically searched for the liftoff height along a ray close to the jet edge, rather than by looking at the entire flame base as was done in the current experiments. They reported the

autocorrelation for one of the flow conditions: $d = 50.6$ mm, stagnation pressure = 28.1 bar, $\bar{h} = 2670$ mm, $h' = 186$ mm. From their autocorrelation curve, $\tau_{1/2}$ is found to be ~ 120 ms.

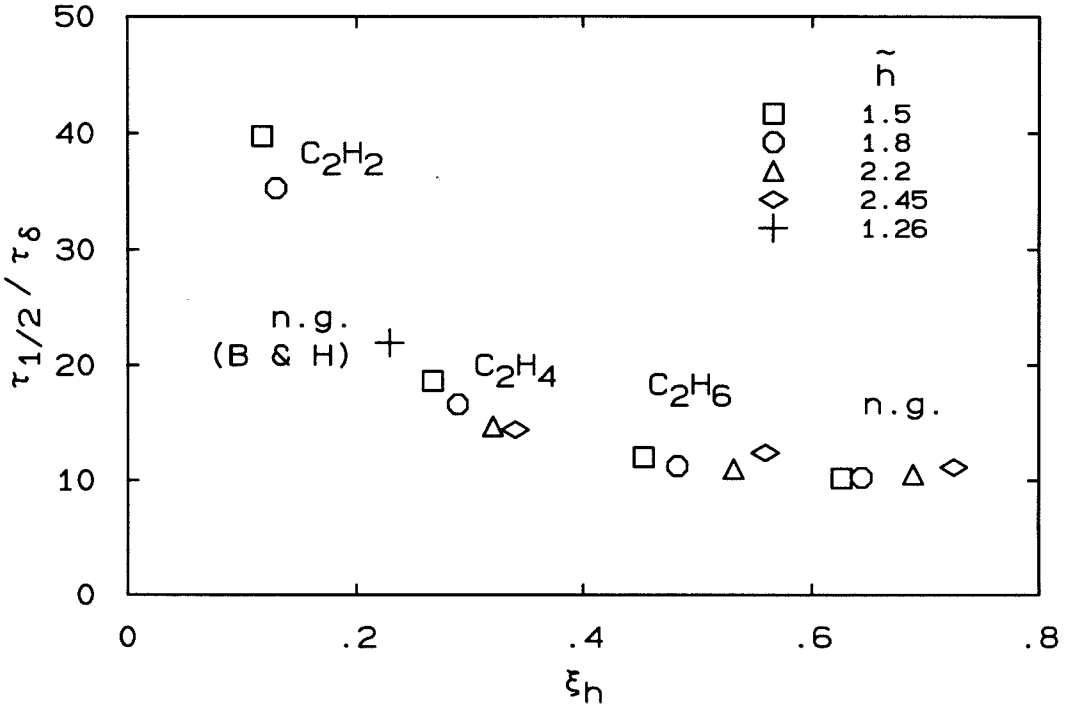

FIG. 4.28 Data point of Birch and Hargrave (1989) (+) plotted on graph of $\tau_{1/2}/\tau_\delta$ *vs.* ξ_h. All other points (open symbols) are at $Re_h = 22{,}000$.

Because of the jet being choked, estimates of the flow conditions at the liftoff height are more difficult. Calculating U_s and d_s by approximating the expansion to atmospheric pressure as an isentropic process, as was done in Sec. 3.3.2, $U_s = 810$ m/s and $d_s = 114$ mm. If the flow conditions are then calculated by the same methods used previously for subsonic jets, the values are $\tilde{h} = 1.3$, $\xi_h = 0.23$, $Re_h = 6.3 \times 10^6$, and $\tau_\delta = 5.5$ ms. The low value of ξ_h for this natural gas flame results from the large Re_∞ (*cf.* Eq. 4.6). The value of $\tau_{1/2}/\tau_\delta \simeq 22$ falls approximately on the curve of $\tau_{1/2}/\tau_\delta$ *vs.* ξ_h, as shown in Fig. 4.28. The other data points in this figure are at $Re_\infty = 22{,}000$. The collapse of $\tau_{1/2}/\tau_\delta$ with ξ_h appears to hold even for values of Re_∞ much greater than those investigated in the current experiments. The uncertainties in the estimates of ξ_h and τ_δ are greater than those

of the current experiments, however. Birch and Hargrave also reported a quasi-periodic aspect to the h *vs.* t signal, with a period of $\sim$ 1.6 s, which is $\sim 300\,\tau_\delta$. They attributed this to the passage of a helical vortex through the flame base, which forces the low point of the flame front to rotate around the periphery of the jet. No such behavior was found in the current measurements.

Another set of measurements on the temporal behavior of lifted flames is that of Chen *et al.* (1989), who measured the radial location of the reaction zone using a thin ceramic filament and a photodiode detector to record the radiation from the filament. They reported values of the rms of the velocity of the flame position divided by the rms of the flame position, which they refer to as a strain rate. Using CH_4 with a 5 mm nozzle, at an exit velocity of 50 m/s and a co-flow velocity of 0.15 m/s, their mean liftoff height was 100 mm. The measured value of their strain rate was 520 s^{-1} at an axial location of 120 mm. Their co-flow velocity was low enough not to significantly affect the jet spreading rate of centerline velocity at $\bar{h}$, and so τ_δ can be estimated from free-jet scaling laws to be $\sim$ 4.2 ms. This gives a value of strain rate times τ_δ of 0.46, indicating that the radial fluctuations of the reaction zone downstream of the liftoff height occur on time scales of order τ_δ, much smaller than the time scales of fluctuations in liftoff height. There is some difficulty in comparing their measured strain rates with values of $\tau_{1/2}$ in the current experiments, however.

4.8 A Simple Model for the Fluctuation Time Scale

A simple model against which to compare the observed long-time behavior of lifted flames is presented here. It is based on the idea of a turbulent flame propagating upstream against the approaching gas, and gives no consideration to the turbulent structure. It is not intended as a plausible explanation for the experimental results, but rather as a simple analysis based on the mean properties of the jet.

It is assumed that the flame base lies on the mean stoichiometric contour and is perturbed about its mean liftoff distance $\bar{h}$, but remains on the contour. The local velocity at the perturbed location $h = \bar{h} + h'$ is given by

$$u(h) = u(\bar{h}) + \frac{\mathrm{d}u}{\mathrm{d}x} h' \ , \tag{4.8}$$

where h' is the perturbation and the derivative is taken along the stoichiometric contour. The propagation speed of the flame S_t will also be changed and is given by

$$S_t(h) = S_t(\bar{h}) + \frac{\mathrm{d}S_t}{\mathrm{d}x} h' \ , \tag{4.9}$$

where, at the equilibrium position, $u(\bar{h}) = S_t(\bar{h})$. Then $h(t)$ is described by

$$\frac{\mathrm{d}h}{\mathrm{d}t} = u(h) - S_t(h) = h' \left(\frac{\mathrm{d}u}{\mathrm{d}x} - \frac{\mathrm{d}S_t}{\mathrm{d}x} \right) \ . \tag{4.10}$$

Assuming that $\frac{\mathrm{d}S_t}{\mathrm{d}x} = 0$ (constant propagation speed along the stoichiometric contour) the time constant of the exponential return to the equilibrium position predicted by this model is

$$\tau_m = 1/(\frac{\mathrm{d}u}{\mathrm{d}x}) \ . \tag{4.11}$$

This derivative is evaluated from

$$\bar{u} = C_u \, U_\mathrm{s} \, \frac{d_\mathrm{s}}{x} \, f_u(\eta) \tag{3.2}$$

where

$$f_u(\eta) = e^{-C'_u \eta^2} \ . \tag{3.2a}$$

Taking the derivative along $\bar{Y} = Y_\mathrm{st}$,

$$\frac{\mathrm{d}u}{\mathrm{d}x} = C_u \, U_\mathrm{s} \, d_\mathrm{s} \left(\frac{1}{x} f'_u(\eta) \frac{\mathrm{d}\eta}{\mathrm{d}x} - \frac{1}{x^2} f_u(\eta) \right) \ . \tag{4.12}$$

$\frac{\mathrm{d}\eta}{\mathrm{d}x}$ is evaluated from the equation for mean concentration,

$$\bar{Y} = C_Y \, \frac{d_\mathrm{s}}{x} \, f_Y(\eta) \tag{3.3}$$

where

$$f_Y(\eta) \;=\; e^{-C'_Y \eta^2} \;, \tag{3.3a}$$

yielding

$$\frac{\mathrm{d}\eta}{\mathrm{d}x} \;=\; -\frac{1}{2\,C'_Y\,\eta\,x} \;. \tag{4.13}$$

Then, $\frac{\mathrm{d}u}{\mathrm{d}x}$ becomes

$$\frac{\mathrm{d}u}{\mathrm{d}x} \;=\; \frac{C_u\,U_\mathrm{s}\,d_\mathrm{s}}{x^2}\,e^{-C'_u\,\eta^2}\,(C'_u/C'_Y - 1) \;. \tag{4.14}$$

Evaluating η from Eq. 3.3,

$$\frac{\mathrm{d}u}{\mathrm{d}x} \;=\; \frac{C_u\,U_\mathrm{s}\,d_\mathrm{s}}{x^2}\left(C_Y\,\frac{d_\mathrm{s}}{Y_\mathrm{st}}\,\bar{h}\right)^{-C'_u/C'_Y}\,(C'_u/C'_Y - 1) \;. \tag{4.15}$$

Noting that $\tau_\delta \;=\; 0.44\,x^2/(C_u\,U_\mathrm{s}\,d_\mathrm{s})$,

$$\tau_m \;=\; \frac{C_Y^{C'_u/C'_Y}}{0.44}\,\frac{1}{C'_u/C'_Y - 1}\,\left(Y_\mathrm{st}\bar{h}/d_\mathrm{s}\right)^{-C'_u/C'_Y}\,\tau_\delta \;. \tag{4.16}$$

Using the values $C_u \;=\; 6.2$, $C'_u \;=\; 94$, $C_Y \;=\; 5.9$, and $C'_Y \;=\; 57$, obtained as described in Sec. A.3,

$$\tau_m \;=\; 56\,\left(Y_\mathrm{st}\bar{h}/d_\mathrm{s}\right)^{-1.65}\,\tau_\delta \;. \tag{4.17}$$

At $Y_\mathrm{st}\bar{h}/d_\mathrm{s} \;=\; 2$, $\tau_m \;=\; 18\,\tau_\delta$, indicating that this model does predict fluctuation times considerably larger than τ_δ. The strong dependence of τ_m on $Y_\mathrm{st}\bar{h}/d_\mathrm{s}$ is *not* realized in the experiments. However, the trend is correct; as $Y_\mathrm{st}\bar{h}/d_\mathrm{s}$ increases, $\tau_{1/2}/\tau_\delta$ decreases, at least for C_2H_4 and C_2H_2.

CHAPTER 5

Imaging of Fuel and Flame Structures

Experiments were conducted in which two-dimensional images of both fuel concentration and reaction zones were obtained. Methane was used as the fuel, and the reaction zones were identified by the presence of CH, which is a reaction intermediate. Methane was imaged by Raman scattering and CH by fluorescence. These experiments were conducted at the Combustion Research Facility of Sandia National Labs, in collaboration with Dr. Robert Schefer and Dr. Mehdi Namazian. The goal of the experiments was to gain insight into the interaction of the turbulent structure of the jet and the flame zones, thereby providing additional understanding of lifted flames, supplementing the global measurements of liftoff height described in previous chapters.

In the flow condition described in this chapter, the fuel was premixed with air, with an initial mass fraction of fuel in the jet fluid of 0.62. The nozzle diameter was 5.4 mm, U_s was 23.7 m/s, and the mean liftoff height was found to be 86 mm, making $\tilde{h} \simeq 1.6$. The Reynolds number was $Re_h = 6{,}700$.

5.1 Apparatus and Instrumentation

As with the experiments discussed previously, the nozzle was designed to have turbulent pipe flow at the exit; its length to diameter ratio was 200. The jet emerged from a solid cylindrical body 50 mm in diameter, as illustrated in Fig. 5.1. The two cameras used to record the images were located 95 mm from the jet centerline, and shields protecting the cylindrical mirrors of the multipass cell were 70 mm from the centerline.

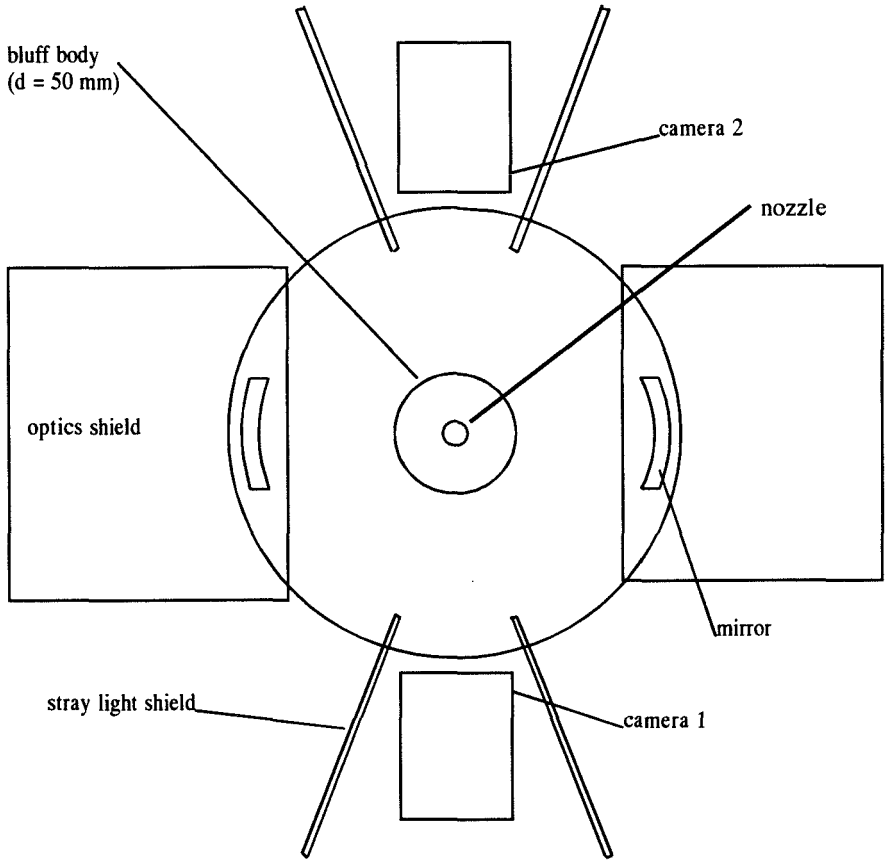

FIG. 5.1 Experimental apparatus used in imaging of CH_4 and CH (top view).

The imaging technique used was that described by Namazian *et al.* (1988). The DIANA facility dye laser at the Sandia Combustion Research Facility was modified to produce a beam with two lines at 431.5 and 444 mm. Using a multipass cell, the beam was formed into a 0.3 mm thick sheet passing through the jet centerline. The 431.5 nm beam caused CH fluorescence at 489 nm, and coincidentally Raman scattering from CH_4 also at 489 nm. To separate the CH_4 and CH contributions, the 444 nm line was used to produce a Raman signal from CH_4 at 510 nm. The signals were recorded with two intensified vidicon detectors located on opposite sides of the laser sheet, one camera with a 10 nm filter centered at 510 nm and the other camera with a 10 nm filter centered at 490 nm. The cameras were gated to stay on for 4 μs. To calibrate the images of both cameras, the test section was

filled with methane using a 100 mm orifice and the scattering signals recorded. By normalizing the measurement of each camera with the signal for pure CH_4 at room temperature, and then taking the difference of the recorded signals from the two cameras, CH_4 and CH were measured separately. Five hundred shots were taken of the flame, and an additional 100 shots of the non-reacting jet were taken.

The normalized CH_4 concentration, denoted $[CH_4]$, is scaled such that a value of 1 represents pure fuel at ambient temperature; it can be converted to number density by multiplying by 2.5×10^{19} molecules/cm^3. The relationship of the CH signal to CH number density depends on temperature and composition. Because some regions very near the flame base may be farther from chemical equilibrium than others, the CH signal is used as a marker of flame position, but not interpreted quantitatively in terms of number density. The CH signal, normalized by the signal for pure CH_4 as described above, is denoted [CH].

In order to increase the resolution of the images, viewing was restricted to one side of the flame using 53 pixels in the horizontal (y) direction and 110 pixels in the vertical (x) direction. This resulted in pixel spacings corresponding to $\sim$ 0.5 mm at the image plane. In the process of aligning the two images before subtracting them (to obtain the [CH] measurement), the data were interpolated and stored as arrays of 90 by 90 elements.

5.2 Observations on Flame Structure

The simultaneous measurements of fuel concentration and reaction zones revealed many interesting features. One observation that can be made is that there is no single, characteristic reaction zone structure of lifted flames. Several shots were selected for presentation to illustrate the range of structure types seen in the images.

Figure 5.2 shows contour plots of $[CH_4]$ and [CH] for one of the shots. The contour levels for $[CH_4]$, starting from the outside, are 0.05, 0.1, 0.15, 0.2, and 0.3.

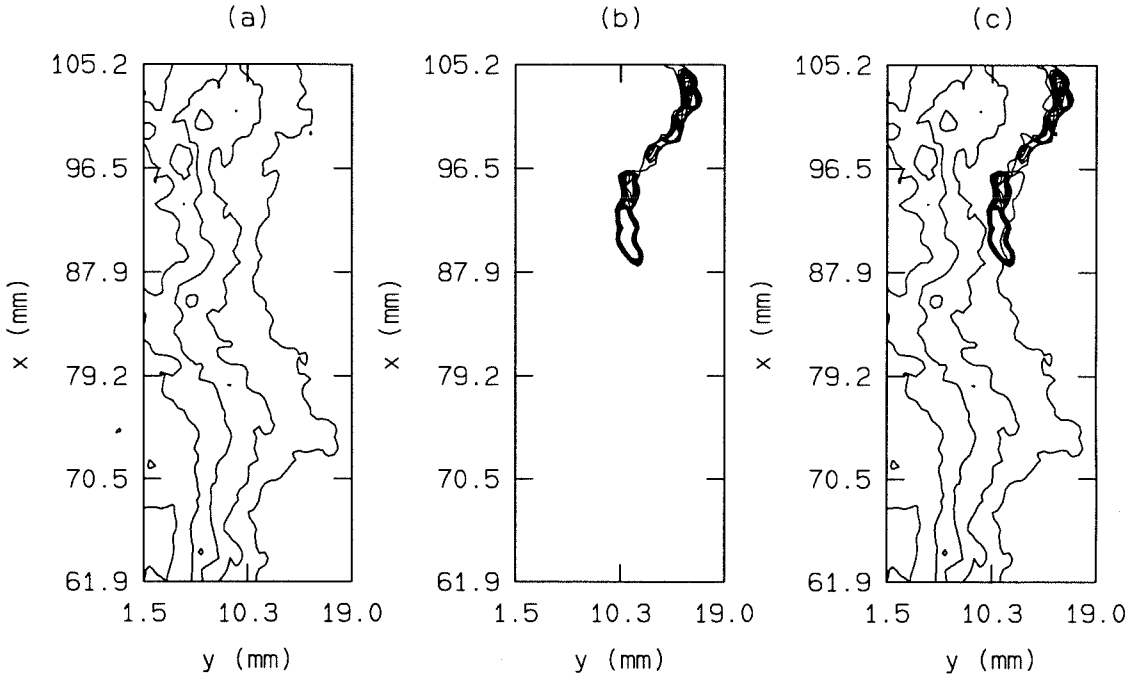

FIG. 5.2 Instantaneous shot illustrating curved reaction zones. Contour plots of (a) CH_4 number density, (b) [CH] signal, and (c) the superposition of (a) and (b). The contour levels for $[CH_4]$ are 0.05, 0.1, 0.15, 0.2, and 0.3. The levels for [CH] are 0.3, 0.34, 0.38, 0.42, 0.46, 0.50, 0.54, 0.58, 0.62, and 0.66.

For reference, the stoichiometric level is 0.095 at room temperature. There are ten contours for [CH], beginning at 0.3, which was found to be a good choice for a threshold to distinguish between burning and non-burning regions. Labeling the individual contours was omitted to keep the figures from being too cluttered.

Figure 5.2 illustrates one of the more common types of flame structure in which the reaction zone lies near the outer edge of the jet, and approximately follows the contour of $[CH_4] = 0.5$ along a curved path, showing evidence of the large structure of the turbulence. The interface is sharp, suggesting that the combustion is taking place in a diffusion-flame like manner, with essentially pure air on the outer side and a fuel-rich mixture on the inner side of the flame. At some locations, the CH_4 concentration on the outer side of the flame is not zero, however.

In other instantaneous images, less evidence of the large turbulent structure is

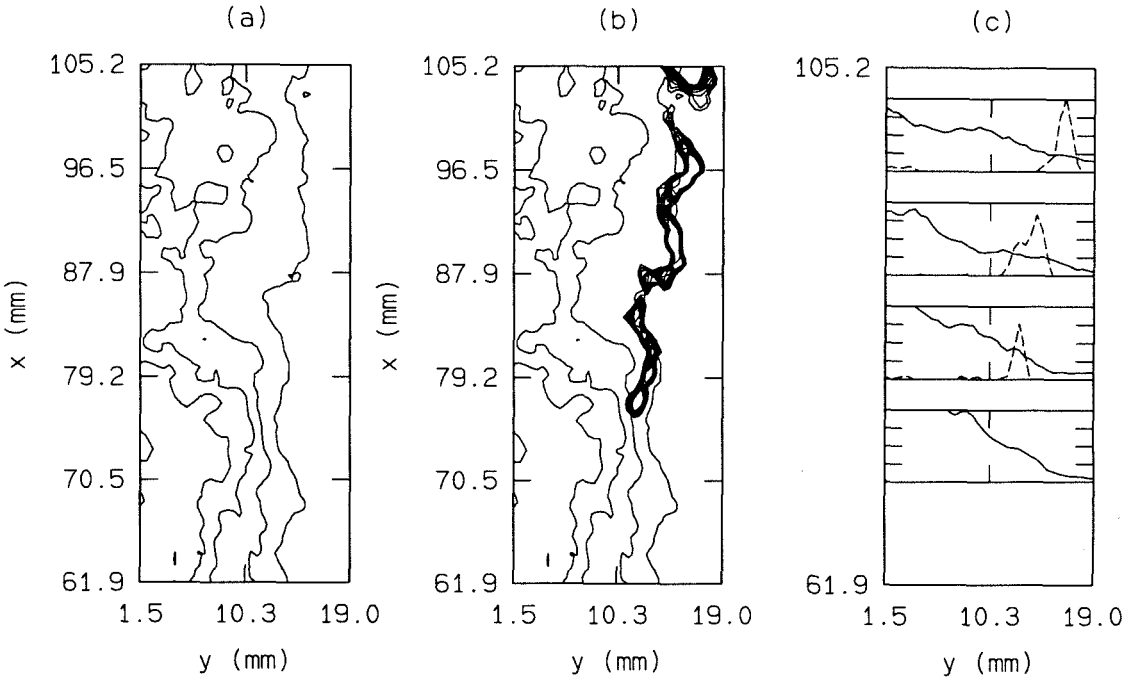

FIG. 5.3 Instantaneous shot illustrating relatively straight reaction zones. (a) $[CH_4]$, (b) $[CH_4]$ and [CH], (c) cuts across flame; solid line $[CH_4]$, vertical axis is $0, \ldots, 0.2$; dashed line [CH], vertical axis is $0, \ldots, 1$. For contour levels see caption of Fig. 5.2.

apparent. Figure 5.3 illustrates this structure type, where the reaction zone is rather straight with small-scale convolutions, again following the $[CH_4] = 0.5$ contour reasonably well. As with Fig. 5.2, the combustion resembles that of a diffusion flame. Four radial cuts have been plotted in (c) to highlight the variation of fuel concentration moving through the reaction zone. There is some unburned fuel on the outer part of the reaction zone, even at the most downstream location plotted.

This structure differs from that of a pure diffusion flame in which no fuel is present on the oxidizer side of the reaction zone. Computational results of Puri *et al.* (1987) are shown in Fig. 5.4 for a counterflow diffusion flame of CH_4, with a strain rate of 55 s^{-1}. The concentrations of CH_4 and CH are plotted as normalized number density to allow direct comparison with the present experimental results, at least for CH_4. The strain rate in the calculation is lower than that in the turbulent flames studied here, where $\bar{\sigma}_I \simeq 175$ s^{-1} (using the result $\bar{\sigma}_I \, \tau_{l_o} \simeq 7.5$, with $\tau_{l_o} \simeq 43$

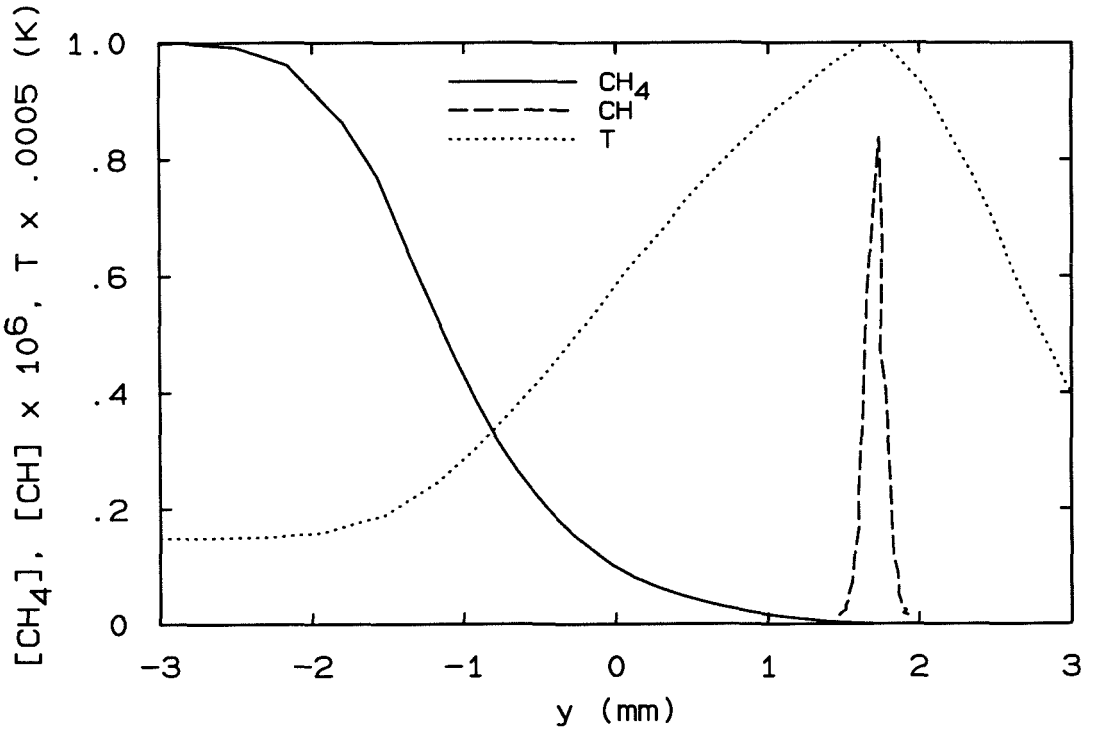

FIG. 5.4 Structure of the reaction zone in a counterflow diffusion flame, from Puri *et al.* (1987), for a strain rate of 55 s^{-1}.

ms, as discussed in Sec. 3.2). The strain rate will affect the profiles, in particular the width of the reaction zone. However, the main point to be made from Fig. 5.4 is that, in a strained diffusion flame, $[CH_4]$ drops to low values before the region of high [CH], and is essentially zero on the oxidizer side of the reaction zone.

Not all of the images suggest that combustion is occurring at the interface between fuel-rich fluid and pure air. In some shots there is a large region of burning at the base of the flame, suggestive of premixed combustion propagating against the oncoming flow. This type of structure is found in Fig. 5.5, where the burning region at the flame base is seen to occur over a range of CH_4 concentrations from 0.05 to 0.1. Above the flame base the flame zone is thinner, appearing more diffusion-like.

In other images such as Fig. 5.6 there are disconnected burning structures. In the three-dimensional flow field, there might be a connection between the different regions seen in the image. These isolated flame structures can be at different axial distances as in Fig. 5.6, or partially overlapping, with one structure closer to the

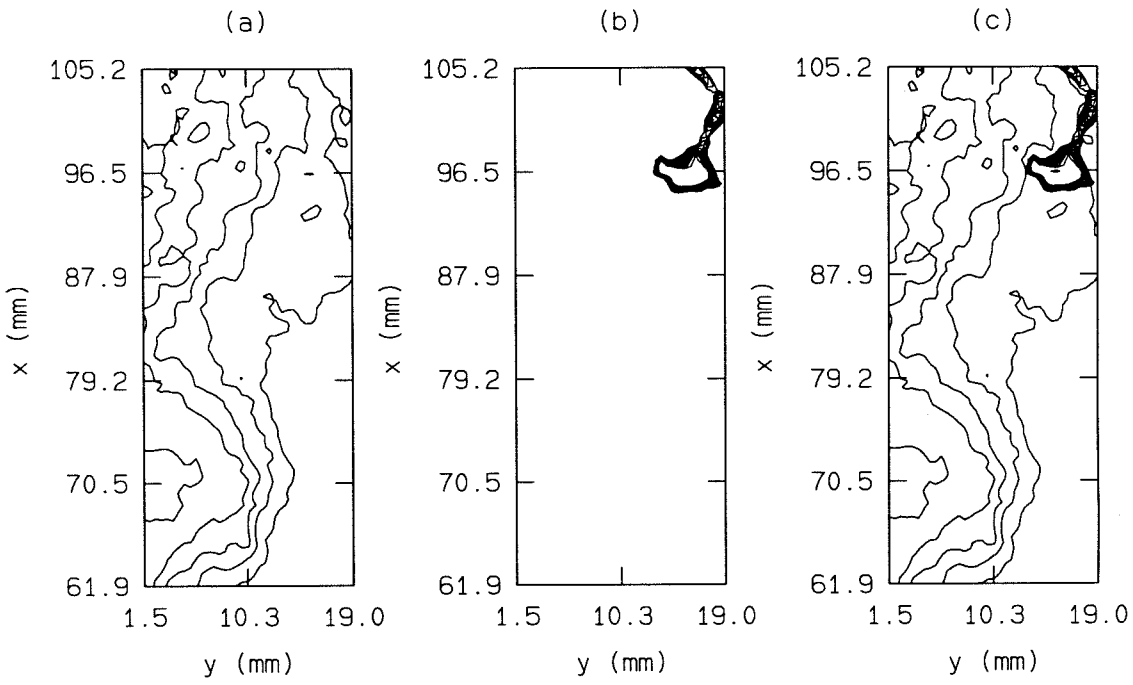

FIG. 5.5 Instantaneous shot resembling premixed combustion. For contour levels see caption of Fig. 5.2.

centerline than the other. There is less of a correlation between the $[CH_4]$ contours and the reaction zones in this image.

5.3 Statistical Measures

Several statistical measures of the structure of the fuel and reaction zones were calculated from the ensemble of the images. Many of these required knowledge of the liftoff height, which was found from the [CH] field. From each image both the liftoff height h and the radial stabilization location y_h were found by searching for the most upstream occurrence of [CH] above a threshold of 0.3. To discriminate from noise in the data, only groups of at least five adjacent array elements above the threshold qualified for finding the liftoff height. Here, adjacent array elements are defined as any of the eight elements surrounding a given element. h is then defined as the most upstream distance within the group, and y_h as the radial location of maximum [CH] in the row at $x = h$.

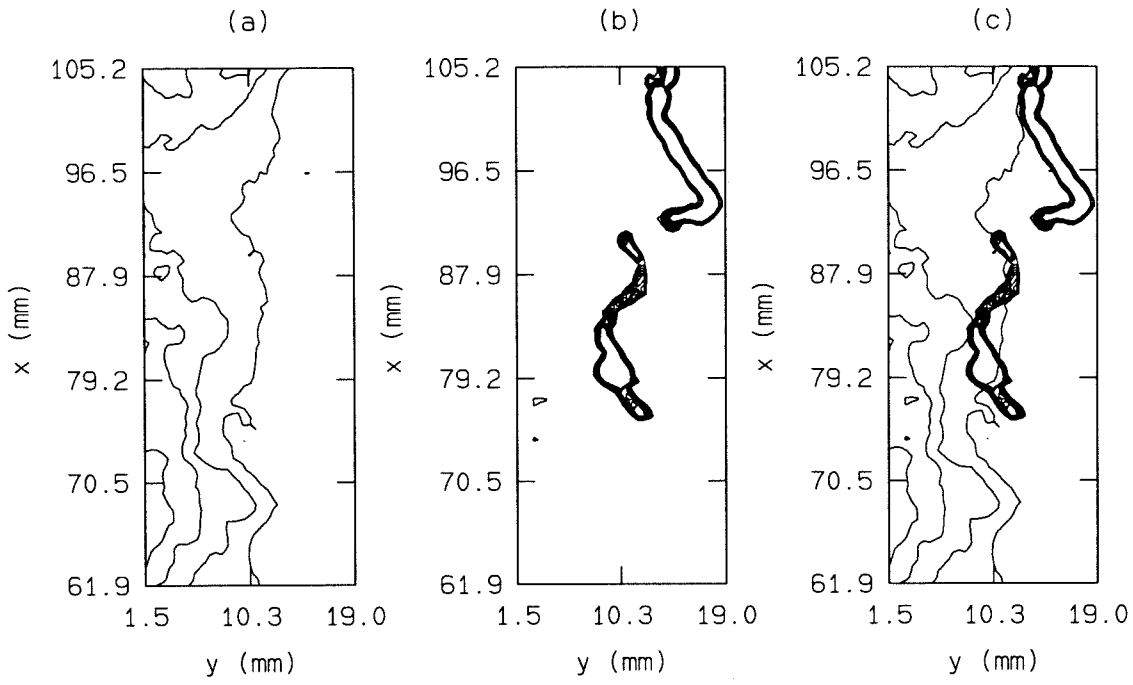

FIG. 5.6 Instantaneous shot illustrating separated reaction zones. For contour levels see caption of Fig. 5.2.

As a quantitative measure of the flame structure, the probability of having burning (defined as [CH] above the threshold) in the vicinity of the liftoff position was calculated. For each image, after finding the liftoff position (both axial h and radial y_h), the presence or absence of burning was recorded versus displacement $(\Delta x, \Delta y)$ from the liftoff position. All the images were then averaged to produce the probability. By definition, the probability of having burning at $\Delta x = \Delta y = 0$ is 1. The results are shown in Fig. 5.7 as a contour plot, where contours levels are shown starting at 0.9 (inner-most curve) and decreasing to 0.1. To keep the plot from being too cluttered, only the levels 0.2 and 0.1 are labeled.

That the contours are more elongated in the vertical direction indicates that the reaction zone at the flame base is most likely to be aligned approximately vertically. The fact that the probability falls off rapidly with distance results from the reaction zones being relatively thin, and having a wide range of orientations. In this averaged representation, there is no one common flame shape which appears.

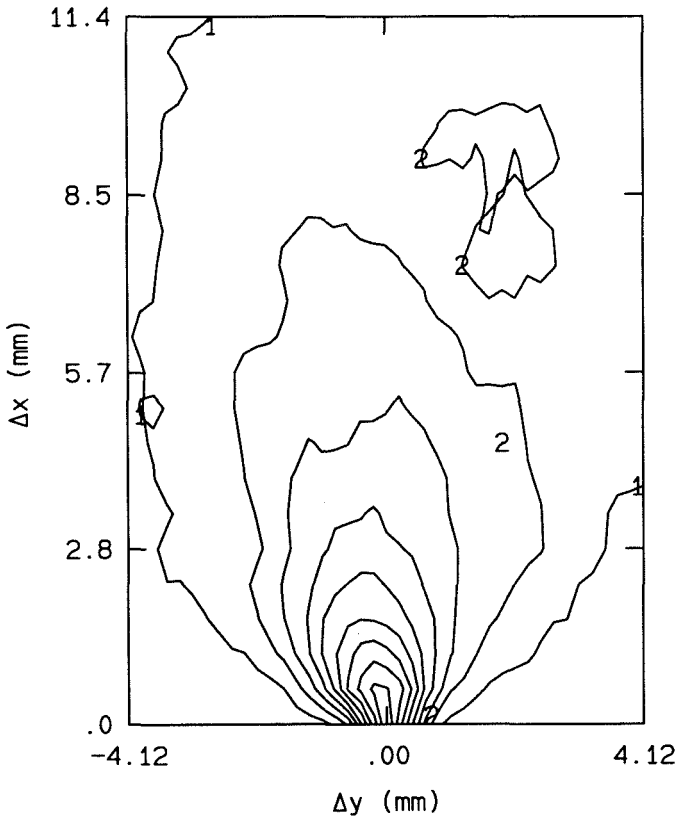

FIG. 5.7 Contours of probability of finding reaction ([CH] > 0.3) at locations displaced from the liftoff location by Δx in the vertical direction and Δy in the horizontal direction. Nine contours are shown from 0.9 to 0.1; only the lowest two contour levels are labeled, 1: 0.1, 2: 0.2.

As with the temporal measurements discussed in Ch. 4, probability density functions can be computed from the data in the imaging experiments. The pdf of h from the imaging data is shown in Fig. 5.8. The pdf is broader than that of the measurements using the photodiode array (Fig. 4.1), having a normalized rms of $h'/\bar{h} = 0.11$. This higher rms and corresponding wider pdf is probably a result of the fact that in the imaging experiments, only a thin slice through one side of the flame is used in determining h, rather than the entire flame base. It is clear from the images that local extinction occurs downstream of the flame base, and this probably occurs at the axial location of the flame base as well. This would cause the measured liftoff height in the imaged plane to fluctuate more than the average over the flame base.

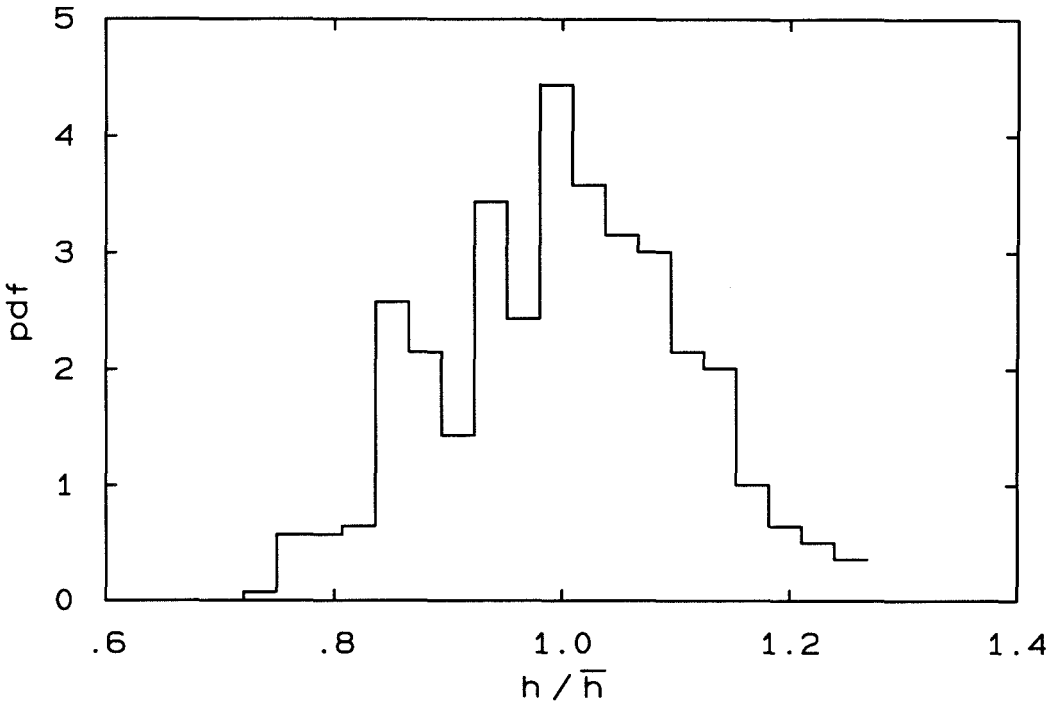

FIG. 5.8 Probability density function of liftoff height.

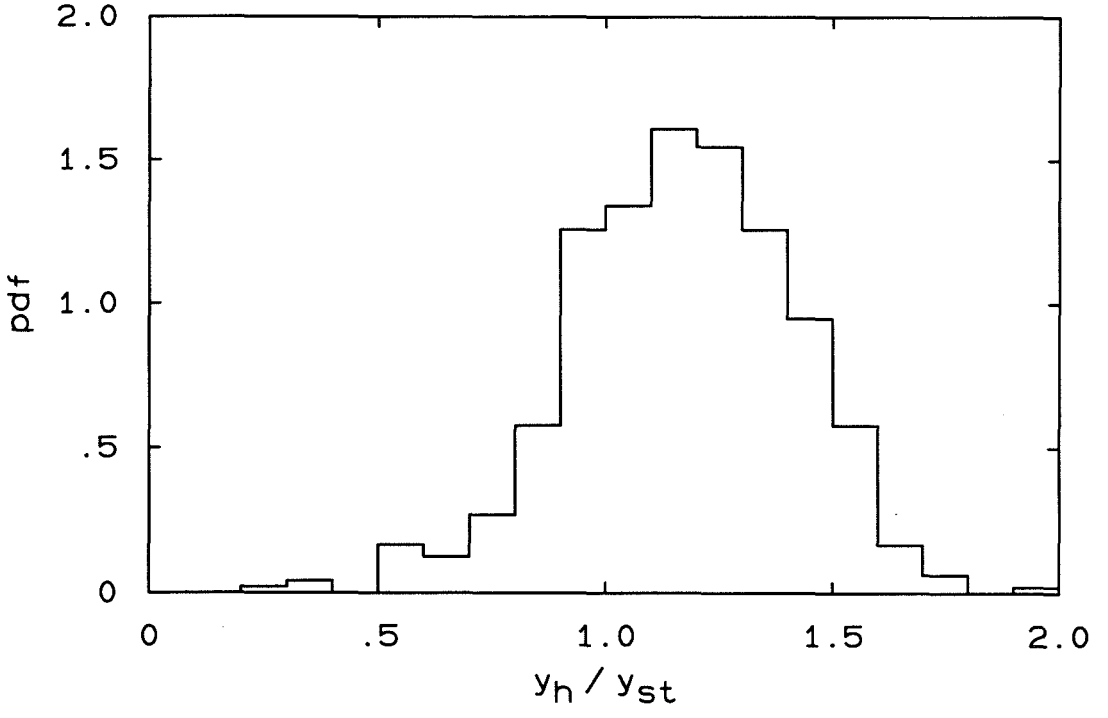

FIG. 5.9 Probability density function of radial position of flame base y_h normalized by y_{st}.

The pdf of the radial flame base position is shown in Fig. 5.9, where y_h has been normalized by y_{st}, the radial position of mean stoichiometric concentration at $x = \bar{h}$, as determined from the shots of a non-reacting jet at the same flow conditions. The peak in the pdf is slightly to the outside (fuel lean side) of the stoichiometric position with a mean value of y_h/y_{st} of 1.17. As with the axial fluctuations, the radial fluctuations are large, with $y'_h/\overline{y_h} = 0.23$ and $y'_h/\bar{h} = 0.033$. Although the flame position never reaches the centerline, the fluctuations are of the order of the jet radial extent.

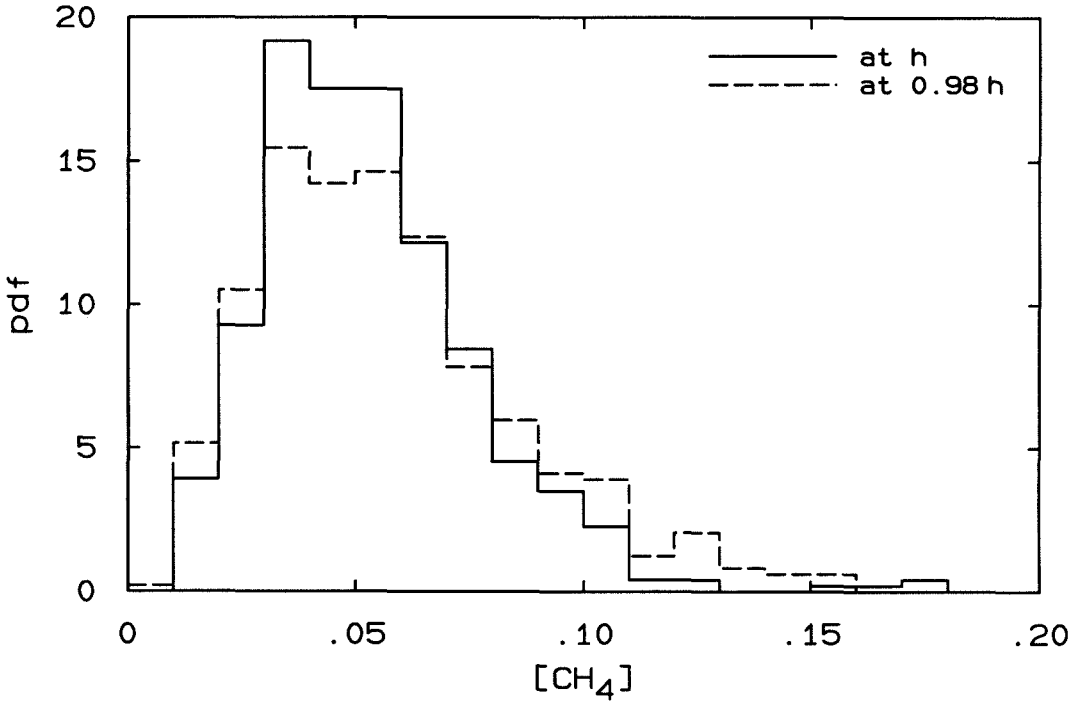

FIG. 5.10 Probability density function of $[CH_4]$ at the flame base ($x = h$, $y = y_h$), and at a location just upstream of the flame base ($x = 0.98\,h$, $y = y_h$).

The pdf of methane number density at the flame base is plotted in Fig. 5.10, along with that at $0.98\,h$, where temperatures are lower. The mean value of $[CH_4]$ at h is 0.054, and at $0.98\,h$ the mean is only slightly higher at 0.058. Both are substantially less than the stoichiometric value at ambient temperature of 0.095. The number density at h is lowered by the higher temperatures in the reaction zone. It is quite possible that heating of the reactants even at $0.98\,h$, which is

$\sim$ 1.4 mm below h, lowers the density somewhat. The pdf at $0.98\,h$ is somewhat broader than at h. This is probably a result of the fuel concentration contours being convoluted, so that moving upstream even 1.4 mm can result in being in a region of either higher or lower concentration. Even the pdf at h is quite wide, with the rms being 45% of the mean.

Noise in the measurements will contribute to the measured rms, and so its contribution must be estimated. For this estimate, both the background rms level n'_0 (at $[CH_4] = 0$) and the rms with the test section filled with methane n'_1 (at $[CH_4] = 1$) were used. The equation

$$n'^2(x,y) \;=\; n'^2_0(x,y) + [CH_4]^2(x,y)\,\left(n'^2_1(x,y) - n'^2_0(x,y)\right)$$

was then used to estimate the noise at each location (x, y), using the mean value of $[CH_4]$. To account for the fluctuation of the radial flame position, the noise was integrated over its pdf, P_{y_h}. *i.e.*,

$$\overline{n'^2} = \int_0^\infty P_{y_h}(y_h)\, n'^2(\bar{h}, y_h)\, \mathrm{d}y_h \;.$$

The integrated noise $\overline{n'^2}$ was found to be 0.014. This is a significant contribution to the measured rms of $[CH_4]$ of 0.024. Accepting this estimate of the noise, the rms of the number density is $(0.024^2 - 0.014^2)^{1/2} \simeq 0.020$, making the number density pdf $0.020/0.024 = 0.83$ times as wide as the one plotted in Fig. 5.10. While there is significant noise in the data, after accounting for it, there is still a large variation of $[CH_4]$ at the flame base.

The large variation is a result of the wide range of conditions present at the flame base at different times. It is not possible to determine whether the mass fraction of CH_4 or the temperature at the flame base varies more, and therefore is the principal cause of the variation in number density of CH_4.

From looking at the images, it appears that the reaction zones follow contours of $[CH_4]$ reasonably well. To get some quantitative measure of this, statistics on the $[CH_4]$ level in the center of the reaction zone at each downstream location x

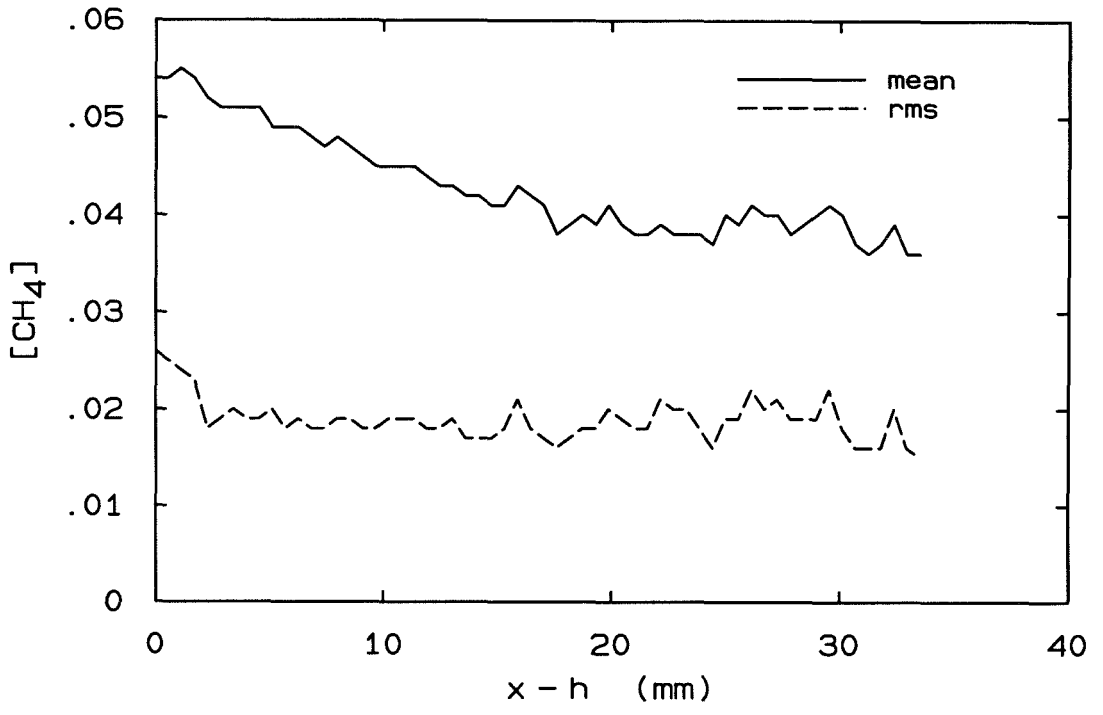

FIG. 5.11 Mean $[CH_4]$ number density at the location of peak [CH] *vs.* distance downstream of h.

above h were computed. Here, the center of the reaction zone is defined as the radial location of maximum [CH], subject to the level being above the threshold for finding h. The mean and rms values of $[CH_4]$ *vs.* $(x - h)$ are shown in Fig. 5.11. The mean $[CH_4]$ level in the reaction zone is 0.54 at the base of the flame, decreases over the next 15 mm to 0.4, then remains at 0.4 for at least the next 15 mm. It is not surprising that the mean level is below the stoichiometric level of 0.95, because of the high temperatures in the reaction zone. In fact, it is rather surprising that the number density is as high as it is even downstream of the liftoff height.

CHAPTER 6

Conclusions and Summary

6.1 Mean Liftoff Heights

Natural gas, C_2H_6, and C_2H_4 exhibit a nearly linear relationship between exit velocity and liftoff height, as had been found by Kalghatgi (1984) for several fuels including CH_4 and C_2H_4. There is, however, a slight decrease in the required velocity needed to achieve a given liftoff height as the nozzle diameter is increased. In non-dimensional terms, $Y_{st}\bar{h}/d_s$ is nearly proportional to $Y_{st}^2\tau_\chi U_s/d_s$, although there is a slight decrease in $Y_{st}^2\tau_\chi U_s/d_s$ at a fixed value of $Y_{st}\bar{h}/d_s$ as the Reynolds number Re_∞ is increased. For acetylene the relationship between U_s and $\bar{h}$ exhibits a large, negative extrapolated intercept to the $\bar{h}$ axis, at least for a 1.0 mm nozzle, for which Re_∞ is less than 15,000. With larger nozzles (and larger Reynolds numbers), the extrapolated (non-dimensional) intercept is reduced.

A strain-rate model based on far-field behavior of turbulent jets provides a plausible explanation for the linear $\bar{h}$ *vs.* U_s relationship. It also accounts for the variation in the slope of the line with fuel type.

Experiments in which air was premixed with the fuel prior to exiting the nozzle showed that the slope of the $(Y_{st}/Y_o)\bar{h}/d_s$ *vs.* $(Y_{st}/Y_o)^2U_s/d_s$ line increases as Y_o is decreased. However, the intercept on the $(Y_{st}/Y_o)\bar{h}/d_s$ axis decreases as Y_o is decreased, creating a fan pattern in the plot. This is in contrast with expectations based on far-field scaling of turbulent jets, which predicts a collapse of the data at any value of Y_o. The discrepancy is attributed to near-field effects, which are more prominent when Y_o is low because such flames are restricted to lower values of $\bar{h}/d_s$ before blowout.

6.2 Fluctuations of the Liftoff Height

The spatial scales of fluctuations in h are of the order of the local large scale of the jet. Values of $h'/\bar{h}$ fall between 0.05 and 0.08. There is an increase in $h'/\bar{h}$ as flames approach blowout, or $\tilde{h}$ becomes large. There is a modest variation of $h'/\bar{h}$ with fuel type, the reason for which is not known.

Time-resolved measurements of the liftoff height revealed that fluctuations occur on time scales considerably longer than the local jet time τ_δ. Using different fuels and flow conditions to achieve different τ_δ, it was found that the normalized correlation time $\tau_{1/2}/\tau_\delta$ is not a constant. Rather, for all the conditions investigated, there is a good collapse with the local Richardson number ξ_h, in which $\tau_{1/2}/\tau_\delta$ increases as ξ_h decreases. Both τ_δ and ξ_h depend largely on the effective fuel chemical time τ_{lo}. The fuels (and fuel mixtures) studied, in order of increasing $\tau_{1/2}/\tau_\delta$, are: natural gas, C_2H_6, C_2H_4, 50% C_2H_2 / 50% C_2H_6, 50% H_2 / 50% C_2H_4, 86% H_2 / 14% C_2H_6, C_2H_2, and 50% H_2 / 50% C_2H_2. Experiments in which the nozzles were oriented horizontally showed no difference in the temporal behavior of h, suggesting that it may not be the influence of buoyancy which is responsible for the variation of $\tau_{1/2}/\tau_\delta$.

Feedback from the flame tip is not responsible for the long correlation times nor for the variation of $\tau_{1/2}/\tau_\delta$ with fuel type. This was confirmed by simultaneously measuring $h(t)$ and the flame length $L(t)$ and finding that they are nearly uncorrelated in time.

There is a monotonic relationship between the measured values of $\tau_{1/2}/\tau_\delta$ and the visible radiation from soot of the above listed fuels, other than the mixtures with hydrogen. In particular, C_2H_2 radiates brilliantly and has substantially higher values of $\tau_{1/2}/\tau_\delta$ than the other fuels. To investigate whether the radiation and liftoff height are correlated in time, simultaneous measurements were made of h and the visible light intensity I at a downstream location in the flames. For C_2H_2 flames, radiation from the flame is strongly, negatively correlated with h. h and I are moderately correlated for C_2H_4, which produces less soot, and nearly uncorrelated

for C_2H_6 and natural gas, which produce essentially no soot under the conditions studied.

This correlation between h and I is not responsible for the variation in $\tau_{1/2}/\tau_\delta$ with fuel type, however. Measurements with fast, non-sooting mixtures of H_2 with C_2H_6 and C_2H_4, with values of τ_δ and ξ_h close to those of C_2H_2, revealed comparable values of $\tau_{1/2}/\tau_\delta$.

There is not a-one-to one correspondence between $\tau_{1/2}/\tau_\delta$ and $h'/\bar{h}$. This eliminates any explanation of the variation of $\tau_{1/2}/\tau_\delta$ with fuel type which would require a corresponding change in $h'/\bar{h}$.

It is possible that the variation in $\tau_{1/2}/\tau_\delta$ with fuel type results from details of the chemical properties of the fuels, rather than ξ_h. In particular, the dependence of the reaction rate on composition may change the structure at the flame base and hence the flame stability. There is a correspondence between $\tau_{1/2}/\tau_\delta$ measured in these experiments and the width of the curve of laminar flame speed *vs.* Y/Y_{st}.

6.3 Imaging of Fuel and Reaction Zones

Planar images of methane number density and CH (to mark the reaction zones) were taken of a flame lifted to $\tilde{h} = 1.6$ at a Reynolds number of $Re_h = 6{,}000$. In some of the images the large-scale structure of the turbulence is quite evident, with large, curved reaction zones, located near the outer part of the jet. Sometimes there there are multiple, separated reaction zones suggesting local extinction. In other images the reaction zones are rather straight, but still located near the outer edge of the jet, suggesting diffusion-like combustion. Not all of the images appear to have combustion taking place in a diffusion-like manner, however. There is sometimes a large region at the base of the reaction zone which appears to be premixed flame propagation, followed by more diffusion-like reaction zones downstream. Even in the diffusion-like structures, the concentration of CH_4 was not zero on the air side of the reaction zone.

Fluctuations in both the axial (h) and radial (y_h) flame stabilization location were found to be large, on the order of the local jet width δ, with $h'/\bar{h} = 0.011$ and $y_h'/\bar{h} = 0.033$. The mean value of y_h was found to be $\sim 1.2\, y_{\rm st}$, where $y_{\rm st}$ is the location of mean stoichiometric concentration in the non-reacting jet. At the flame base, the mean value of $[CH_4]$, the number density normalized by that of pure fuel at ambient temperature, was found to be 0.054. Large variations in $[CH_4]$ at the flame base were observed in the individual shots.

6.4 Summary

Measurements of mean liftoff height confirmed the nearly linear dependence of $\bar{h}$ on $U_{\rm s}$, with a slight increase in $\bar{h}$ with Reynolds number. This linear dependence is in agreement with a strain-rate model based on the far-field scaling of turbulent jets. When increased amounts of air are added to the nozzle fluid, the slope of the $\bar{h}$ *vs.* $U_{\rm s}$ line increases faster than predicted by far-field jet scaling. The spatial scales of the fluctuations of h were found to be of the order of the jet large scale, while the time scales were found to be much larger than the local large-scale time. The non-dimensional fluctuation time varies with fuel type, and collapses with the Richardson number at the flame base, ξ_h. There is no change in the measured fluctuation time scale when the nozzles are oriented horizontally, suggesting that the fluctuation time scale may depend on some parameter other than ξ_h. The variation is not caused by feedback from the flame tip nor by feedback from radiation. It may be due to details of the chemistry of the fuels. Experiments in which fuel concentration and reaction zones were imaged showed a large range of structure types. Large variations in the axial and radial flame stabilization location and fuel number density at the flame base were observed.

APPENDIX A

Calculation of Fluid Flow Quantities

A.1 Momentum Velocity and Momentum Diameter

From the calculated mean velocity exiting the nozzle U_o, obtained as described in Sec. 2.1.1, the equivalent source velocity U_s was calculated, along with the equivalent source diameter d_s. U_s and d_s are defined in terms of the momentum flux J_o and mass flux $\dot{m}_o$ exiting the nozzle by the solution of the equations

$$\begin{aligned} \dot{m}_o &= \rho_\infty \frac{\pi}{4} d_s^2 U_s \\ J_o &= \rho_\infty \frac{\pi}{4} d_s^2 U_s^2 \, . \end{aligned} \tag{A.1}$$

To calculate U_s and d_s, the mean velocity profile for turbulent flow in a pipe as reported by Nikuradse (1932) was used,

$$\frac{u}{u_{cl}} = \left(1 - \frac{r}{r_o}\right)^n \, , \tag{A.2}$$

where u_{cl} is the centerline velocity, r is the radial coordinate, and r_o is the nozzle radius. The exponent n depends on the pipe flow Reynolds number $Re_o \equiv (\rho_o U_o d)/\mu_o$, as reported by Nikuradse.

By integrating the velocity profiles, U_s and d_s are found to be

$$\frac{U_s}{U_o} = \frac{(n+1)(n/2+1)^2}{(2n+1)} \tag{A.3}$$

and

$$\frac{d_s}{d} = \left(\frac{\rho_o}{\rho_\infty}\right)^{1/2} \left(\frac{(2n+1)}{(n+1)(n/2+1)^2}\right)^{1/2} \, . \tag{A.4}$$

To a reasonable approximation for the Reynolds numbers investigated ($10{,}000 < Re_o < 50{,}000$),

$$\begin{aligned} U_s &= 1.02\, U_o \\ d_s &= 0.99\, (\rho_o/\rho_\infty)^{1/2}\, d \, . \end{aligned} \tag{A.5}$$

A.2 Mean Strain Rate

The mean strain rate in the far field of a turbulent jet can be obtained from the mean velocity profile,

$$\bar{u} \;=\; C_u\, U_s\, \frac{d_s}{x}\, f_u(\eta)\;. \tag{3.2}$$

From the continuity equation, the radial velocity is obtained,

$$\bar{v} \;=\; -\frac{1}{r}\int_0^r \hat{r}\,\frac{\partial \bar{u}}{\partial x}\,\mathrm{d}\hat{r}\;. \tag{A.6}$$

Using Eq. 3.2, this becomes

$$\bar{v} \;=\; C_u\,\frac{U_s\, d_s}{x}\left(\eta\, f_u(\eta) - \frac{1}{\eta}\int_o^\eta \hat{\eta}\, f_u(\hat{\eta})\,\mathrm{d}\hat{\eta}\right)\;. \tag{A.7}$$

Partial derivatives of the velocity components are then given by

$$\begin{aligned}
\frac{\partial \bar{u}}{\partial x} &= -C_u\,\frac{U_s\, d_s}{x^2}\left(\eta\, f_u'(\eta) + f_u(\eta)\right)\\
\frac{\partial \bar{u}}{\partial r} &= C_u\,\frac{U_s\, d_s}{x^2}\, f_u'(\eta)\\
\frac{\partial \bar{v}}{\partial x} &= -C_u\,\frac{U_s\, d_s}{x^2}\left(\eta^2\, f_u'(\eta) + \eta\, f_u(\eta)\right) \;=\; \eta\,\frac{\partial \bar{u}}{\partial x}\\
\frac{\partial \bar{v}}{\partial r} &= C_u\,\frac{U_s\, d_s}{x^2}\left(\eta\, f_u'(\eta) + \frac{1}{\eta^2}\int_0^\eta \hat{\eta}\, f_u(\hat{\eta})\,\mathrm{d}\hat{\eta}\right)\;.
\end{aligned} \tag{A.8}$$

The strain rates are given by

$$\begin{aligned}
\bar{\sigma}_{xx} &= \frac{\partial \bar{u}}{\partial x}\\
\bar{\sigma}_{rr} &= \frac{\partial \bar{v}}{\partial r}\\
\bar{\sigma}_{xr} &= \frac{1}{2}\left(\frac{\partial \bar{u}}{\partial r} + \frac{\partial \bar{v}}{\partial x}\right)\\
\bar{\sigma}_{\theta\theta} &= \frac{\bar{v}}{r} \;=\; C_u\,\frac{U_s\, d_s}{x^2}\left(f_u(\eta) - \frac{1}{\eta^2}\int_o^\eta \hat{\eta}\, f_u(\hat{\eta})\,\mathrm{d}\hat{\eta}\right)\;.
\end{aligned} \tag{A.9}$$

Using a Gaussian for the velocity function,

$$f_u(\eta) \;=\; e^{-C_u'\,\eta^2}\;, \tag{A.10}$$

these become

$$\begin{aligned}
\frac{\partial \bar{u}}{\partial x} &= C_u \frac{U_s d_s}{x^2} \left(2 C_u' \eta^2 - 1\right) e^{-C_u' \eta^2} \\
\frac{\partial \bar{u}}{\partial r} &= -2 C_u' C_u \frac{U_s d_s}{x^2} \eta \, e^{-C_u' \eta^2} \\
\frac{\partial \bar{v}}{\partial r} &= -C_u \frac{U_s d_s}{x^2} \left(2 C_u' \, e^{-C_u' \eta^2} + \frac{1}{2 C_u' \eta^2} \left(e^{-C_u' \eta^2} - 1\right)\right) \\
\bar{\sigma}_{\theta\theta} &= C_u \frac{U_s d_s}{x^2} \left(f_u(\eta) - \frac{1}{\eta^2} \int_0^\eta \hat{\eta} \, f_u(\hat{\eta}) \, \mathrm{d}\hat{\eta}\right) .
\end{aligned} \tag{A.11}$$

The principal strain rates in the x-r plane are

$$\begin{aligned}
\bar{\sigma}_\alpha &= \frac{\bar{\sigma}_{xx} + \bar{\sigma}_{rr}}{2} + \sqrt{\left(\frac{\bar{\sigma}_{xx} - \bar{\sigma}_{rr}}{2}\right)^2 + \bar{\sigma}_{xr}^2} \\
\bar{\sigma}_\beta &= \frac{\bar{\sigma}_{xx} + \bar{\sigma}_{rr}}{2} - \sqrt{\left(\frac{\bar{\sigma}_{xx} - \bar{\sigma}_{rr}}{2}\right)^2 + \bar{\sigma}_{xr}^2} .
\end{aligned} \tag{A.12}$$

The most compressive strain rate, $\bar{\sigma}_{\mathrm{III}}$, is the minimum of $\bar{\sigma}_\alpha$, $\bar{\sigma}_\beta$, and $\bar{\sigma}_{\theta\theta}$. The most extensive strain rate, $\bar{\sigma}_{\mathrm{I}}$, is the maximum of the three.

A.3 Velocity, Concentration, Density just below Flame Base

The centerline velocity in the far field of a non-buoyant, non-reacting jet is given by

$$U_{\mathrm{cl}} = C_u U_s \frac{d_s}{x} . \tag{A.13}$$

This equation relies on the fact that as $x \to \infty$, $\rho \to \rho_\infty$. Provided that $\bar{h}$ is out of the near field, and far enough downstream that $\rho \approx \rho_\infty$, Eq. A.13 provides an adequate estimate for U_{cl} at $x = \bar{h}$. This is sufficiently accurate for all of the conditions presented here, except those using a mixture of 86% H_2 / 14% C_2H_6, for which the centerline density at $x = \bar{h}$ is considerably less than ρ_∞. In order to obtain a more accurate estimate for U_{cl} in those flames, another method for estimating U_{cl}, as well as Y_{cl}, was employed.

The momentum flux J and mass flux of fuel $\dot{m}_f$ remain constant at any axial location x below the flame. The time-averaged values of $\dot{m}_f$ and J are given by

$$\begin{aligned} \dot{m}_f &= \int_0^\infty \left[\overline{\rho Y}\,\overline{u} + \overline{(\rho Y)' u'}\right] 2\pi r \,\mathrm{d}r \\ J &= \int_0^\infty \left[\overline{\rho}\,\overline{u}^2 + \overline{\rho}\,\overline{u'^2} + 2\,\overline{u}\,\overline{u'\rho'} + \overline{\rho' u'^2}\right] 2\pi r \,\mathrm{d}r \ . \end{aligned} \tag{A.14}$$

The $\overline{\rho' u'^2}$ term was assumed to be small, and was neglected in the momentum equation; all other terms were estimated from measurements in turbulent jets. The radial behavior of u and Y were assumed to be given by the similarity functions

$$\begin{aligned} \frac{\bar{Y}}{Y_{\mathrm{cl}}} &= f_Y(\eta) \\ \frac{\bar{u}}{U_{\mathrm{cl}}} &= f_u(\eta) \\ \frac{\sqrt{\overline{u'^2}}}{U_{\mathrm{cl}}} &= f_{u'}(\eta) \\ \frac{\sqrt{\overline{Y'^2}}}{Y_{\mathrm{cl}}} &= f_{Y'}(\eta) \\ \frac{\overline{Y' u'}}{Y_{\mathrm{cl}}\, U_{\mathrm{cl}}} &= f_{Y'u'}(\eta) \ . \end{aligned} \tag{A.15}$$

It was assumed that the statistics of u and Y are unaffected by the initial density ratio ρ_o/ρ_∞. The functions in Eq. A.15 were estimated from measurements in turbulent jets. The concentration functions f_Y and $f_{Y'}$ were taken from data of Dowling (1988). The mean velocity function f_u was taken from Chen and Rodi (1980) and the rms velocity function $f_{u'}$ from Wygnanski and Fiedler (1969). The cross correlation function of velocity and concentration $f_{Y'u'}$ was obtained from measurements of So *et al.* (1990) who reported velocity-density correlations in a jet with an initial density ratio of $\rho_o/\rho_\infty = 0.64$.

The density as a function of mass fraction is given by

$$\frac{\rho}{\rho_\infty} = \frac{1}{Y(\mathrm{MW}_\infty/\mathrm{MW}_o - 1) + 1} \ . \tag{A.16}$$

To obtain estimates for the terms in Eq. A.14 involving ρ', Eq. A.16 was linearized about $\bar{Y}$:

$$\rho' \approx \frac{\mathrm{d}\rho}{\mathrm{d}Y} Y' \ . \tag{A.17}$$

Equations A.14 can then be combined with the similarity functions in Eq. A.15 to obtain two simultaneous equations for $U_{\rm cl}$ and $Y_{\rm cl}$,

$$1/8\left(\frac{d_{\rm s}}{x}\right)^2 = Y_{\rm cl}\frac{U_{\rm cl}}{U_{\rm s}}\int_0^\infty\left[\frac{\rho}{\rho_\infty}f_Y f_u + Y_{\rm cl}\frac{1}{\rho_\infty}\frac{{\rm d}\rho}{{\rm d}Y}f_{Y'}^2 f_u + \left(Y_{\rm cl}\frac{1}{\rho_\infty}\frac{{\rm d}\rho}{{\rm d}Y}f_Y + \frac{\rho}{\rho_\infty}\right)f_{Y'u'}\right]\eta\,{\rm d}\eta \tag{A.18}$$

$$1/8\left(\frac{d_{\rm s}}{x}\right)^2 = \left(\frac{U_{\rm cl}}{U_{\rm s}}\right)^2\int_0^\infty\left[\frac{\rho}{\rho_\infty}(f_u^2+f_{u'}^2) + Y_{\rm cl}\frac{2}{\rho_\infty}\frac{{\rm d}\rho}{{\rm d}Y}f_u f_{Y'u'}\right]\eta\,{\rm d}\eta\ .$$

Equations A.18 were solved for $Y_{\rm cl}$ and $U_{\rm cl}$ at the location $x = \bar{h}$. When $\rho/\rho_\infty = 1$, these equations reduce to the asymptotic forms

$$\begin{aligned} U_{\rm cl} &= C_u\,U_{\rm s}\frac{d_{\rm s}}{x} \\ Y_{\rm cl} &= C_Y\frac{d_{\rm s}}{x} \end{aligned} \tag{A.19}$$

with the values of $C_u = 6.17$ and $C_Y = 5.92$ found from the solution of Eqs. A.18. This value of C_u is very close to the value reported by Chen and Rodi (1980) of 6.2. The value for C_Y obtained from Eq. A.18 is somewhat higher than previously measured values, however. Chen and Rodi recommend 5.0, and Dowling (1988) finds $C_Y = 5.0$ at $Re = 5{,}000$ and 4.7 at $Re = 16{,}000$.

A.4 Non-Dimensional Liftoff Height

The definition chosen for the non-dimensional liftoff height relies on the concentration field of the jet. Because the fuels studied have maximum reaction rates at compositions near the stoichiometric value $Y_{\rm st}$, it was decided that selecting a parameter that would be a function of $\eta_{\rm st}$, the value of η for which $\bar{Y} = Y_{\rm st}$, would be the best choice.

In the far field of the jet, the mean concentration field is given by

$$\bar{Y} = C_Y\,Y_o\frac{d_{\rm s}}{x}f_Y(\eta)\,. \tag{3.3}$$

From this equation, it is clear that $(Y_{st}/Y_o)\bar{h}/d_s$ is a function of η_{st}, and is the correct non-dimensional liftoff height. This is the exact parameter used in Ch. 3 for the non-dimensional liftoff height.

For all of the conditions studied except those using a mixture of 86% H_2 / 14% C_2H_6, this definition would have sufficed, because Eq. 3.3 is sufficiently accurate. However, to be consistent with the calculation of U_{cl} and Y_{cl} described in Sec. A.3, a slightly different definition of the non-dimensional liftoff height $\tilde{h}$ was used:

$$\tilde{h} \equiv C_Y \frac{Y_{st}}{Y_{cl}} . \tag{A.20}$$

Using this definition, $\tilde{h}$ is a function of η_{st}, and, as $\rho_{cl} \to \rho_\infty$, $\tilde{h} \to (Y_{st}/Y_o)\bar{h}/d_s$.

A.5 Reynolds Number at the Liftoff Height

The Reynolds number in the cold jet, just below the flame base (Re_h) was determined for each experimental condition by neglecting any possible influence from the flame downstream. In the far field of the jet, where sufficient air has mixed with the jet fluid (fuel) such that $\mu \approx \mu_\infty$ and $\rho \approx \rho_\infty$, the Reynolds number becomes independent of x, and is $Re_\infty = U_s d_s/\nu_\infty$. To get a slightly better estimate of Re_h, the values of U_{cl} and Y_{cl} calculated as described in Sec. A.1 were used.

The local Reynolds number is proportional to $U_{cl}\,\delta/\nu$. Noting that $\delta \propto x$, the precise definition for Re_h is

$$Re_h = \left(\frac{1}{C_u}\right) \frac{U_{cl}\,\bar{h}}{\nu} , \tag{A.21}$$

where $\nu = \mu/\rho$ is evaluated for the mixing cup concentration

$$\breve{Y} = \frac{\dot{m}_f}{\dot{m}} , \tag{A.22}$$

where $\dot{m}_f$ is the mass flux of fuel and $\dot{m}$ is the total mass flux, both evaluated at $x = \bar{h}$. Dividing by the velocity decay constant C_u ensures that as $x \to \infty$, $Re_h \to Re_\infty$.

A.6 Richardson Number at the Liftoff Height

The Richardson number at the flame base Ri_h is defined as the ratio of a buoyancy force B in the vicinity of the flame base, to the momentum flux entering the flame base $J = (\pi/4) d_s^2 U_s^2$. The buoyancy force was calculated from the liftoff height $\bar{h}$ to a distance $\alpha \bar{h}$. This distance was taken as the size of one large structure, making α equal to $1 + C_\delta$, where the jet spreading rate, $C_\delta \equiv \delta/x \approx 0.44$. Then,

$$B = \int_{\bar{h}}^{\alpha \bar{h}} (\rho_\infty - \rho) \mathrm{d}V \ , \tag{A.23}$$

and $Ri_h \sim B/J$. In order to facilitate comparison of this definition of a Richardson number relevant to the liftoff height dynamics with definitions for the flame tip dynamics, a constant factor was added to this definition.

Becker and Liang (1978) used $Ri_L \equiv (g\, L^3)/(U_s^2\, d_s^2)$ as the Richardson number for the flame length, noting that $\rho_\infty - \rho \approx \rho_\infty$ in hydrocarbon flames, and that the volume $\sim L^3$. The actual volume of a cone of height L and spreading rate C_δ is $V_{\mathrm{cone}} = (\pi/12)\, C_\delta^2\, L^3 = 0.051\, L^3$. Therefore, the definition of Ri_h in the current experiments is

$$Ri_h \equiv \frac{12}{\pi\, C_\delta^2\, \alpha^3} \frac{B}{U_s^2\, d_s^2} \ . \tag{A.24}$$

Defining $\overline{\Delta\rho}$ is the spatially averaged value of $\Delta\rho$ in the first flame structure,

$$\overline{\Delta\rho} \equiv \frac{\int_{\bar{h}}^{\alpha \bar{h}} \int_0^{.5\, C_\delta\, x} (\rho_\infty - \rho)\, 2\, \pi\, r\, \mathrm{d}r\, \mathrm{d}x}{\int_{\bar{h}}^{\alpha \bar{h}} \int_0^{.5\, C_\delta\, x} 2\, \pi\, r\, \mathrm{d}r\, \mathrm{d}x} \ , \tag{A.25}$$

Eq. A.23 becomes

$$Ri_h = (\alpha^3 - 1)/\alpha^3\, (g\, \overline{\Delta\rho}\, \bar{h}^3)/(U_s^2\, d_s^2) \ . \tag{A.26}$$

The factor $\alpha^3 - 1$ is included because only the region above h is at low density; the factor of $1/\alpha^3$ is included because without it, this would actually be a Richardson number at $x = \alpha\, \bar{h}$, rather than at $x = \bar{h}$.

The remaining difficulty in this definition was to determine ρ in the flame region. For that, the data of Becker and Yamazaki (1978) for propane flames attached to the nozzle were used in the following manner. By measuring dynamic pressure and temperature, they calculated the mixing cup density $\breve{\rho} \equiv \dot{m}/Q$, where $\dot{m}$ is the mass flux and Q is the volume flux at the downstream measuring station. They found that to a good approximation, $\breve{\rho}/\rho_\infty$ is a function of the local Richardson number and independent of the distance along the flame x/L. In particular, they found that for $\xi_x < 2$, $\breve{\rho}/\rho_\infty \approx 0.20$, where their definition of ξ_x is $(x/d_s)\, g/(U_s^2\, d_s^2)^{1/3}$.

Although their measurements were on attached flames (often using hydrogen stabilization), their data were used to approximate the density in lifted flames. Account was taken of the properties of each fuel in applying their results from propane flames. Because all of the flames studied in the current experiments had $\xi_x < 2$, with the distance $\alpha\,\bar{h}$ used for x, the result that $(\breve{\rho}/\rho_\infty) = 0.2$ was used. This was converted into a mean temperature rise by

$$\frac{\overline{\Delta T}}{\Delta T_f} = \frac{T_\infty}{\Delta T_f}\left(\frac{\rho_\infty}{\breve{\rho}} - 1\right) = 0.6\ , \tag{A.27}$$

where ΔT_f is the adiabatic temperature rise for a stoichiometric mixture of fuel and air. Approximating $\overline{\Delta\rho}$ as $\rho_\infty - \breve{\rho}$ gives

$$\overline{\Delta\rho} = \rho_\infty\left(1 - \frac{T_\infty}{T_\infty + \overline{\Delta T}}\,\frac{\overline{\mathrm{MW}}}{\mathrm{MW}_\infty}\right)\ . \tag{A.28}$$

The average molecular weight in the flame $\overline{\mathrm{MW}}$ was estimated by solving for the mass fractions of product, fuel, and oxidizer from the equations

$$\begin{aligned} Y_p &= \overline{\Delta T}/\Delta T_f \\ Y_{\mathrm{st}}\, Y_p + Y_f &= \dot{m}_{\mathrm{fuel}}/\dot{m}_{\mathrm{air}} \\ Y_p + Y_f + Y_o &= 1\ . \end{aligned} \tag{A.29}$$

A.7 Convection Time Estimates

Estimates of convection times in the flames were made to compare with the simultaneous measurements of h and I at x_I, as well as the measurements of h and L. For the h and I measurements, estimates of the convection times from $\bar{h}$ to x_I and from $x_{I,1}$ to $x_{I,2}$, *etc.* were made. For the h and L experiments, estimates of the convection time from $\bar{h}$ to $\bar{L}$ were made. Centerline velocities were estimated at the locations $\bar{h}$, x_I and $\bar{L}$; these velocities were used in estimating both the convection times and the local large scale times τ_δ.

For the acetylene flames listed in Table 4.7, for which the Richardson numbers at the measurement locations x_I were all low, it was assumed that the centerline velocity is reasonably well approximated by the isothermal result,

$$U_{\rm cl} \;=\; C_u \, U_{\rm s} \, \frac{d_{\rm s}}{x} \;. \tag{A.30}$$

The convection time of fluid traveling at the centerline velocity is then

$$\tau_{\rm c} \;=\; \frac{x_I^2 - \bar{h}^2}{2\, C_u \, U_{\rm s} \, d_{\rm s}} \;. \tag{A.31}$$

Even at low Richardson numbers, the change in density may affect the centerline velocity. However, it was felt that this method would provide a more accurate estimate of $U_{\rm cl}$ for the acetylene flames, than the method described below, which was used for the other fuels, listed in Table 4.8.

For the fuels other that acetylene, two different estimates for the velocity at x_I were made. Because most of the locations were not too far downstream of $\bar{h}$, the first method was simply to use Eq. A.30. Some of the locations x_I were far enough downstream of the flame base that buoyancy would affect the velocities, and so another method for estimating velocities was taken from Becker and Yamazaki (1978). They investigated attached flames, but their results were used as an approximation. Their Eq. 38 can be written

$$U_{\rm cl}^2 \;=\; U_{\rm s}^2 \left(\frac{d_{\rm s}}{x}\right)^2 \frac{\rho_\infty}{\rho_{\rm cl}} \left(2.6 + 0.51\,\xi\right)^3 \;, \tag{A.32}$$

where they have defined ξ as $(g\,x^3/U_s^2\,d_s^2)^{1/3}$. To obtain the centerline density ρ_{cl}, their Fig. 9 was used, approximating the data as

$$\tilde{T}_{cl} \;=\; 0.2 + 0.072\,\frac{Y_{st}\,x}{d_s}\;, \tag{A.33}$$

for $(Y_{st}\,x)/d_s < 6$. Here $\tilde{T}_{cl} \equiv (T_{cl} - T_\infty)/(T_f - T_\infty)$. Then ρ_{cl} was found from

$$\frac{\rho_\infty}{\rho_{cl}} = \frac{\Delta T_f\,\tilde{T}_{cl} + T_\infty}{T_\infty} \tag{A.34}$$

to give an approximation for the centerline velocity. This second method always gave estimates of velocities larger than the isothermal result, Eq. A.30. The average of the two methods was taken as the estimate of $U_{cl}(x_I)$. The reason for not simply using the more complex calculation, which accounts for buoyancy, was that the equations used were obtained form measurements of attached flames, and it was felt that the true value of U_{cl} would lie between the two estimates.

For estimating the velocity at $x = \bar{L}$, a method similar the last one was used. First, the calculated flame length L_{ca} was found from Becker and Yamazaki's Equations (40) and (58)

$$\psi \;=\; \left\{ \begin{array}{ll} 0.202\,, & \text{if } \xi < 1 \\ 0.18 + 0.022\,\xi\,, & \text{if } \xi \geq 1 \end{array} \right\}\;, \tag{A.35}$$

where $\psi = (d_s\,\beta/L_{ca}\,\mathrm{MW}_f)$ with $\beta = (\mathrm{MW}_\infty\,T_f/\mathrm{MW}_f\,T_\infty)^{1/2}$. Then Eq. A.32 was used to find U_{cl} at L_{ca}. However, Eq. A.33 could not be used because it is not applicable above $(Y_{st}\,x)/d_s = 6$. Instead, to estimate ρ_{cl} at L_{ca}, their Fig. 12 was used. Three quantities were obtained from the graph: the maximum normalized centerline concentration $\tilde{T}_{cl,m}$, the location of this maximum location $x_m/L_{ca} \equiv \tilde{x}_m$, and $\tilde{x}$ for which $\tilde{T}_{cl} = 0.8$, $\tilde{x}_{.8}$. Then linear extrapolation was used to get $\tilde{T}_{cl}$ at L_{ca}.

Because the measured flame length $\bar{L}$ was in general less than the calculated flame length L_{ca}, linear interpolation was used to find U_{cl} at $\bar{L}$, using the velocities at $\bar{h}$ and L_{ca} for the interpolation.

The velocity estimates at locations other than $\bar{h}$ have rather large uncertainties, probably $\pm 30\%$, and are intended only as a rough measure against which to compare the correlation times measured in the experiments.

Given these velocity estimates, local passage times were estimated as

$$\tau_\delta(x) = \frac{0.44\,x}{U_{\rm cl}(x)} \ , \tag{A.36}$$

and the convection time from one x_1 location to another x_2 is estimated as

$$\tau_{\rm c} = \frac{x_2 - x_1}{1/2\left(U_{\rm cl}(x_1) + U_{\rm cl}(x_2)\right)} \ . \tag{A.37}$$

A.8 Bound on Temperature Rise of Reactants from Radiation

A very crude estimate for the maximum temperature rise in the reactants approaching the flame base caused by absorption of thermal radiation is presented here. The result is quoted in Sec. 4.5 as a verification that this temperature rise could not be a coupling mechanism between the liftoff height and downstream radiation of the flame.

The following nomenclature is used in this section: q is the total heat release rate of the flame; f_r is the fraction of q that is radiated; ΔH is the heat release per unit mass of fuel, assumed to be 50×10^6 J/kg; α is the absorptivity of the mixture of fuel and air, integrated over the spectrum of the radiation; and $\tau_{\rm c}$ is the convection time from the nozzle exit to $\bar{h}$, integrated along the ray $\eta = 0.15$.

Approximating the radiation as a point source, located an average distance of $1.5\,\bar{h}$ from the reactants, the temperature rise during the convection from the nozzle exit to $\bar{h}$ is

$$\Delta T = \frac{f_r\, q\, \alpha}{4\,\pi\,\rho_\infty\, C_p\,(1.5\,\bar{h})^2}\,\tau_{\rm c} \ , \tag{A.38}$$

where C_p of the reactants is taken to be 1000 J/kg-K. Noting that

$$q = \frac{\pi}{4}\, d_{\rm s}^2\, \rho_\infty\, \Delta H \ , \tag{A.39}$$

and calculating the convection time τ_c by

$$\tau_c = \int_0^{\bar{h}} \frac{dx}{u(x,\eta)} = \frac{0.08}{f_u(\eta)} \frac{\bar{h}^2}{U_s\, d_s} , \tag{A.40}$$

the temperature rise can be found to be

$$\Delta T = \frac{0.08}{16\, f_u(\eta)} f_r \frac{\Delta H}{C_p} \alpha\, d_s \frac{\bar{h}^2}{(1.5\,\bar{h})^2} . \tag{A.41}$$

Taking $f_r = 0.4$, and, as a very conservative estimate $\alpha_a = 0.01$ m^{-1} results in a temperature rise of only 0.002 K. This calculation has a tremendous number of simplifications, but is adequate to show that the temperature rise associated with absorption of radiation is quite small.

APPENDIX B

Tabulated Mean Liftoff Heights

B.1 Measurements Without Air Premixing

Table B.1: $\bar{h}$ Measurements for n.g., Without Air Premixing

d (mm)	U_s (m/s)	$\bar{h}$ (mm)	U_s (m/s)	$\bar{h}$ (mm)	U_s (m/s)	$\bar{h}$ (mm)
4.61	33	89	44	124	56	164
	39	106	50	143		
6.25	42	133	51	159	71	213
	45	141	58	175	74	229
	48	152	64	195		
7.73	39	137	59	187	81	244
	49	166	70	216	90	273

Table B.2: $\bar{h}$ Measurements for C_2H_6, Without Air Premixing

d (mm)	U_s (m/s)	$\bar{h}$ (mm)	U_s (m/s)	$\bar{h}$ (mm)	U_s (m/s)	$\bar{h}$ (mm)
3.12	46	74	58	98	71	124
	53	88	65	110		
3.88	48	89	66	119	87	162
	53	98	73	132	93	180
	59	108	81	147		
4.61	58	115	82	154	111	210
	67	130	91	167		
	74	140	101	187		

Table B.3: $\bar{h}$ Measurements for C_2H_4, Without Air Premixing						
d (mm)	U_s (m/s)	$\bar{h}$ (mm)	U_s (m/s)	$\bar{h}$ (mm)	U_s (m/s)	$\bar{h}$ (mm)
2.16	73	44	92	59	114	77
	83	52	102	67	126	91
3.12	95	66	134	93	165	117
	116	80	149	102	181	134
3.88	111	82	145	103	200	143
	125	92	168	119		

Table B.4: $\bar{h}$ Measurements for C_2H_2, Without Air Premixing						
d (mm)	U_s (m/s)	$\bar{h}$ (mm)	U_s (m/s)	$\bar{h}$ (mm)	U_s (m/s)	$\bar{h}$ (mm)
1.02	173	20	204	28	240	37
	182	23	217	31		
	195	26	234	36		
1.55	226	32	260	38		
	239	34	266	40		

B.2 Measurements with Air Premixing

Table B.5: $\bar{h}$ Measurements for n.g., with Air Premixing							
d (mm)	Y_o	U_s (m/s)	$\bar{h}$ (mm)	U_s (m/s)	$\bar{h}$ (mm)	U_s (m/s)	$\bar{h}$ (mm)
4.61	1	26	74	39	111	50	144
		30	86	41	119	53	156
		33	94	44	127	56	168
		36	102	47	136		
4.92	0.92	25	75	36	108	46	144
		28	85	38	118	49	156
		30	92	41	127	51	169
		33	102	43	138		
6.25	0.69	19	73	27	111	34	152
		21	82	28	121	36	165
		23	91	30	132	38	180
		25	102	32	141		
7.73	0.53	15	68	21	112	27	161
		16	80	22	124	28	174
		18	90	24	136	30	189
		19	99	25	147		

Table B.6: $\bar{h}$ Measurements for C_2H_6, with Air Premixing							
d (mm)	Y_o	U_s (m/s)	$\bar{h}$ (mm)	U_s (m/s)	$\bar{h}$ (mm)	U_s (m/s)	$\bar{h}$ (mm)
3.88	1	47	91	69	128	89	170
		58	110	81	150		
4.92	0.79	37	89	53	128	68	168
		45	110	61	149		
6.25	0.62	30	88	42	132	55	186
		36	112	48	155		
7.73	0.50	24	77	33	128	41	168
		28	104	38	152		

Table B.7: $\bar{h}$ Measurements for C_2H_4, with Air Premixing

d (mm)	Y_o	U_s (m/s)	$\bar{h}$ (mm)	U_s (m/s)	$\bar{h}$ (mm)	U_s (m/s)	$\bar{h}$ (mm)
2.16	1	74	44	92	58	114	78
		83	51	102	67	127	92
3.12	0.69	48	38	65	63	82	91
		53	47	70	71		
		59	55	76	80		
3.88	0.55	38	34	50	63	63	90
		42	44	54	71		
		46	54	59	81		
4.92	0.43	30	27	39	60	49	92
		33	37	42	70		
		36	48	45	81		

APPENDIX C

Correcting Autocorrelation for Finite Sample Time

One of the possible causes of error in the current measurements of h *vs.* time is the non-zero sampling time of the photodiode array. Averaging over a length of time, rather than taking an instantaneous measurement, can cause changes in the measured autocorrelation function. Thus, both the rms level h' and the correlation time $\tau_{1/2}$ can be affected. This appendix describes the method for estimating and correcting the associated errors.

The linear photodiode array used in these experiments has 512 pixels which are scanned successively by the controlling electronics and output onto a serial line which is then input to the A/D board of the computer. After scanning the last pixel, there is a delay of 4 clock cycles (the time needed to read 4 pixels) before the next scan of the array, starting with the first pixel. Each pixel integrates the light incident on it during the entire time between successive scans, making its output equal to the average light intensity during the previous array sample time Δt (ms per scan). Thus each pixel intensity is an average over a slightly different time interval. In the current measurements of h, however, an approximate simplification can be made. Because h moves at most a small fraction of the 512 pixels during any time step, the average of each of the pixels in the near vicinity of h is taken over approximately the same time interval.

Two steps remain in finding an approximate correction to the measurements of h. In Sec. C.1, it is argued that this averaging of light intensity on the linear array has the effect of averaging the liftoff height over the same time interval. In Sec. C.2 a technique for correcting the measured values of h' and $\tau_{1/2}$ is presented.

C.1 Effect of Integration of Light on Measurement of h

To approximate the effect of the integration of light over a time interval on the measurement of liftoff height h, the light intensity profile is linearized about the threshold for determining h, I_t. This linearized profile is given by

$$I(x,t) \;=\; I_t \;+\; \frac{\mathrm{d}I}{\mathrm{d}x}\,(x - h(t)) \;, \tag{C.1}$$

where $\frac{\mathrm{d}I}{\mathrm{d}x}$ is the slope of the I *vs.* x curve, assumed to be constant over the time interval Δt. Taking a time average over Δt,

$$\bar{I}(x) \;=\; I_t \;+\; \frac{\mathrm{d}I}{\mathrm{d}x}\,(x - \bar{h}(t)) \;. \tag{C.2}$$

Therefore, at $x = \bar{h}$, $\bar{I} = I_t$, indicating that averaging the light intensity I over a time interval Δt has the effect of averaging the liftoff height $h(t)$ over the same time interval, subject to the above assumptions.

C.2 Effect of Sampling Time on the Measured Autocorrelation

If the true process to be measured is designated as $x(t)$ and the measurement occurs over an interval Δt, then the measured process $w(t)$ can be written as

$$w(t) \;=\; \frac{1}{\Delta t}\int_{t-\Delta t/2}^{t+\Delta t/2} x(\hat{t})\,\mathrm{d}\hat{t} \;. \tag{C.3}$$

If the integration in Eq. C.3 is approximated by the trapezoidal rule, $w(t)$ can be approximated by $z(t)$ as

$$w(t) \;\approx\; z(t) \;\equiv\; {}^1\!/_2\,[x(t - \Delta t/2) + x(t + \Delta t/2)] \;. \tag{C.4}$$

The autocorrelation of the process $z(t)$ can now be written in terms of the autocorrelation of $x(t)$ as

$$R_{zz}(\tau) \;=\; {}^1\!/_4[2\,R_{xx}(\tau) + R_{xx}(\tau + \Delta t) + R_{xx}(\tau - \Delta t)] \;. \tag{C.5}$$

Because $R_{xx}(\Delta t) = R_{xx}(-\Delta t)$, for $\tau = 0$, Eq. C.5 reduces to

$$R_{zz}(0) = 1/2\, R_{xx}(0) + 1/2\, R_{xx}(\Delta t) \ . \tag{C.6}$$

Given the values of the measured autocorrelation function $R_{zz}(i\,\Delta t)$, for $0 \leq i \leq N$, it is desired to find the corresponding values of the autocorrelation of the true process, $R_{xx}(i\,\Delta t)$. In order to do this, one additional equation is needed at the end of the interval,

$$R_{xx}(N\,\Delta t) = R_{zz}(N\,\Delta t) \ . \tag{C.7}$$

This is equivalent to extrapolating the values of $R_{xx}(N-1)$ and $R_{xx}(N)$ to $R_{xx}(N+1)$. Equation Eq. C.7 completes the set of $N+1$ equations

$$\begin{aligned} 1/2\, R_{xx}(0) + 1/2\, R_{xx}(1) &= R_{zz}(0) \\ 1/4\, R_{xx}(i-1) + 1/2\, R_{xx}(i) + 1/4\, R_{xx}(i+1) &= R_{zz}(i) \quad i = 1, 2, \ldots, N-1 \\ R_{xx}(N) &= R_{zz}(N) \ . \end{aligned} \tag{C.8}$$

From the computed autocorrelation of liftoff height an attempt was made to invert the above set of equations and obtain the autocorrelation in the limit of zero sampling time. However, this set of equations is extremely sensitive to the values of $R_{zz}(i)$, in particular near $i = 0$. Solutions to the equations typically gave oscillatory behavior; values of $R_{xx}(i)$ for even values i were higher than for odd values of i. An alternative method of correcting the autocorrelation measurements was then chosen.

From the autocorrelation of the data set with the best relative resolution (largest $\tau_{1/2}/\Delta t$), Eqs. C.8 were used to compute the autocorrelation which would be obtained by averaging each pair of adjacent data points. From the new autocorrelation, different values of h' and $\tau_{1/2}$ were found. This process was repeated until $\tau_{1/2}/\Delta t$ was less than that of any case studied. From the autocorrelations at the different effective sampling times Δt, a least squares fit was preformed on the equation

$$\frac{\tau_{1/2}(\Delta t)}{\tau_{1/2}(0)} = 1 + \frac{C_1}{(\tau_{1/2}(\Delta t)/\Delta t)^{C_2}} \ . \tag{C.9}$$

From the least squares fit, the values of $C_1 = 0.391$ and $C_2 = 1.042$ were obtained. This equation was then used to solve for $\tau_{1/2}(0)$, the limit of $\tau_{1/2}$ as $\Delta t \rightarrow 0$.

Similarly for the rms levels,

$$\frac{h'(\Delta t)}{h'(0)} = 1 + \frac{C_3}{(\tau_{1/2}(\Delta t)/\Delta t)^{C_4}} \tag{C.10}$$

with $C_3 = -0.113$ and $C_4 = 1.004$ was used to estimate the values of h' in the limit $\Delta t \rightarrow 0$.

These equations resulted in at most a 5% increase in the value of h' and a 15% decrease in the value of $\tau_{1/2}$. The accuracy of this correction technique was checked in two ways. First, the scheme described to determine the values of $C_1, \ldots, C_4$ was applied to another autocorrelation function and the corrected values of $\tau_{1/2}$ and h' compared at the various resolutions. For $1.7 < \tau_{1/2}(\Delta t)/\Delta t < 6.0$, the values of h' agreed with one another to within 0.5% and the values of $\tau_{1/2}$ to within 1%.

For the second test, data were taken at two different sampling times, Δt, but under the same experimental conditions. The correction equations (Eqs. C.8 and C.9) were applied to h' and $\tau_{1/2}$ and compared. For $\tau_{1/2}(\Delta t)/\Delta t = 2.8$, the (corrected) value of $\tau_{1/2}/\tau_\delta$ was 1% higher, and the value of $h'/\bar{h}$ was 0.5% higher than at $\tau_{1/2}(\Delta t)/\Delta t = 5.9$.

Having confidence that the correction technique was accurate, it was applied to all the data to adjust the values of h' and $\tau_{1/2}$.

APPENDIX D

Accuracy Estimates and Experimental Considerations

In this appendix estimates are given for the accuracy of various measured and calculated quantities. This includes the measurement of flow velocity and the calculated autocorrelation time $\tau_{1/2}$, as well as the large scale time at the liftoff height τ_δ, which is used to normalize $\tau_{1/2}$.

Along with identifying the size of errors in the measurements, some analysis of the sensitivity of the measurements to the exact experimental conditions and measurement technique is presented. This includes the arrangement of screens around the flame for protecting it from room disturbances and the choice of what fraction of the flame width to image when finding the liftoff height.

D.1 Measurement of Flow Velocities

Velocities of gases exiting the nozzles were calculated from measurements with laminar flow elements (LFE's), across which the pressure drop was measured with a Barocel pressure transducer as described in Sec. 2.1.1. The exit velocity was then calculated by assuming that the gas reached atmospheric pressure and temperature. The sources of error in the measurements are 1) error in calibration of the LFE, 2) error in measurement of pressure drop Δp, 3) error in knowledge of the gas viscosity, used to convert Δp to flow rate, and 4) the gas not reaching a uniform temperature of T_∞ at the nozzle exit (applicable at the higher Mach numbers).

The LFE's have reported accuracies of $\pm 0.5\%$. By fitting the points to a parabola of Δp *vs.* flow rate, this accuracy should be achievable at any flow rate in the usable range. In the current experiments, the repeatability was approximately $\pm 0.5\%$, and the accuracy approximately $\pm 2\%$, as checked by comparing the two flow meters. The pressure transducer is accurate to $\pm 0.1\%$ of the reading, and so it should not contribute substantially to the measurement error. Viscosities were taken from Reid *et al.* (1978). In comparing them to the CRC Handbook (Weast 1974), the values were found to be within 1% for all gases except acetylene, which differed by 2%. Because the flow-rate is approximately proportional to $\Delta p/\mu$, the corresponding uncertainty in estimating U_o, is $\sim$ 2% for C_2H_2 and $\sim$ 1% for the other fuels.

For the higher Mach number flows, the largest possible error in calculating velocities stems from the assumption that the exit temperature equals T_∞. Heat transfer calculations indicate that this should be a reasonable assumption. However, to estimate the largest possible error, calculations were also done assuming adiabatic expansion to atmospheric pressure and compared with the isothermal calculations. The adiabatic velocity estimates are always lower, being 0.5, 2.0, 2.5, and 6.5% lower than the isothermal velocities for the highest velocity cases of the four fuels: natural gas, C_2H_6, C_2H_4, and C_2H_2, respectively. The calculation of d_s is always larger for the adiabatic calculation, by a percent approximately half that for the velocity calculation. Therefore, the calculation of $U_s\, d_s$, on which both the Reynolds number (Re_∞) and large-scale time (τ_δ) calculations rely, would be only 0.25, 1.0, 1.3, and 3.3 % lower in the extreme case of adiabatic flow to the nozzle exit.

D.2 Resolution Limits Caused by Pixel Spacing

The photodiode array used in the measurement of h has 512 pixels, spaced at 50 μm intervals. Each pixel has a width of 2.5 mm. For each flow condition, the placement of the array was chosen such that the width of the flame image just filled the width of the array. This determined the distance at the flame corresponding to the spacing between two pixel centers, Δh. Specifically, $\Delta h/\bar{h} = 0.008$.

This resolution can affect the accuracy of both the mean liftoff height $\bar{h}$ and the other quantities derived from the measurement of h *vs.* t. The time averaging will allow $\bar{h}$ to be measured to accuracies better than Δh, and so Δh is an upper bound on the error of the measurement of $\bar{h}$.

An approximate analysis of the effect of the pixel spacing on measurement of the rms fluctuations h' can be made by assuming that the error associated with binning the true liftoff height h_t to an integer number of pixels for the measured liftoff height h_m, $e \equiv h_m - h_t$, is uncorrelated with h_t. The rms of the error e is then $e' = \Delta h/\sqrt{12}$. Using the experimental result that $h'/\bar{h} \approx 0.07$ results in the estimate for the error in determining the rms of h as

$$\frac{e'}{h'} = \frac{e'}{\Delta h}\frac{\Delta h}{\bar{h}}\frac{\bar{h}}{h'} = 0.03 \ . \tag{D.1}$$

D.3 Errors Caused by Integrating Measurement over Time

In Appendix C the technique for reducing the error of the measurement of $\tau_{1/2}$ caused by the non-zero sample time of the linear array is discussed. Because several approximations were made in deriving the correction technique, errors will remain.

To estimate the remaining errors, two experiments were conducted with identical flow conditions, but with different temporal resolutions, changed by adjusting the clocking rate of the array. As acetylene was found to have the shortest (dimensionally) correlation times of all the pure fuels, conditions were selected to match

the resolution of the acetylene experiments. For this, ethylene was used, with measurements first made at $\Delta t = 4.4$ ms, and then at a time step of 10.0 ms. This longer time was selected to match the resolution of the C_2H_2 group A experiments where $\tau_{1/2}/\Delta t \approx 2.3$.

The autocorrelation functions were computed and corrected for sampling time as described in Appendix C. There is very little difference between the estimates of $\tau_{1/2}/\tau_\delta$ for the two cases with the values being 14.8 and 15.0 for the fast and slow sampling, respectively.

The measured rms is also affected by the sample time, and was corrected by the same technique as the autocorrelation. Values of $h'/\bar{h}$ are 0.0597 and 0.0600 for the fast and slow sampling, respectively. This is verification that the reported values of $h'/\bar{h}$ are reasonably accurate, even for the acetylene flames.

An additional test of the temporal resolution effects was made by modifying the data acquisition system, allowing just 256 of the 512 pixels of the linear array to be sampled. This enabled a sampling time of 2.2 ms, compared with the standard sampling time of 4.4 ms. The results from a mixture of 86% H_2 / 14% C_2H_6 again indicated close agreement in the measured autocorrelation. Namely, as $\tau_{1/2}/\Delta t$ was increased from 2.5 to 5, the measured $\tau_{1/2}/\tau_\delta$ decreased only 6%.

D.4 Accuracy of Estimate of $\tau_{1/2}$

$\tau_{1/2}$ is defined as the time at which the autocorrelation function of liftoff height reaches a value of 0.5. To estimate the accuracy to which this time scale is known, the following procedure was used. The data record of h *vs.* t was broken up into eight pieces. The autocorrelation was then calculated for each piece, and the resulting value of $\tau_{1/2}$ determined. From these eight measurements of $\tau_{1/2}$, the standard deviation was calculated. To estimate the accuracy to which the value of $\tau_{1/2}$ is known when using the entire data record, it was assumed that the eight individual pieces were statistically uncorrelated. Under this assumption the standard deviation

of the measure of $\tau_{1/2}$ for the entire data record would equal the standard deviation for the individual measurements divided by $\sqrt{8}$.

As an example, using the seventh condition listed in Table 4.2 (ethane, $d = 3.88$ mm, $\tilde{h} \approx 2.2$) the standard deviation of the eight individual measurements was found to be 4.5% of the mean value. Dividing this by $\sqrt{8}$, gives an accuracy of 1.5% on the estimate of $\tau_{1/2}$. With the exception of the eighth case in Table 4.2, during which the gas supply was depleted, the accuracies of all the measurements of $\tau_{1/2}$ are estimated to be better than $\pm 3\%$.

D.5 Calculation of Local Large-Scale Time

The large-scale time at the liftoff height $\tau_\delta(\bar{h})$ is defined as $\delta/U_{\rm cl}$. The velocity was estimated as described in Sec. A.3, with δ defined as

$$\delta \;=\; C_\delta \, x \;, \tag{D.2}$$

where $C_\delta = 0.44$. For most of the cases studied, $\rho_{\rm cl}(\bar{h}) \approx \rho_\infty$, and the velocity estimate reduces to

$$U_{\rm cl} \;=\; C_u \, U_{\rm s} \, \frac{x}{d_{\rm s}} \;, \tag{D.3}$$

with $C_u = 6.17$.

One source of error in this calculation stems from the fact that no jet virtual origin x_o was used in the above equations, *e.g.*, replacing x with $(x - x_o)$. If both $U_{\rm cl}$ and δ were to have the same virtual origin, then the fractional error in estimating τ_δ would be $\sim 2\,x_o/\bar{h}$. Taking $x_o = 2\,d$ and $\bar{h} = 20\,d$ (the lowest liftoff heights studied), results in a fractional error of $\sim 20\%$. For the highest liftoff heights the error would be reduced to $\sim 10\%$. This is possibly the largest source of error in the presented data.

D.6 Fraction of Jet Width Imaged

The choice of what fraction of the flame width to image onto the photodiode array could potentially affect the results of both the mean liftoff height and the temporal behavior.

Chapter 3 describes measurements of h *vs.* t that were made for relatively short times, where only the mean values were reported. In those measurements, for the flames near blowout (specifically for flames with $Y_{st}\bar{h}/d_s > 2.2$), the outer parts of the flames were chopped off of the image. At the highest liftoff height ($Y_{st}\bar{h}/d_s \approx 2.6$), approximately $0.84\,\delta$ was imaged. To see what effect that would have on the mean measurements, two experiments were conducted which were identical, except for the distance of the array from the flame. This changed the fraction of the flame width's image on the array, as well as the resolution of the measurement. For the first case, $0.65\,\delta$ was imaged, and for the second case, the entire jet width δ was imaged.

The fuel was natural gas, $d = 6.25$ mm, $U_s = 61$ m/s. The measured value of $\bar{h}$ for the first case was 182.6 mm, and for the second case 182.4 mm, essentially identical results. This indicates that the measure of $\bar{h}$ is not very sensitive to the fraction of the flame width imaged, at least down to $w/\delta = 0.65$, where w is the width imaged.

The same measurements are also able to give an indication of how sensitive the temporal measurements are to the fraction of the flame width imaged. The autocorrelations from the two cases are plotted in Fig. D.1, along with a third curve to be discussed in Sec. D.7. There is no significant change in the autocorrelation when the fraction of the flame imaged is reduced to 0.65. Whether a further reduction, say to just a thin strip along the centerline, would change the time scales measured has not been investigated.

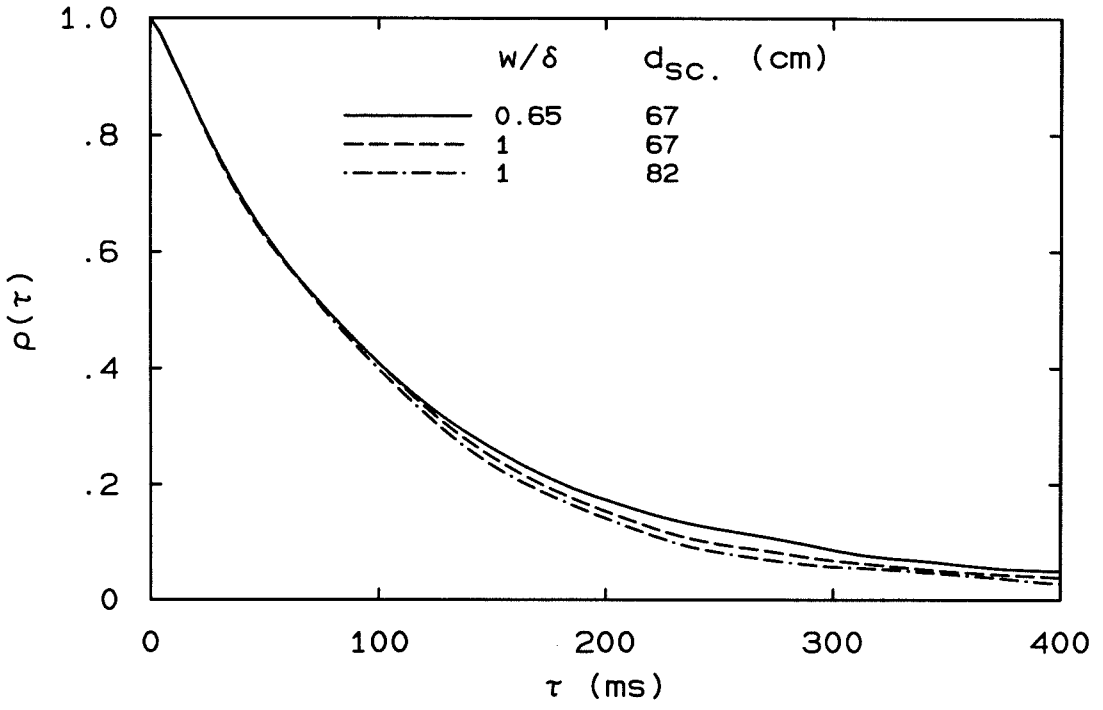

FIG. D.1 Autocorrelation of liftoff height. Natural gas, $d = 6.25$ mm, $U_s = 61$ m/s. Solid line: fraction of width imaged $w/\delta = 0.65$, dashed line: $w/\delta = 1$, dot-dash: same as dashed, except a larger screen diameter was used.

D.7 Effect of Diameter of Screen Surrounding Flame

To see how the time scales of the h fluctuations are affected by the surrounding cylindrical screen, measurements were made in which a screen with a larger diameter was used, to compare with results of the standard, smaller screen.

These results from the larger 82 cm screen are compared to those of the 68 cm screen in Fig. D.1. As there is no measurable difference in correlation times, the reported results are relatively insensitive to screen diameter used, as long as the screen is large enough. The possibility that the large correlation times measured scales in some way with the screen diameter can therefore be ruled out.

APPENDIX E

Photographs of Lifted Flames

Photographs of natural gas, ethylene and acetylene flames are shown in this appendix. All photographs were taken with a Nikon 35 mm camera using T-max 3200 speed film pushed to 6400 during development. The range of liftoff heights in the photographs of each fuel corresponds roughly to the range $1.8 \leq \tilde{h} \leq 2.6$.

Figure E.1 shows natural gas flames using a nozzle diameter of 4.61 mm, taken with an exposure time of 1/1000 s, at f/1.4. Flames at four different flow velocities are shown, with two photographs at each velocity, *e.g.*, (a) and (a′), except at the highest velocity for which only one photograph was taken. From these photographs it is clear that the flame base is not a flat front. Rather it can be quite irregular. This is particularly evident in parts (c) and (d) of Fig. E.1, which are flames rather close to blowout. In some of the photographs, tongues of flame protruding down toward the nozzle can be seen. As an aid to judging the degree to which these photographs represent instantaneous images, the ratio of the exposure time to τ_δ ranges from $\sim$ 0.13 to 0.10 in going from (a) to (d).

Photographs of C_2H_4 flames are shown in Fig. E.2, taken with an exposure time of 1/4000 s, at f/2.0. The bright regions in the tops of the photos of (a) and (a′) are radiation from soot, and the visible light is yellow, wheres the flame base appears blue. The soot level decreases as the blowout velocity is approached. The flame base is again irregular, although it has a slightly different appearance from the natural gas flames. The undulations are smaller, giving the base a rough shape, but with less large-scale deformation. For these images, the ratio of the exposure time to τ_δ ranges from $\sim$ 0.19 to 0.12 in going from (a) to (d), indicating only slightly poorer resolution than the natural gas photos of Fig. E.1.

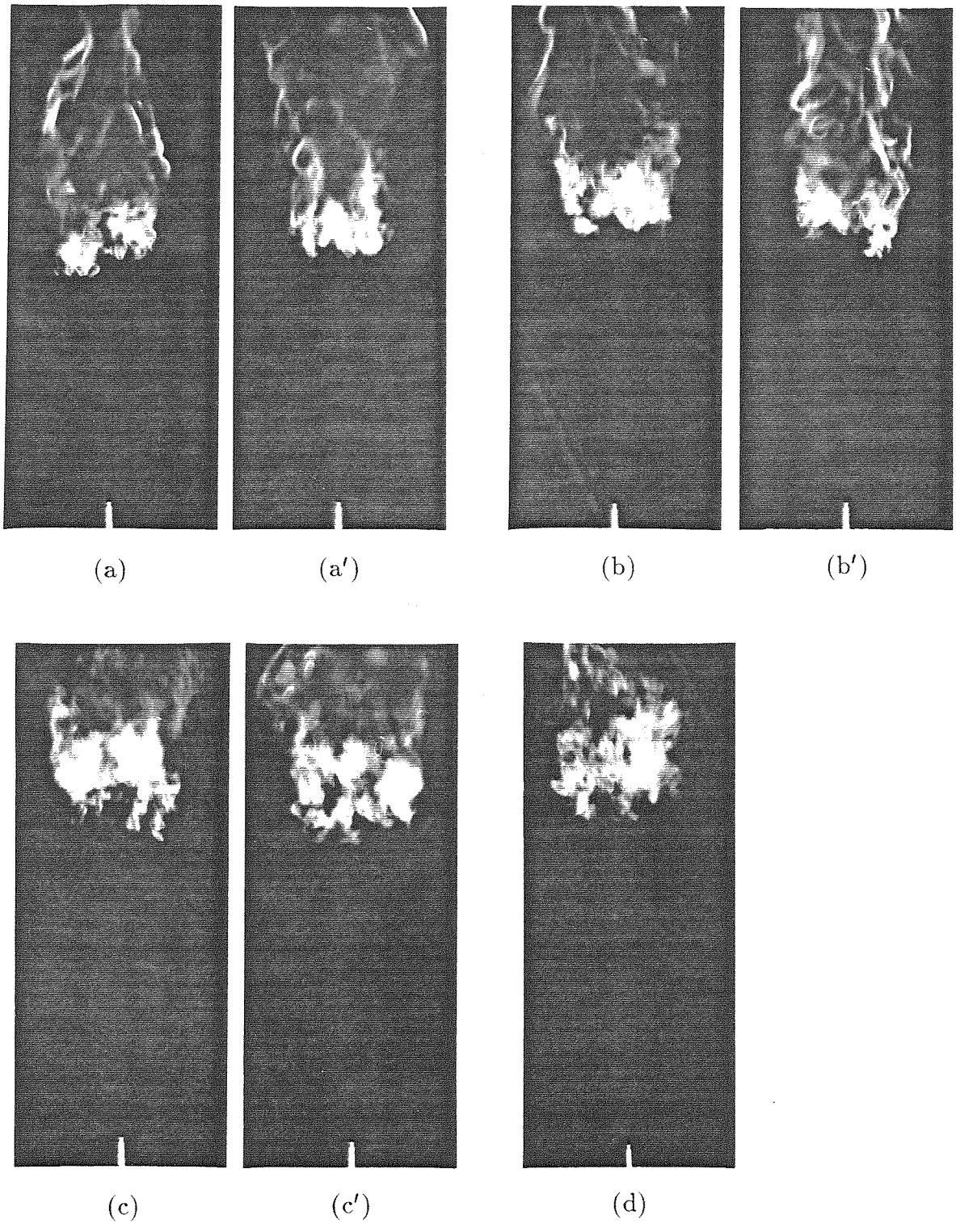

FIG. E.1 Natural gas flames; $d = 4.61$ mm; (a) & (a′) $U_o = 45$ m/s, (b) & (b′) 52 m/s, (c) & (c′) 57 m/s, and (d) 59 m/s.

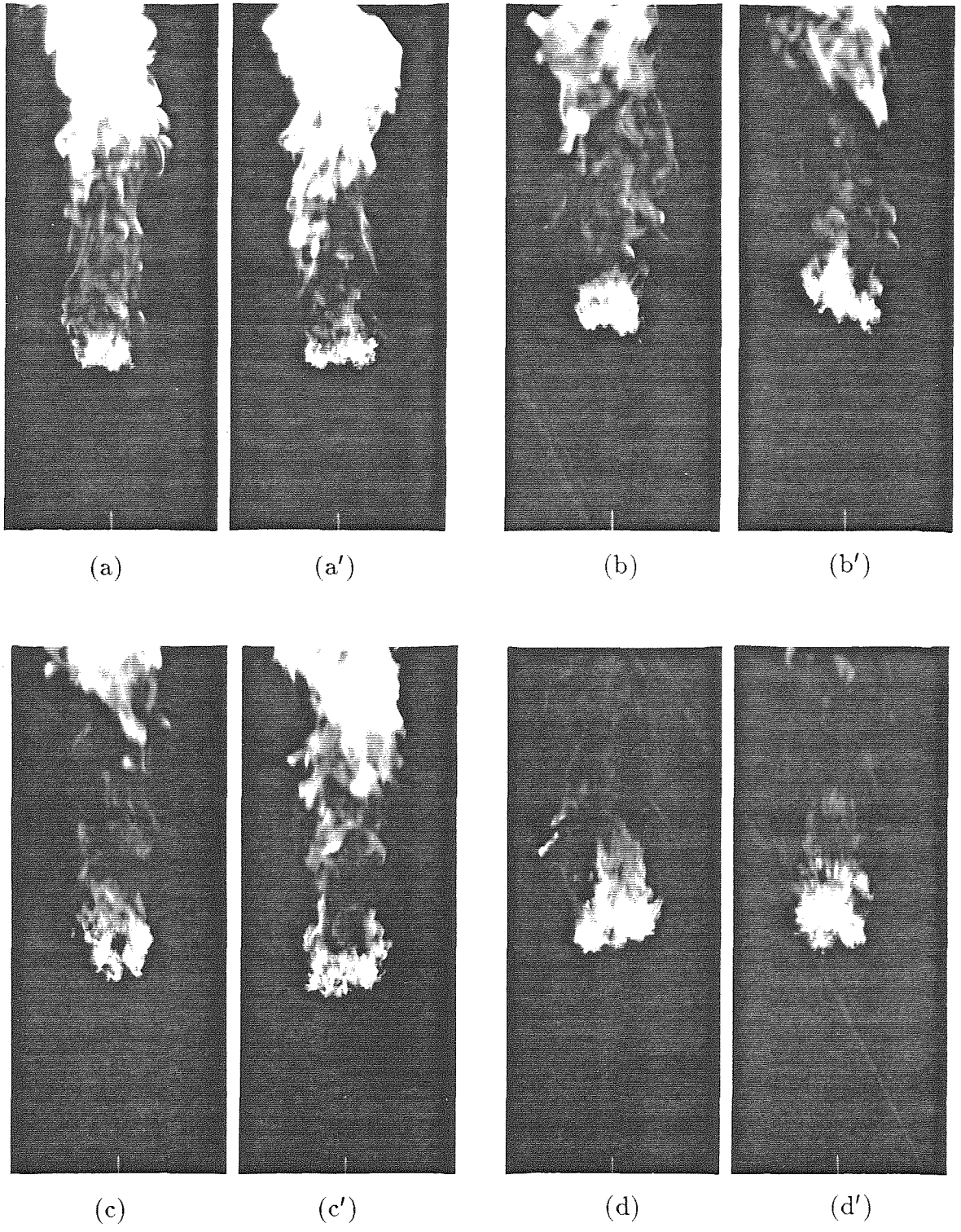

FIG. E.2 C_2H_4 flames; $d = 2.16$ mm; (a) & (a′) $U_o = 95$ m/s, (b) & (b′) 110 m/s, (c) & (c′) 112 m/s, and (d) & (d′) 123 m/s.

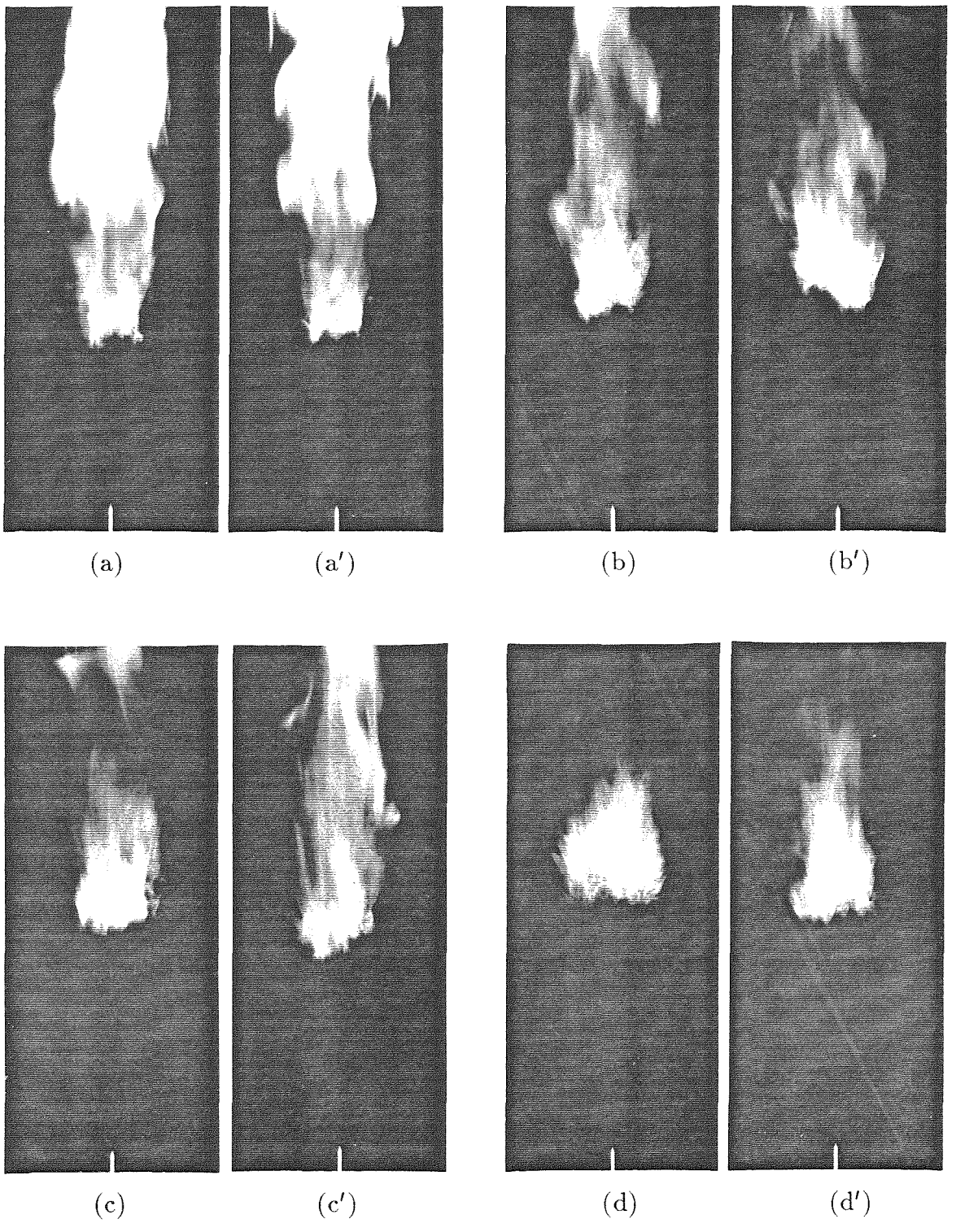

FIG. E.3 C_2H_2 flames; $d = 1.02$ mm; (a) & (a′) $U_o = 200$ m/s, (b) & (b′) 215 m/s, (c) & (c′) 225 m/s, and (d) & (d′) 235 m/s.

Finally, photographs of acetylene flames are shown in Fig. E.3, taken with an exposure time of 1/4000 s, at f/8.0. The bright regions downstream of the initial flame base are again caused by soot. These soot regions are reduced as the blowout condition is approached, and in (d) and (d′) the soot is not visible at all. The flame base is very bright (blue) and the region just downstream is dim (not even visible in the photo of (d)). The exposure time divided by τ_δ ranges from ~ 0.91 to 0.62 for these images, indicating that there is some blurring.

References

BECKER, H. A. and LIANG, D. [1978] "Visible Lengths of Vertical Free Turbulent Diffusion Flames," *Comb. and Flame* **32**, 115–137.

BECKER, H. A. and YAMAZAKI, S. [1978] "Entrainment, Momentum Flux and Temperature in Vertical Free Turbulent Diffusion Flames," *Comb. and Flame* **33**, 123–149.

BIRCH, A. D. and HARGRAVE, G. K. [1989] "Lift-off Heights in Underexpanded Natural Gas Jet Flames," *Twenty-Second Symposium (International) on Combustion* (The Combustion Institute), 825–831.

BROADWELL, J. E., DAHM, W. J. A. and MUNGAL, G. [1985] "Blowout of Turbulent Diffusion Flames," *Twentieth Symposium (International) on Combustion* (The Combustion Institute), 303–310.

CHEN, C. J. and RODI, W. [1980] "Vertical Turbulent Buoyant Jets," (Pergamon Press, Oxford).

CHEN, T. H., GOSS, L. P., TALLEY, D. and MIKOLAITIS, D. [1989] "Stabilization Zone Structure in Jet Diffusion Flames from Liftoff to Blowout," AIAA 27th Aerospace Sciences Meeting (Reno, Nevada) AIAA Paper 89–0153.

CHOMIAK, J. [1990] "Combustion: A Study in Theory, Fact and Application," (Gordon and Breach Science Publishers, New York, p. 370.)

CHUNG, S. H. and LEE, B. J. [1991] "On the Characteristics of Laminar Lifted Flames in a Non-Premixed Jet," *Comb. and Flame* **86**, 62–72.

DAHM, W. J. A. and DIMOTAKIS, P. E. [1987] "Measurements of Entrainment and Mixing in Turbulent Jets," *AIAA J.* **25**, 1216–1223.

DAHM, W. J. A. and DIMOTAKIS, P. E. [1990] "Large Schmidt Number Mixing of a Conserved Scalar in the Self-Similar Far Field of Turbulent Jets," *J. Fluid Mech.* **217**, 299–330.

DIMOTAKIS, P. E. [1993] "Some Issues on Turbulent Mixing and Turbulence," Turbulence Symposium for W. C. Reynolds' 60^{th} birthday (22–23 March 1993, Monterey, CA), GALCIT Report FM 93–1.

DIMOTAKIS, P. E., MIAKE-LYE, R. C. and PAPANTONIOU, D. A. [1983] "Structure and Dynamics of Round Turbulent Jets," *Physics of Fluids* **26**(11), 3185–3192.

DIXON-LEWIS, G., DAVID, T., and GASKELL, P. H. [1986] "Structure and Properties of Methane-Air and Hydrogen-Air Counterflow Diffusion Flames," *Archivum Combustionis* **6**(1), 3–21.

DOWLING, D. R. "Mixing in Gas Phase Turbulent Jets," [1988] Ph.D. Thesis, Caltech.

EGOLFOPOLOUS, F. N. and LAW, C. K. [1991] "An Experimental and Computational Study of the Burning Rates of Ultra-Lean to Moderately-Rich $H_2/O_2/N_2$ Laminar Flames with Pressure Variations," *Twenty-Third Symposium (International) on Combustion* (The Combustion Institute), 333–340.

EGOLFOPOLOUS, F. N., ZHU, D. L. and LAW, C. K. [1991] "Experimental and Numerical Determination of Laminar Flame Speeds: Mixtures of C_2-Hydrocarbons with Oxygen and Nitrogen," *Twenty-Third Symposium (International) on Combustion* (The Combustion Institute), 471–478.

EICKHOFF, H., LENZE, B. and LEUCKEL, W. [1985] "Experimental Investigation on the Stabilization Mechanism of Jet Diffusion Flames," *Twentieth Symposium (International) on Combustion* (The Combustion Institute), 311–318.

GAYDON, A. G. and WOLFHARD, H. G. [1970] "Flames, Their Structure, Radiation and Temperature," (3rd edition, revised, The Chaucer Press, Ltd., Suffolk, p. 30).

GILBRECH, R. J. [1991] "An Experimental Investigation of Chemically-Reacting Gas-Phase Turbulent Jets," Ph.D. Thesis, Caltech.

GLASSMAN, I. [1977] "Combustion," (Academic Press, Inc., Orlando, p. 84).

GOLLAHALLI, S. R., SAVAS, Ö., HUANG, R. F. and AZARA, J. L. R. [1987] "Structure of Attached and Lifted Gas Jet Flames in Hysteresis Region," *Twenty-first Symposium (International) on Combustion* (The Combustion Institute), 1463–1471.

HAMMER, J. A. [1990] "A Comparison of Several Theories which Use Jet Scaling to Predict Liftoff Heights of Turbulent-Jet Flames," GALCIT Report FM 90–3.

KALGHATGI, G. T. [1984] "Lift-off Heights and Visible Lengths of Vertical Turbulent Jet Diffusion Flames in Still Air," *Combust. Sci. and Technol.* **41**, 17–29.

LIEPMANN, H. W. and ROSHKO, A. [1957] "Elements of Gasdynamics," (Wiley, New York).

LOCKWOOD, F. C. and MONEIB, H. A. [1982] "Fluctuating Temperature Measurements in Turbulent Jet Diffusion Flame," *Comb. and Flame* **47**, 291–314.

MASTORAKOS, E., TAYLOR, A. M. K. P. and WHITELAW, J. H. [1992] "Extinction and Temperature Characteristics of Turbulent Counterflow Diffusion Flames with Partial Premixing," *Comb. and Flame* **91**, 40–54.

MIAKE-LYE, R. C. and HAMMER, J. A. [1989] "Lifted Turbulent Jet Flames: A Stability Criterion Based on the Jet Large-Scale Structure," *Twenty-Second Symposium (International) on Combustion* (The Combustion Institute), 817–824.

MUNGAL, M. G., KARASSO, P. S. and LOZANO, A. [1991] "The Visible Structure of Turbulent Jet Diffusion Flames: Large Scale Organization and Flame Tip Oscillation," *Combust. Sci. and Technol.* **76**, 165–185.

NAMAZIAN, M., SCHMITT, R. and LONG, M. G. [1988] "Two-Wavelength Single Laser CH and CH_4 Imaging in a Lifted Turbulent Flame," *Applied Optics* **27**(17), 3597–3600.

NIKURADSE, J. [1932] "Gesetzmässigkeiten der Turbulenten Strömung in Glatten Rohren," *VDI Forschungsheft* **356**(1), translated as "Regularity of Turbulent Flow in Smooth Pipes," [1949] Project SQUID Purdue Univ., Tech. Memo Pur-11.

PAPAMOSCHOU, D. and ROSHKO, A. [1988] "The Compressible Turbulent Shear Layer: an Experimental Study," *J. Fluid Mech.* **197**, 453–477.

PETERS, N. and WILLIAMS, F. A. [1983] "Liftoff Characteristics of Turbulent Diffusion Flames," *AIAA J.* **21**(3), 423–429.

PITTS, W. M. [1989] "Assessment of Theories for the Behavior and Blow Out of Turbulent Jet Diffusion Flames," *Twenty-Second Symposium (International) on Combustion* (The Combustion Institute), 808–816.

PRESS, W. H., FLANNERY, B. P., TEUKOLSKY, S. A. and VETTERING, W. T. [1988] "Numerical Recipes in C, The Art of Scientific Computing," (Cambridge University Press, New York, pp. 432–434).

PURI, I. K., SESHADRI, K. SMOOKE, M. D. and KEYES, D. E. [1987] "A Comparison Between Numerical Calculations and Experimental Measurements of the Structure of a Counterflow Methane-Air Diffusion Flame," *Combust. Sci. and Tech.* **56**, 1–22.

REID, R. C., PRAUSNITZ, J. M. and SHERWOOD, T. T. [1977] "The Properties of Gases and Liquids," (McGraw-Hill, pp. 406–407).

SAVAS, Ö. and GOLLAHALLI, S. R. [1986a] "Structure in Near-Nozzle Region of Gas Jet Flames," *AIAA J.* **24**(7), 1137–1140.

SAVAS, Ö. and GOLLAHALLI, S. R. [1986b] "Stability of Lifted Laminar Round Gas-Jet Flame," *J. Fluid Mech.* **165**, 297–318.

SO, R. M. C., ZHU, J. R., ÖTÜGEN, M.V., and HWANG, B.C. [1990] "Some Measurements in a Binary Gas Jet," *Experiments in Fluids* **9**, 273–284.

TSUJI, H. and YAMAOKA, F. [1969] "Structure of Counterflow Diffusion Flames in the Forward Stagnation Region of a Porous Cylinder," *Twelfth Symposium (International) on Combustion* (The Combustion Institute) 997–1005.

VANQUICKENBORNE, L. and VAN TIGGELEN, A. [1966] "The Stabilization Mechanism of Lifted Diffusion Flames," *Comb. and Flame* **10**, 59–69.

WEAST, R. C., ed., [1974] "CRC Handbook of Chemistry and Physics," (65^{th} edition, CRC Press, Inc., Boca Raton, FL, pp. F42–F44).

WYGNANSKI I. and FIEDLER, H. E. [1969] "Some Measurements in the Self-Preserving Jet," *J. Fluid Mech.* **38**, 577–612.